SOME STUDIES ON HEMODYNAMIC MODELING IN HUMAN CEREBRAL VASCULATURE

Thesis submitted by

PRANATI RAKSHIT

DOCTOR OF PHILOSOPHY (ENGINEERING)

Department of Computer Science and Engineering,
Faculty Council of Engineering & Technology
Jadavpur University
Kolkata-700032, India

2018

JADAVPUR UNIVERSITY
KOLKATA- 700 032, INDIA

INDEX NO. 232/13/E

1. TITLE OF THE THESIS:

SOME STUDIES ON HEMODYNAMIC MODELING IN HUMAN CEREBRAL VASCULATURE

2. NAME, DESIGNATION & INSTITUTION OF THE SUPERVISORS:

   i. **PROF. MITANASIPURI**
   PROFESSOR,
   DEPARTMENT OF COMPUTER SCIENCE AND ENGINEERING, JADAVPUR UNIVERSITY
   KOLKATA-700032, INDIA

   ii. **PROF. SUBHADIP BASU**
   PROFESSOR,
   DEPARTMENT OF COMPUTER SCIENCE AND ENGINEERING, JADAVPUR UNIVERSITY
   KOLKATA-700032, INDIA

3. LIST OF PUBLICATIONS:

   a. **JOURNAL**:

1. Indranil Guha, Nirmal Das, **Pranati Rakshit**, Mita Nasipuri, Punam Kumar Saha, Subhadip Basu, “A semiautomatic approach for segmentation of carotid vasculature from patients' CTA images”, *Innovations in Systems and Software Engineering*, vol. 13, no. 4, pp: 243-250, Dec, 2017. Springer, Scopus indexed. ISSN:1614-5046(Print)1614-5054(Online).

2. **Pranati Rakshit**, Mita Nasipuri, Nirmal Das, Subhadip Basu, “Classification of anomalous region in human cerebrovascular structure using random forest”, *International Journal of Latest*

Trends in Engineering and Technology, vol. 09, no. 03, pp: 015-021, JAN, 2018. ISSN: e-ISSN:2278-621X

3. **Pranati Rakshit**, Nirmal Das , Mita Nasipuri, Subhadip Basu, "Classification of normal and anomalous regions in 3D human cerebrovascular phantom", International Journal of Scientific & Engineering Research, Volume 8, Issue 3, pp:1863-1867, March 2017. ISSN 2229-5518.

b. CONFERENCE:

1. **Pranati Rakshit**, Nirmal Das, Mita Nasipuri, Subhadip Basu, "Hemodynamic Analysis on Human Cerebrovascular Phantom with and without Aneurysm", in proc. of 2nd International Conference on Computing and Communication System (I3CS), NEHU, Shillong, 2016. *Lecture Notes in Networks and Systems 24*, pp: 383-392, *Springer*.

2. Nirmal Das, **Pranati Rakshit**, Mita Nasipuri, Punam Saha, Subhadip Basu, "3-D Digital flows in cerebrovascular phantoms", Ninth International Conference on Advances in Pattern Recognition (ICAPR-2017).December 27-30, 2017, Organized by Indian Statistical institute, Kolkata, Indian Statistical institute, Bangalore.

c. BOOK CHAPTER:

1. **Pranati Rakshit**, Nirmal Das, Mita Nasipuri, Subhadip Basu, "A Qualitative Hemodynamic Analysis on Human Cerebrovascular Phantom", pp: 219-229, *Progress in Advanced Computing and Intelligent Engineering*, Springer**,** Singapore, 2018. ISBN: 9789811068744**.**

2. Indranil Guha, Nirmal Das, **Pranati Rakshit**, Mita Nasipuri, Punam Saha, Subhadip Basu, "Design of cerebrovascular phantoms using fuzzy distance transform based geodesic paths", pp: 359-367, *Progress in Intelligent Computing Techniques:Theory, Practice, and Applications*, Springer, Singapore, 2018. Adv Intelligent System Computing Book series. 2018.

4. LIST OF PATENTS: NONE

5. LIST OF PRESENTATIONS IN INTERNATIONAL / NATIONAL CONFERENCE:

1. **Pranati Rakshit**, Nirmal Das, Mita Nasipuri, Subhadip Basu, “A Qualitative Hemodynamic Analysis on Human Cerebrovascular Phantom”, Springer, 1st conference on Adavanced computing and Intelligent Engineering, CV Raman college of Engg, Bhubaneswar, 2016.

2. **Pranati Rakshit**, Nirmal Das, Mita Nasipuri, Subhadip Basu, “Hemodynamic Analysis on Human Cerebrovascular Phantom with and without Aneurysm”, Springer, Second International conference on computing and communication system(i3cs), 2016, NEHU, Shillong.

CERTIFICATE FROM THE SUPERVISORS

This is to certify that the thesis entitled ***"SOME STUDIES ON HEMODYNAMIC MODELING IN HUMAN CEREBRAL VASCULATURE"*** *submitted by* ***PRANATI RAKSHIT****, who got her name registered on* ***29TH OCTOBER, 2013*** *for the award of Ph.D. (Engg.) degree of Jadavpur University is absolutely based upon her own work under the supervision of* ***PROF. MITA NASIPURI*** *and* ***PROF. SUBHADIP BASU*** *and that neither her thesis nor any part of the thesis has been submitted for any degree/diploma or any other academic award anywhere before.*

1. ______________________________

(Prof. Mita Nasipuri)

Signature of the Supervisor
and date with Office Seal

2. ______________________________

(Prof. Subhadip Basu)

Signature of the Supervisor
and date with Office Seal

Dedicated to my parents

Ajit Kumar Rakshit & Kalpana Rakshit,

My grandmother

Late Durga Rani Kumar

&

My beloved daughter

Ekaparna Ghosh

ACKNOWLEDGEMENTS

First and foremost, I wish to thank God for giving me strength and courage to complete this thesis and research.

I am deeply indebted to many people who have contributed in making the completion of this dissertation work possible. Above all, I would like to express my sincere thanks and heartfelt gratitude to my Ph.D. supervisors **Prof. Mita Nasipuri**, Professor, Department of Computer Science and Engineering, Jadavpur University, Kolkata, India and **Prof. Subhadip Basu**, Professor, Department of Computer Science and Engineering, Jadavpur University, Kolkata, India, for their excellent guidance and support during the period of my Ph.D. study. They have been always a source of inspiration to me for their patience, motivation, enthusiasm. I appreciate all their contributions of time, ideas that have made my Ph.D. experience productive and stimulating. I am indebted to both of them and wish to have their academic support and kind help in my future academic life.

Besides my advisor, I would like to thank the rest of my thesis committee: Prof. Utpal Garain, ISI, Kolkata, Prof. Mahantapas Kundu, Professor, Department of Computer Science and Engineering, Jadavpur University for their insightful comments, encouragement and appreciation but also for the hard question which incented me to widen my research from various perspectives.

I express my sincere thanks to **Prof. Ujjwal Maulik**, Head of the Department, Computer Science and Engineering, Jadavpur University, for making available all the departmental facilities and his valuable comments.

I express my sincere thanks to Mr. Nirmal Das, Research Scholar of *CMATER* Lab, Dr. Ayatullah Faruk Mollah, Asst. Prof., CSE Dept. Aliah University for their valuable suggestions and help.

I am also thankful to some other distinguished faculty members who have played a vital role to bring out the best of me.

I express my hearty regards and thanks to my beloved parents, Mr. Ajit Kumar Rakshit and Mrs. Kalpana Rakshit for the unceasing encouragement, support and constant inspiration. I would like to express my warm appreciations to my husband Dr. Dipankar Ghosh, for his incessant informative and moral support during my dissertation work.

I would also like to thank my brothers Mr. Susanta Rakshit, Mr. Agneeswar Kumar and all my family members for their love, affection and encouragement. I am deeply indebted to my grandmother, Late Smt. Durga Rani Kumar to make my life with her pure love and affection. I would also like to thank all of my supportive friends, colleagues and other well-wishers for all their love and motivation.

Last but not the least, I would like to express my heartfelt beloved appreciations to my little daughter, Ekaparna Ghosh for bearing me with my less attention to her and moral support during my dissertation work.

Pranati Rakshit
Place: Bandel

Date: 30.07.2018

Contents

LIST OF FIGURES

LIST OF TABLES

Chapter 1

Introduction

The problems of treating the arteriovenous malformation due to flow of blood through the carotid vascular system enlighten the need for study of hemodynamics in the same [1]. Though the human brain represents only 2% of the whole body weight, receives one fifth of the resting cardiac output [2]. Human cerebrovasculature consists of a set of connections of blood vessels which supplies blood to all the parts of the human brain [3][4]. Brain is considered as the most significant and essential part of human body and carotid vascular region is one of the major arterial structures of the same. Arteries and veins are two major components of carotid vasculature. The arteries distribute oxygenated blood and other nutrients to the different parts of the brain whereas the veins carry deoxygenated blood back to the heart. Hemodynamics plays a essential role in genesis and progression of some vascular diseases [5][6][7]. The clear idea on patient specific carotid vasculature and hemodynamics there in, helps physicians to detect the disease like aneurysm etc. [8]. The main objective of this study is to segment the human carotid arteries from CT angiography images and do hemodynamic analysis to predict the anomaly in human cerebrovasculature.

1.1 Hemodynamics

Fluid dynamics of blood flow, referred to as hemodynamics, provides the insight of the physical laws that direct the blood flow in the blood vessels [9]. Owing to viscosity, blood flow causes a frictional force known as hemodynamic shear stress on the luminal vessel wall [10].

Hemodynamic forces regulate blood vessel structure and influence development of vascular pathology such as atherosclerosis, aneurysm, post-stenotic dilation and arteriovenous malformation [11][12]. Atherosclerosis remains the primary cause of death in many countries and is associated with genetic predisposition and multiple risk factors such as hypertension, smoking, diabetes mellitus, social stress, viral infection etc [13][10]. Despite the systemic nature of its associated risk factors, atherosclerosis has a propensity to involve the outer edges of blood vessel bifurcation [14]. In the susceptible areas, blood flow is slow and it changes direction with cardiac cycle resulting in a weak hemodynamic shear stress [15][16]. In contrast vessel regions which are exposed to steady blood flow and bearing higher shear stress stay comparatively disease free [11][17][18]. As a result, the vascular segments with slower blood flows and weaker shear stress may develop different types of vascular anomalies. One of such vascular anomaly, called aneurysms happens to be a recognized cerebrovascular disease for over two centuries around the world [19].

Hemodynamics is the study and exploration of the dynamics and inner properties of the blood flow [20]. Different parameters, such as flow separation, shear stresses and vortex formation which have been suggested to be important hemodynamic factors, are derived from the velocity field [21]. A monolayer of cells which exists amid the blood and vessel wall is known as endothelial cells (ECs) [22][23]. Adverse cell responses which causes different atherogenesis, is enhanced by the interactions induced by hemodynamic parameters that are seemed to occur on the ECs first [24]. Fluid dynamic wall shear stress (WSS) is the frictional force (between blood and endothelial layer) per unit area exerted by the wall, is an important factor which causes atherogenesis [25][26][27]. WSS is a vector whose magnitude is proportional to the blood viscosity and flow velocity gradient normal to the surface, and which acts in a direction parallel to the local velocity at the wall [28][29][30]. It is very difficult to measure WSS *in vivo* or *in vitro*. So, it is generally computed from the local velocity distribution near the wall [31]. Therefore, knowledge of the local velocity field is needed to investigate WSS effects. WSS distribution, in turn, is highly influenced by diameter changes, separation zones, recirculation areas, turbulence, and elasticity [29].

To do the hemodynamic analysis in cerebral vasculature it is essential to understand the carotid blood flow patterns and for that it is necessary to do structural analysis of carotid arteries.

1.2 Anatomy of Cerebral Vasculature

Anatomical analysis of vessel network is necessary to know the blood flow patterns, to determine the abnormal outpouching, to detect possible obstruction in the blood flow etc. Blood supply is basically carried out with the help of the two internal carotid arteries (ICA) (referred to as the anterior circulation) and the two vertebral arteries (referred to as posterior circulation) that reconnect to form that Circle of Willis [32].

1.2.1 The Carotid Arteries

The carotid arteries deliver nutrient filled blood full of oxygen to the head and neck regions of the human body [33]. In both sides of the neck, carotid arteries are present. The right common carotid artery extends up to the right side of the neck starting from the brachiocephalic artery [34]. The left common carotid artery branches from the aorta and extends up the left side of the neck [34][35]. Details of the branches are as follows:

Common Carotid Artery (CCA): The left CCA and right CCA arise from the aortic arch and bifurcation of the innominate artery respectively.

External Carotid Artery (ECA): The branches of it supply blood to the face, jaw, neck and meninges [36]. CCA bifurcation is the starting point of it.

Internal Carotid Artery (ICA): It begins from the carotid sinus which is located at bifurcation of CCA. It serves blood to the major area of the brain. The main branches of ICA are as follows:

- ***Ophthalmic Artery (OA)*:** OA, the first major branch of ICA, continues throughout the optic canal for serving the eye area and other parts of the orbit. The most important part of OA is the central artery of retina.
- ***Posterior Communicating Artery (PoCA):*** It arises just before the last part of ICA and continues toward the back to connect the initial part of the PCA. It serves the optic tract, thalamus, chiasma, hypothalamus and the midbrain [37].
- ***Anterior Cerebral Artery (ACA)*:** The anterior section of the circle of Willis is formed by ACA. It serves the frontal as well as the medial parts of the cerebral hemispheres.

Middle Cerebral Artery (MCA): It is the prime branch of ICA and appears nearly as its direct prolongation. After entering into the sylvian fissure, it passes laterally and bifurcates into two to four branches to supply blood to the lateral sides of this cerebral hemispheres [38].

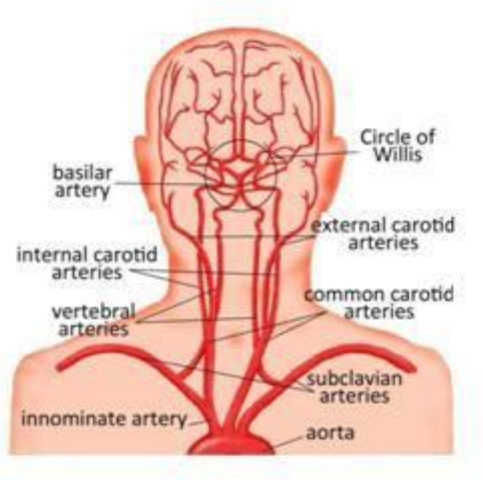

Figure 1.1 Main arterial branches of head and neck and brain (Courtesy: Medical-care/ Phace-syndrome)

1.2.2 Vertebrobasilar System

Vertebral Artery: It originates from the posterior superior part of the subclavian arteries.

Basilar Artery: Two of the vertebral arteries joined in the pontomedullary junction to form the basilar artery [39]. At the end, it divides into two parts i.e. two posterior cerebral arteries.

Posterior Cerebral Artery: These arteries supply blood to the inferior part of the temporal lobe and the occipital lobe. Circle of Willis is completed by anastomosing these arteries with the posterior communicating arteries.

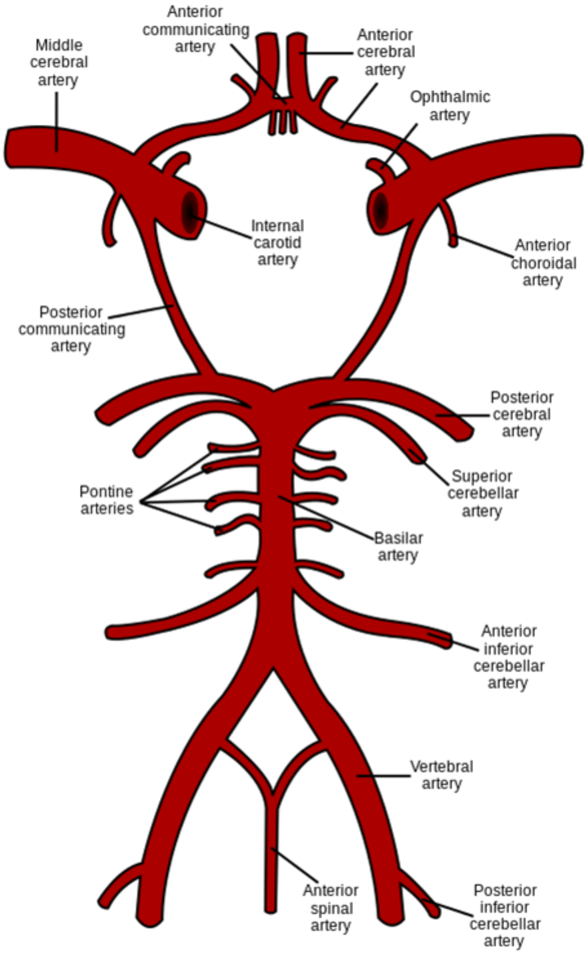

Figure 1.2 Detailed structures of carotid arteries

(Source: https://en.wikipedia.org/wiki/Circle_of_Willis#/media/File:Circle_of_Willis_en.svg)

1.3 The Role of Hemodynamics in Vascular Disease

Cerebrovascular disease is the dominant cause of death in the urbanized and developed world. Aneurysm and atherosclerosis are account for the majority of the cases. Moreover, in the past few years although mortality has slightly decreased, morbidity has not, signifying that the upgrading of diagnostic and curative techniques did not match to a massive improvement in preventive and protective measures [40]. As discussed before, several risk factors are associated with atherosclerosis, and even though such factors have a systemic nature, atherosclerotic lesions are normally being seen near bifurcations and bendings part of the arterial tree [41][42]. *In vivo* and *in vitro* experiments confirmed the hypothesis on the involvement of local hemodynamic factors in the genesis and progression of atherosclerosis [11]. Atherosclerosis is often thought to be elementary preconditions for genesis of a well known cerebrovascular disease, aneurysm [43][44].

Cerebral Aneurysm

Aneurysm, basically is some outpouch which is filled with blood and formed in the wall of a blood vessel. Cerebral aneurysm is obviously associated with artery of the brain. It is a bulge which can be developed due to weakness of the arterial wall [45]. If it becomes large enough, it can rupture and spill blood into the adjoining tissues. According to their geometry three different types of cerebral aneurysms are there [46]. The most common form of aneurysm is Saccular aneurysm. It is of rounded shape that is adjoined to an artery by a neck or stem. Berry aneurysm is another name of this type of aneurysm as the shape is just like berry. Fusiform aneurysm is that type of aneurysm which is not so common. It is of spindle-shape. Another type of aneurysm is a giant aneurysm. It is actually berry aneurysm but very large in size. It is seen mostly at the bifurcation position of the artery. Endogenous factors like elevated arterial blood pressure, the special anatomy of the Circle of Willis or the effect of hemodynamic factors, particularly originating at vessel bifurcation, are all known to be involved in the growth and rupture of an aneurysm [47][48][49]. The effects of the flow-rate ratio, bifurcation angle, aneurysmal size, parent vessel curvature are also possible risky factors which are identified [50]. Intra-aneurysmal hemodynamics is believed to be important factor related to the etiology and natural history of brain aneurysms [25][51][47][52][48].

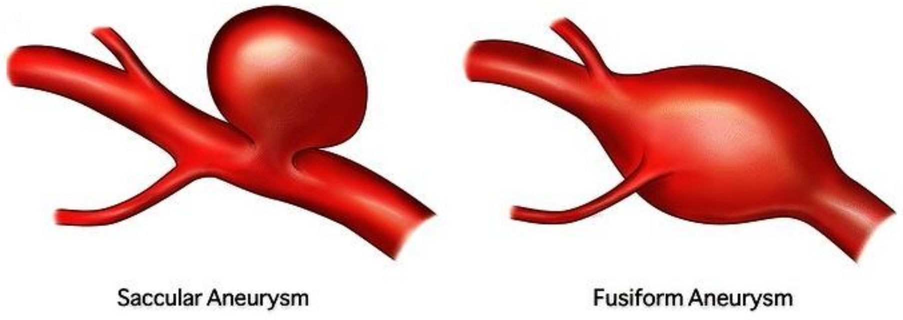

Figure 1.3 Different types of Aneurysm (Courtesy: Baylor College of Medicine/health care)

1.4 Image Acquisition Modalities

The principal imaging techniques to map the 3-D anatomy of vascular segments, which are used in clinical practice are discussed here.

1.4.1 Magnetic Resonance Imaging and Angiography

Magnetic resonance imaging (MRI) and magnetic resonance angiography (MRA) need a magnetic field as well as radio waves [53]. It uses a computer to create detailed pictures of inside of the body. It is usually used to diagnose a variety of diseases within the chest, articular cartilage, abdomen and pelvis. For a pregnant person, body MRI can be safely used to monitor the baby.

MRI and MRA are also frequently help to evaluate the blood vessels, acetabular labrum, joint capsule, and periarticular soft tissues such as bursae, tendons, and muscles [54][55][56]. One advantage of MRI includes the use of nonionizing radiation [57]. Images can be viewed into the coronal, axial, sagittal, and oblique planes and also can be plotted in thin slices (2 mm). Many advances are made in quantitative imaging techniques to detect different abnormalities. A recent meta-analysis [58] shows that, the accuracy of diagnosis of MRA was better to that of MRI in some disease like acetabular chondrolabral complex [59][60][61][62].

1.4.2 Ultrasounds

Ultrasounds are the high frequency sound waves that have frequency band above 20 KHz [63]. For medical applications the frequency range is used between 1 MHz to 20 MHz. Ultrasounds are produced with the help of a piezoelectric transducer (probe). The electrical pulses are converted into ultrasonic waves in it as the piezoelectric transducer contains piezoelectric crystals that are started to vibrate or oscillate whenever electric pulses are applied [64]. The produced ultrasound is passed through a gel medium on the skin which is externally applied to the targeted area. Different tissue has its own different acoustic impedance [65][66]. As a result the transmitted ultrasound is reflected back from the interface of two tissue and several echoes have been created. The reflected ultrasounds vibrate the piezoelectric transducer and corresponding electrical pulses are generated. From these pulses the digital image is formed. In medical imaging different ultrasounds mode are used like Amplitude mode or simply A mode, Brightness mode (B mode), C mode, Doppler mode, Harmonic mode and Pulse inversion mode. The morphologic images, produced by brightness modulation imaging technique that show the echogenity of the tissues [67][68]. Recently, some image processing techniques combine acquired 2-D images into volumes, to produce 3-D ultrasound image [69]. The pixel density of ultrasound image is quite low as compared with CT or MR angiography image [70]. Doppler ultrasound is based on the frequency shift of wave reflecting over flowing red blood cells [71].

1.4.3 Computed Tomography

A computed tomography (CT) scan is an imaging technique which results in a noninvasive investigative test that uses x-rays at various angles around the subject and it needs a computer to create images of the particular parts of the body [72]. The source and the detector rotate around the subject and a series of X-ray measurements for each rotation angle is collected [73]. To generate the helical trajectory around the subject, helical CT scanners are needed where the subject is continuously moved through the plane of the rotating source and detector [74]. The multi-row helical CT scanner is the actual state of the art scanner [75]. Here the signal is acquired simultaneously from up to four rows and thus therefore optimizing the trade-off between acquisition time, z-resolution and noise [76].

The signal resulting from the acquisition is called SINOGRAM [77]. It is represented as a series of images with detected attenuation on the x-axis and rotation angle on y-axis. The image is then reconstructed by the mechanism of inverse Radon transform on the image grid. The reconstructed image contains attenuation values expressed by Hounsfield units (HU), for which water is conventionally represented by 0. Consequently, fat is expressed with negative values, connective tissue by low positive values and calcium by high positive values. Scanners are available today in the clinical context which allow in-plane resolution < 0.5mm and slice thickness < 1mm of the anatomical structures in a single breath hold [78].

To obtain vascular imaging, radio-opaque contrast is injected intravenously. The HU values obtained by contrast agents are positive values between that of connective tissue and that of calcium. A dye (contrast agent) may be injected into the bloodstream to enhance certain body tissues. The dye contains iodine, a substance through which x-rays cannot pass through. It circulates through the blood stream and is absorbed in certain tissues, which then stand out on the scan.

Angiography is a minimally invasive medical procedure that helps physicians to diagnose and treat medical conditions [79]. Computed tomography angiography (CTA) uses an injection of iodine-rich contrast material and CT scanning thus helps to diagnose and evaluate blood vessel disease or related conditions, such as aneurysms or blockages [80].

In the present study CT Angiography is used as the preferred imaging modality due to the following reasons.

- CT angiography can perceive narrowing or obstruction in blood vessels and thus allows for potentially better corrective therapy to be done.
- CT angiography can provide more accurate anatomical detail than MRI, specially in narrow and small blood vessels.
- CT angiography is comparatively faster, non-invasive and has minimum complications.
- CT angiography is a valuable way to detect arterial and venous disease as well as structural abnormalities of the heart before any symptoms are evident or when symptoms are not clearly correlated to blood vessel disease, such as Acute Myocardial Infarction.
- There is also significantly less discomfort because contrast material is injected into an upper limb vein rather than into a catheter inserted into a large artery or vein.
- After a CT examination there exists no left over radiation in a patient's body.
- The X-rays which is used in CT scans have no immediate side effects.

1.5 Fluid Dynamics in Cerebrovasculature

Cerebral arterial disease is a consequence of the situation in which cerebral arteries become tapered or blocked which leads to reduce blood flow in the brain [81]. The arteries may be blocked with cholesterol deposition which can gradually break and cause blood clots [82]. If the vessels of the brain are smaller in size, the cholesterol deposition and the blood clots can become trapped in that, decreasing blood supply to the area. It leads to a stroke, when a region of the brain is depriving of blood. Carotid artery obstruction or blockage is one of the major reason of stroke [83].

Working with the flow within the blood vessels is going on since the middle of the last century. Due to (i) rising computational power, (ii) advancement in imaging, (iii) progress in visualization techniques and (iii) the development of novel computational algorithms, the use of computational methods in fluid dynamics to study the physiological flows concerning blood has become an area of exhaustive research. Numerical or computational models can describe the behavior of blood flow in important vessel networks quantitatively. Proper modeling also helps in explaining and assessing the relationships among vessels shape, hemodynamics, vorticity etc. which correlates to risk of failure in artery occlusion due to stenosis, or the one of aneurysm rupture [84]. When a mild stenosis is observed to be formed in the artery, biomechanical parameters which are resulted from the blood flow due to formation of stenosis and stress distribution in the arterial wall may contribute to further progression of the disease [85]. Though the blood flow in vascular structure is normally laminar in nature, it can transit to turbulence due to the pulsatile nature of the flow where the diameter of the artery decreases and consequently velocities increase [86][87].

Flow visualization techniques and non-invasive medical imaging data acquisition such as computed tomography, angiography or magnetic resonance imaging, make reconstruction of three dimensional models of blood vessels feasible [88].

Finite element simulation of hemodynamics have been frequently used to gain a better understanding of different aspects of the blood flow and in the early detection of vessels at risk and prediction of future disease progression.

1.6 Computational Fluid Dynamics (CFD)

CFD is a branch of fluid mechanics which can solve and analyze problems occurred during fluid flows [89]. It uses some data structures and numerical analysis to solve the different flow related issues.

Numerical simulations of the flow of the fluid can be performed in CFD based software. These simulations are resulted from the solutions of differential equations derived from physical conservation laws for flows [90]. CFD can provide the detail insight of hemodynamics and possibly can respond to some queries related to blood flow

[91]. The experimental and computational methods which are used extensively as the research tools used in fluid dynamics, are also applicable in hemodynamics research [92]. CFD has been established as a reliable practice for investigating 3-D flow patterns in a complex geometrical model [93]. In contrast to experimental flow studies, CFD is more suitable for altering model and flow parameters like inlet velocity, wall conditions etc. CFD can provide output with high resolution if the boundary condition information is correct. Therefore, for realistic modeling of blood flow in the artery, the geometrical data and boundary velocity data that come from in vivo measurements are very much necessary [94]. These data can be made available through medical imaging techniques. Using CFD solutions, velocity distributions for blood flows can be available easily and to extract WSS and other important hemodynamic factors from that are also not difficult. These factors suggest that CFD can be an attractive tool for hemodynamic research.

ANSYS [95] is a well-known CFD software and is used in this study for hemodynamic analysis on the cerebrovascular phantoms. It is widely used as a standard tool for finite element analysis. The Fluent module of ANSYS Workbench 16.0 is used here to analyze different hemodynamic parameters through flow analysis.

This CFD based hemodynamic analysis can be the supporting research which is also used to assess the hemodynamic parameters with the assessment of hemodynamic parameters derived from the novel digital flow based model.

1.7 The Concept of Digital Flow in Cerebrovasculature

In this work, a novel concept of digital flows in the cerebrovasculature is proposed to computationally assess the underlying hemodynamics. Hypothetical flows are conceived in the 3-D digital space inside the reconstructed arterial segments to mimic a fluid flow in a closed tubular region. The hypothetical flow in the 3-D digital space initiates from a point at one end of the tubular structure, and iteratively propagates through neighborhood points along the structure. Propagation of the flow is governed by the flow characteristics and bound by the termination conditions.

During the flow propagation, different flow characteristics like velocity and WSS are estimated at all points covered by the flow. These parameters are evaluated using the designed flow equations based on fuzzy distance transform (FDT), as discussed in details in Section 4 of the thesis.

Digital flow based analysis is used in the current work to assess the flow parameters along the cerebrovasculature, both in synthetically designed phantoms and also in segmented cerebrovasculature from patients' CTA. Vascular segments with and without aneurysm are assessed and necessary features are extracted for automatic detection of possible anomalies. A detailed discussion on digital flow based feature extraction and anomaly detection is given in Chapter 6 of the thesis.

1.8 Brief Literature Survey

Computational analysis of cerebravasculature is an important and open research problem. There are several key issues involved in the process. Existing work may be broadly confined into (i) Phantom design, (ii) Segmentation (iii) WSS distribution (iv) Aneurysmal hemodynamic analysis (v) Prediction of anomaly.

(i) Phantom Design

Phantom is basically designed for experimental validations. As it is well understood that there is natural difficulty to study real-life patient or *ex vivo* analysis, phantom based experiments are becoming popular or gathering momentum. *In vivo* or *ex vivo* analysis of carotid arterial tree is difficult as it needs active participation of patients and clinicians. Therefore, generating synthetic structures or phantoms is often favorable for experimental evaluation. In general, there are two aspect of this design; 1) physical vascular phantoms, by casting a replica of the actual vasculature, and 2) digital phantom, modeling of the vasculature, using mathematical models.

J. Zhang et al. [96] examined and compared the vessel distensibility measurements using (1) electrocardiographically gated multidetector computed tomography (CT) in a phantom; (2) a digital camera. They examined feasibility in human. Using a pulsatile flow pump, they constructed large-vessel phantoms, and measured the absolute diameter and percentage diameter changes during pulsation.

H. H. G. Hansen et al. [97] used noninvasive ultrasound elastography to detect the Atherosclerotic plaques in carotid arteries. In this paper compound radial as well as circumferential strain images were generated for a homogeneous vessel phantom with a concentric lumen subjected to different intraluminal pressures. The result of comparison of the elastographic signal-to-noise ratio (SNRe) and contrast-to-noise ratio (CNRe) revealed that compounding increases the image quality considerably compared to images from 0^{deg} information only. This work used vessel phantom for validation purpose. Above two works are based on design of physical phantom.

M. Piccinelli et al. [98] studied about the vascular geometry and identified geometric features which is allied with a specific pathological condition to focus into the mechanisms involved in the pathogenesis and progression of the atheroclerosis and aneurysm diseases. They designed the modeling framework which is based on solid computational geometry.

L. Antiga et al. [99] present a modeling framework to study patient-specific computational hemodynamics. It is designed to perform in the environment to study in large-scale. The framework incorporated image processing with geometric analysis as well as mesh generation techniques, in addition to high-level interaction and full automation. They performed image segmentation with the help of implicit deformable models taking advantage of a novel approach for selective initialization of vascular branches, as well as of a strategy for the segmentation of small vessels. The Vascular Modeling Toolkit has been used for modeling the geometry and study the computational hemodynamics.

Above two works deal with the designing of digital phantom.

(ii) Segmentation Methods

P. K. Saha et al. [100] separated arteries from veins by using a novel multiscale topomorphologic approach. This work mainly focused on opening of two isointensity objects which are fused at different position. Two fundamental challenges of this work; (i) to find local size of morphological operators, (ii) to trace continuity of locally separated regions, are met with the help of FDT, a new morphological reconstruction and a morphologic feature through a topologic fuzzy connectivity. This semi-automated segmentation method is very promising in separating arteries and veins in pulmonary CT images.

S. Basu et al. [101] stated a new hypothesis and algorithm to separate two structures having a common intensity band which is conjoined at unknown locations and scales. This work is mainly focused on segmentation of vascular structure of patients having intracranial aneurysms. CTA has been used here as imaging modality. Major challenge which is addressed here is to separate aneurysms and vessels from bone that shares common intensity space, may be with mutual tight coupling. The FDT, a morphologic function with a topologic fuzzy connectivity have been used for segmentation.

(iii) Wall Shear Stress Distribution

WSS, which is the tangential force produced by blood moving across the endothelial surface, is thought to be the major hemodynamic parameter to contribute to the aneurysm growth and rapture.

A. M. Malek et al. [11] discussed about the role of hemodynamic shear stress in atherosclerosis. Atherosclerosis is one of the primary cause of death in developed and developing world. However, being a geometrically focal disease, atherosclerosis mainly affects the outer edges of the vessel bifurcation. In these vulnerable areas, hemodynamic shear stress acting on the endothelial cell is weaker than other protected areas. Arterial level shear stress ($> 15\, dyne/cm^2$) induces an atheroprotective gene expression profile while low shear stress ($< 4\, dyne/cm^2$) is prevalent in atherosclerosis prone zones. They prepared a model to understand the focal proneness of atherosclerosis in the setting of systematic factors which may help to supervise future therapeutic strategies.

L. Boussel et al. [102] rigorously elucidates how the low WSS region and growth of aneurysm are correlated. For medical treatment or surgery or for any therapeutic decision making, determination of accurate criteria to predict aneurysm growth and consequent rupture are very important. In this context, study of intra-aneurysmal hemodynamic forces, predominantly WSS is of great importance as it plays a role in the advancement of aneurysmal disease. As low WSS has adverse effect on endothelial cells, it contributes to local remodeling of arterial wall, aneurysm growth and rapture. To determine the distributions of WSS, numerical simulations of the flow were conducted. They constructed lumenal geometries, and the calculation of radial displacement of the wall was done on a pixel-by-pixel basis. This displacement which corresponds to the local expansion of the aneurysm, was compared with the time-averaged WSS (WSSTA). After statistical analysis, the result of linear correlation demonstrates an important relationship between WSSTA and surface displacement. The results indicate that growth of the aneurysm is likely to occur in regions where the endothelial layer lining the vessel wall is exposed to abnormally low WSS.

(iv) Aneurysmal Hemodynamic Analysis

Hemodynamic analysis of vascular structure with aneurysm is studied in following works using patient specific image based CFD simulations.

A. Sarrami-Foroushani et al. [103] explored how intra-aneurysmal hemodynamics is effected by the heart rate and flow rate in internal carotid artery in the region of ICA aneurysm. Basically, hemodynamics is considered to play a significant role in the process of initiation, growth and rupture of intracranial aneurysm. To generate patient specific geometrical anatomic model of ICA aneurysm, CT scan angiogram data was collected from a 55yrs old female having saccular ICA aneurysm. With different heart and flow rates, the intra-aneurysmal hemodynamic environments for three states were studied using patient-specific image-based CFD modeling. Significant changes were found for the three different simulated states. The systolic, time-averaged WSS and pressure on aneurysm wall provides a proportional rise with the mainstream flow rate. The study established the major role of vascular geometry with respect to hemodynamics. The result also reinforced the importance of patient specific CFD simulation through which the effect of different blood flow conditions on the hemodynamics of aneurysm could be assessed.

S. M. Moore et al. [104] developed CFD models of the circle of willis (1-D and 3-D) to provide a simulation tool that can be used to identify cerebral arterial structure which is at risk and replicate clinical scenarios, such as blockage in afferent arteries. A ring-like structure which is called the Circle of Willis is found at the base of the brain beneath the hypothalamus. To maintain optimal efferent flow rates and afferent blood pressure, both models capture cerebral hemodynamic auto-regulation with a proportional–integral (PI) controller to change afferent artery resistances. The models of this present can be used to identify cerebral arterial geometries which is at risk before surgery and other clinical procedures.

(v) Anomaly Prediction

Prediction of anomalous region in vascular structure is one of the vital job for the medical practitioners for further investigation and treatment.

M. L. Raghaban et al. [105] stated that evaluating the need of surgical intervention in an abdominal aortic aneurysm (AAA) to avoid rupture, information and understanding of wall stresses are very much necessary. The knowledge of *in vivo* wall stress distribution in AAA helps to predict the rupture risk accurately, thereby serving to aid in the decision for elective repair. One necessary component of a method that would allow reliable, noninvasive estimates of wall stress in intact AAA is a suitable constitutive model that describes the mechanical behavior of the aneurysm wall.

S. M. Moore et al. [104] identified the cerebral arterial geometries which are at risk by developing some CFD model as a simulation tool. If there exists some anomaly, such as blockage in afferent arteries and absent circulus vessels, the model can detect that and check the condition before surgery or any further clinical investigation.

1.9 Motivation

The above mentioned literature strongly elucidates that hemodynamics plays a significant role in genesis and progression of vascular diseases. Cerebrovascular disease affects the blood vessels and is presently the one of the major cause of death worldwide [106][107]. The diagnosis of cerebrovascular disease usually involves an assessment of the anatomical structure of vasculature, function and the behavior of vascular blood flow. The behavior of the flow is, nevertheless, of vital importance to the cerebrovascular system. Morphology of cerebrovascular tissue is significantly influenced by the unsteady behavior of blood flow and vice-versa [108]. Therefore, the hemodynamic parameters analysis of blood flow potentially harbors a significant value for both diagnosis and risk assessment. Progression in medical imaging technology with fast enhancement of the computer technology has enabled to predict the hemodynamics of cerebral vasculature using computational analysis. Some research works have already been done using conventional CFD models. Often, such medical images are processed through complex cascades of computational and analytical algorithms. Digital topology and geometry can play some important roles in the design and development of such algorithms by enriching the scope of their target outcomes as well as by adding strong theoretical foundations enhancing their stability, fidelity and efficiency [109]. FDT based improved segmentation and digital flow based hemodynamic analysis have a great scope to be studied and implemented. Prediction of anomalous part of carotid vasculature is equally important as to diagnose cerebrovascular disease like aneurysm etc. From the literature study it can be stated that some works have been done on prediction of anomaly in vascular structure. But it will be a novel approach if the anomaly prediction or detection in human cerebrovasculature can be done using digital flow based model.

1.10 Scope of the Thesis

The main purpose of the thesis is to study hemodynamics and analyze the human cerebrovascular structure to predict cerebrovascular anomalies like aneurysm etc. As the real patient data is limited in number, mathematically generated phantom data are prepared for experimentation. So for data set- 1) synthetic phantoms have been designed; and 2) some carotid arterial structures are segmented from patient's CTA image.

Hemodynamics plays an important role in genesis and progression of different vascular diseases [110][111]. To model the hemodynamic parameters a novel digital flow based approach has been proposed in the current work. The changes in hemodynamic parameter like velocity, WSS etc are modeled using the concept of digital flows.

For the CFD based or finite element based analysis, ANSYS has been used on some cerebrovascular structure with and without aneurysm.

Finally, to classify the normal and anomalous regions, the features extracted from the digital flow analysis are used. Different hemodynamic parameters like velocity, WSS etc and some flow based parameters are used as the feature set to classify the anomalous part and normal part of the cerebrovascular structure.

The overall scope of the thesis can be summarized as follows:

- Develop methodology to reconstruct patient specific carotid arterial geometries.
- Segmentation of carotid arterial structure from real CTA image.
- 3-D Digital flows are conceived and implemented to simulate hypothetical fluid flow through the phantom and segmented human cerebrovasculature.
- To uncover the hemodynamic characteristic,
  - Hemodynamic parameter models are developed and analyzed using the concept of digital flow.
  - CFD based flow analysis is also done on some cerebrovascular structure.
- Anomalous parts of the carotid arterial structures are classified.

1.11 Organization of the Thesis

The thesis is organized into seven chapters. **Chapter 1** provides an introduction to the thesis. It includes brief overview of each of the main modules of the work presented in the thesis. In **Chapter 2** the concept of design of digital phantoms of some cerebrovascular structures have been discussed. The modeling of 3-D arterial structures with the help of self developed GUI is presented. Carotid arterial structure reconstruction methods are described with the help of original *in vivo* data of a CTA image of a real patient. **Chapter** 3 elucidates the methods of segmentation of carotid vasculature from human CT angiography image. This is a key module for hemodynamic analysis in human cerebrovasculature. **Chapter 4** describes the concepts of *3D* Digital flow. The concepts of the digital flow algorithms are established and illustrated in this chapter. The theory of digital flow is described in detail. Hemodynamic analysis using digital flow has been discussed and analyzed to develop the velocity and WSS model in **Chapter 5.** CFD based flow analysis using ANSYS and comparison of hemodynamic parameters of cerebrovascular structure with and without Aneurysm are also explained in this chapter. In **Chapter 6,** anomaly detection in cerebrovasculature and classification of anomalous and normal regions of carotid vasculature are discussed and performances of different classification model are analyzed. Designing the feature set from different hemodynamic parameters and some flow based parameters which are used to classify the anomalous part and normal part of the cerebrovascular structure are also discussed here. **Chapter 7** concludes with the summarizing statements and the future scope of the thesis.

Chapter 2

Design of Cerebrovascular Phantom

In vivo or *ex vivo* analysis of cerebrovascular system is a crucial job to do any further study on that. But it is complicated as well as time taking task which needs to be handled carefully by the high-quality clinicians. Patient’s consent and participation are also needed to capture the *in vivo* vascular images. So as much real medical data is important to analyze and validation purpose, construction of synthetic structures (phantoms) are equally important to generate simulated results. Therefore, generation of these phantoms are often beneficial for experimental evaluation of new computational techniques for flow analysis at the laboratories as well as they relieve the patients from repeated involvement in the experimental procedures. Owing to the perceptible simplicity of the design, phantom based simulation experiments are becoming very popular in experimental biology. In general, there are two different approaches for the design of these phantoms: 1) modeling of physical vascular phantoms by casting a replica of the actual vasculature, and 2) digital modeling of the vasculature, using approximate mathematical models. Both have individual merits and demerits. Researchers sometimes work on both of the models to validate their experiments as in work [112]. However in the present study, work has been done only with the mathematical phantoms.

Reconstruction of arterial geometry from medical images must be completed before CFD simulations or flow analysis in phantom. This reconstruction work has been carried out in several steps. An overview of geometry construction methods are given in *Section 2.1*. In both physical and digital phantom of arteries blood flow analysis is done by different methods. Various parameters need to be modeled to simulate the digital flow in synthetic phantoms. By using computer models to simulate the flow in arteries, much more information can be gathered than what physical experiments can provide. Both the spatial and temporal resolution of the simulations is far superior to any measurement methods currently available. These simulations can be done causing minimal disturbance to the patient, as only a digital 3-D image of the area of interest is needed to perform simulations. This also minimizes both the geographical and time limitations of physical experiments, as the simulations may be performed anytime, anywhere. They may also be performed several times, using different physical parameters, e.g. to simulate different treatment methods. To simulate the CTA images of the patterns a 3-D GUI, developed using QT [113], Insight Toolkit (ITK) [114], Visualization Toolkit (VTK) [115][116] and for visualization ITK-snap [117] have been used.

2.1 Literature Review

There are several existing works available in the literature, both on the design of physical & digital phantoms while most of the prior works focus on the development and experimental analysis using physical phantoms, some recent works have also discussed the development of digital phantoms. Some of the literatures are on both, the design of physical as well as digital phantom.

(i) Design of Physical Phantom

Z. Cai et al. [118] designed the Dynamic Arterial Tree Phantom. The starting point of this particular phantom is the aorta and continues to the arteries in the feet using the bolus chasing techniques. The angles are chosen as 30°, 45° and 60° between the joined vessels. First, using AutoCAD, the structure of phantom is made. Then it is implemented physically using silicone and wax. There are five parts in arteries, which are integrated by connectors. No leakage should be present at the region of connection. Later, aneurysms are added according to requirement.

B. He et al. [119] developed physical phantom to accurately estimate the 3-D *in vivo* activity distribution for dose estimation in targeted radionuclide therapy.

(ii) Design of Digital Phantom

D. L. Collins [120] stated that validation is an vital step after giving conception and implementing any new algorithm of medical image processing to ensure the fulfillment of all requirements. Though the algorithm must be evaluated on real data, a comprehensive validation needs the use of simulated data as it is impossible to set up ground truth using *in vivo* data. The authors designed a realistic, digital, high-resolution, volumetric phantom of the human brain. This 3-D digital brain phantom consists of ten volumetric data sets that define the spatial distribution for different tissues where voxel intensity is proportional to the fraction of tissue within the voxel. The digital brain phantom can be used to simulate tomographic images of the head. Furthermore, this phantom may be used for different modalities and it is ideal tool for testing intermodality registration algorithms.

R. P. Wood et al. [121] used the perfusion imaging as it is very useful to assess the acute stroke. They designed a uniform phantom which mimicks the brain vasculature. An angiographic system tested the phantom and from the particular result, a time density curves (TDC) were derived. Using the Fick principle, flow area under the curve and maximum slope were calculated. The TDCs were physiologically applicable and 25% percentage error was presented in the calculated flow values. It can be a clinical calibration tool for the existing imaging perfusion measurement systems. It will be very helpful for the systems to analyze the quantitative values of the tissue at risk and ischemic core size more meaningfully. They basically developed a systematic way to assess the reliability of the existing perfusion systems.

E. R. Melhem et al. [122] developed carotid bifurcation phantom models with different degrees of stenoses. The exactness of vessel lumen representation was evaluated on contrast enhanced 3-D MR angiography images. That is obtained from the inverse Fourier transform (IFT) of different k-space percentages. It decreases motion related artifacts and remove the need for cumbersome image post processing and high contrast agent.

G. Cloutier et al. [123] presented a process of developing a novel multimodality vascular imaging phantom. It will be compatible with each radiographic imaging technique, namely digital subtraction angiography, CTA, B-mode echography and MRA. The designed phantom is used for the calibrating multimodality images of cylindrical vessels of size varying between 0.93mm and 6.24mm. This is used for optimizing peripheral MRA acquisition parameters to quantify peripheral vascular stenoses. In the vascular phantom, a nitinol stent with tantalum markers was recently implanted for evaluating artifacts produced on MRA and CTA imaging.

(iii) Design of both Digital and Physical Phantoms

P. K. Saha et al. [100][112][124] studied on physical and digital phantom design. An experiment was done with the help of an actual vessel cast of a pig lung that was used in these studies. For generating a pig pulmonary vessel cast phantom, there are two steps involved in it. In first step the animal was exsanguinated and in second step pneumonectomy was performed. For creating a cast of the pulmonary arterial and venous trees, a quick hardening compound was injected into the vasculature. Then CT scanner digitizes the vessel cast phantom for subsequent experimental validations. Computer-generated phantoms are used, as an assembly of two objects which run quasi-parallelly across the slice direction with different types of geometry and variable levels of scale, noise, overlap and fuzziness. The evaluation of the object segmentation performances was done by these phantoms qualitatively as well as quantitatively.

As discussed before, for assessment of mean differences quantitatively various physical vessel phantoms can be used between the clinical studies and experiments that are truly based on phantom [96][125][97]. Real-life simulation is done by physical phantom. The implementation of this type of setup is very expensive. Physical phantoms are not vital in most of the theoretical studies. The basic purpose is served by accurate or approximate digital phantoms. For recreating the physical structure in the digital space, it is important to use mathematical modeling and three dimensional graphical rendering. Various works have been done on digital phantom design [126][98][99] and subsequent computational analysis [127][128] in contemporary literature. More specifically Bogunović et al. [129], have widely covered the geometrical structure of carotid siphon. An approach for objective geometric characterization of the carotid siphon was done by them and it was parameterized by a set of anatomical landmarks.

2.2 Research Objective

Structural scrutiny of human cerebrovasculature is essential for in-depth clinical understanding of the carotid blood flow patterns, determination of abnormal outpouching, detection of possible shrinkage or blockage in the artery etc. and to delineate the underlying hemodynamics. Experiments based on digital phantom are becoming very popular due to the expected difficulty in real-life patient study. Due to the acceptability of digital phantoms in a broad range of simulation experiments, design of digital cerebrovascular phantoms is of active interest.

2.3 Theory & Methodology

In this section, the theory and notations involved in the mathematical simulation of the vascular phantom as well as the methodology to design the digital phantom, are discussed.

A three dimensional (3-D) cubic grid, or simply a cubic grid, is represented by $\mathrm{Z}^3 \mid \mathrm{Z}$ is the set of integers. A grid point which is often referred to as a voxel or simply a point in 3-D space, is represented by a triplet of integer coordinates and is an element of Z^3. In this present study conventional 26 adjacency [16] is used, i.e., two points $\mathrm{p} = (\mathrm{x}_1, \mathrm{x}_2, \mathrm{x}_3)$, $\mathrm{q} = (\mathrm{y}_1, \mathrm{y}_2, \mathrm{y}_3) \epsilon \mathrm{Z}^3$ are adjacent if and only if $\max_{1 \leq i \leq 3} |\mathrm{x}_\mathrm{i} - \mathrm{y}_\mathrm{i}| \leq 1$, where |.| returns the absolute value. Two adjacent points are referred to as neighbors of each other; the set of 26-neighbors of a point excluding itself is denoted by $\mathrm{N}^*(\mathrm{p})$. Now a sphere $S(\mathrm{p}, \mathrm{r})$, with center at $(\mathrm{x}_\mathrm{c}, \mathrm{y}_\mathrm{c}, \mathrm{z}_\mathrm{c})$ and radius r is defined as

$$(x - x_c)^2 + (y - y_c)^2 + (z - z_c)^2 = r^2$$

The points on the sphere with radius r can be parameterized as $\mathrm{x} = \mathrm{x}_\mathrm{c} + \mathrm{r}\cos\theta\sin\varphi$, $\mathrm{y} = \mathrm{y}_\mathrm{c} + \mathrm{r}\sin\theta\sin\varphi$ and $\mathrm{z} = \mathrm{z}_\mathrm{c} + \mathrm{r}\cos\varphi$ where $0 \leq \theta \leq 2\pi$ and $0 \leq \varphi \leq \pi$. Two points p_1 and p_2 in Z^3 may be connected by a set of adjacent points $\{\mathrm{p}_1, .., \mathrm{p}_\mathrm{i}, .., \mathrm{p}_{\mathrm{i}+1}, .., \mathrm{p}_\mathrm{n}\}$. Then a tubular structure $\mathrm{T}(\mathrm{p}_1, \mathrm{p}_\mathrm{n})$ in Z^3 having uniform radius may be defined as a collection of spheres $\mathrm{S}_1, \mathrm{S}_\mathrm{i}, \mathrm{S}_{\mathrm{i}+1}, \ldots, \mathrm{S}_\mathrm{n}$ having radius r and the set of adjacent center points, $\mathrm{C} = \{\mathrm{p}_1, .., \mathrm{p}_\mathrm{i}, \mathrm{p}_{\mathrm{i}+1}, .., \mathrm{p}_\mathrm{n}\}$ respectively. When the points p_1 and p_n are connected through a digital straight line then the corresponding tubular structure forms a simple tubular structure or a pipe. Figure 2.1 (a-c) shows 3-D rendering of a pipe and some other tubular structures with varying complexities, respectively.

Two tubular structures $\mathrm{T}_1(\mathrm{p}_1, \mathrm{p}_\mathrm{n}); \mathrm{p}_1, \mathrm{p}_\mathrm{n} \in \mathrm{C}_1$ and $\mathrm{T}_2(\mathrm{q}_1, \mathrm{q}_\mathrm{m}); \mathrm{q}_1, \mathrm{q}_\mathrm{m} \in \mathrm{C}_2$ in Z^3, may be connected to each other when, $\mathrm{C}_1 \cap \mathrm{C}_2 \neq \emptyset$. Figure 2.4 shows sample images with connected tubular structures. In a tubular structure $\mathrm{T}(\mathrm{p}_1, \mathrm{p}_2)$ in Z^3, the spheres at the two endpoints p_1 and p_2 may have different radius values r_1 and r_2. Then, the radius of the intermediate sphere r_i with center point p_i may be estimated as follows:

$$r_i = r_1 + \Delta r \frac{||p_i - p_1||}{||p_1 - p_2||}; if\ r_2 > r_1$$

$$r_i = r_1 - \Delta r \frac{||p_i - p_1||}{||p_1 - p_2||}; if\ r_2 \leq r_1$$

where, $\Delta r = |r_2 - r_1|$ and $||p_i - p_j||$ is the length of the digital path between p_i and p_j in C. A tubular structure T having varying diameter is illustrated in Figure 2.5. The intermediate points between the end points p_1 and p_2 in C are populated using different mathematical functions including non-linear interpolation techniques, according to the geometry of the physical vasculature.

Piecewise interpolation technique using cubic Bézier curves have been used to generate multiple tubular structures to design carotid vasculatures synthetically, part by part, to replicate to complete human arterial tree. A Bézier curve is a parametric curve that uses Bernstein Polynomial as a blending function. A Bezier curve of degree n (order $n + 1$) is represented by: $R(t) = \sum_{t=0}^{n} b_i B_{i,n}(t)$, $0 \leq t \leq 1$. The coefficients b_i are the control points or Bézier points and together with the blending function $B_{i,n}(t)$ determine the shape of the curve.

VTK [116], an open-source, freely available software system for 3-D computer graphics is used here for rendering of the synthetic structures. QT [18] which is a cross-platform application framework and is widely used for developing application software with a graphical user interface (GUI), is also used. The ITK-SNAP software [19], [20] is used here for generating the 3-D visualizations.

2.4 Design of Simple Structures

Using the above mentioned methodology, first some basic structures are generated for testing and simulation. Figure 2.1 is the first generated data where structure looks like a pipe (Figure 2.1(a) almost straight or with little bend and Figure 2.1(b) with bends).

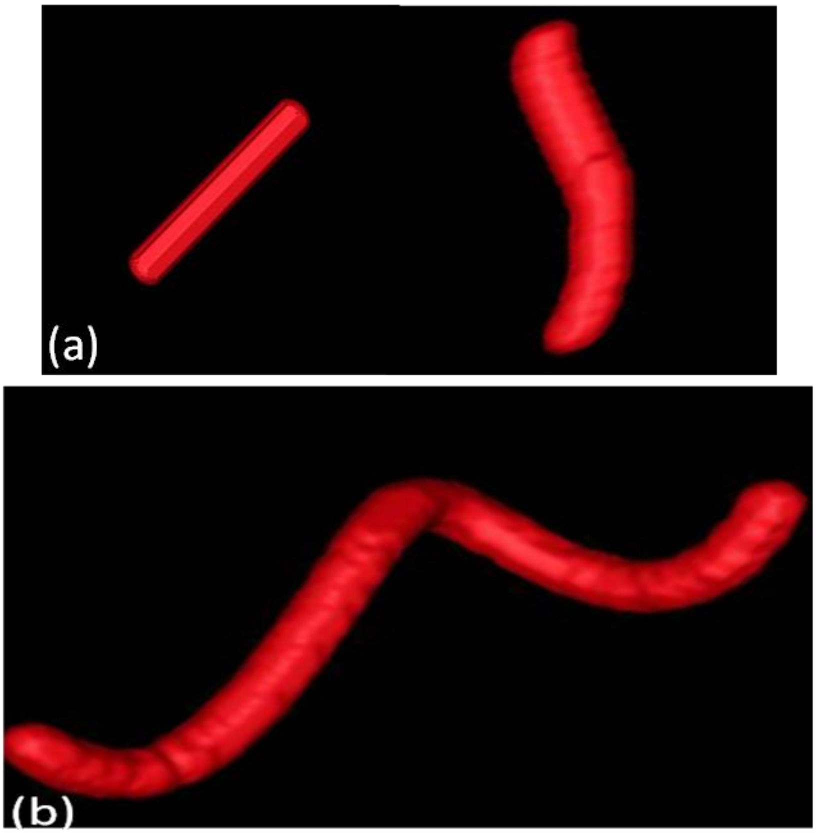

Figure 2.1 3-D rendering of simple tubular structure a) with little bend or no bend b) with bend

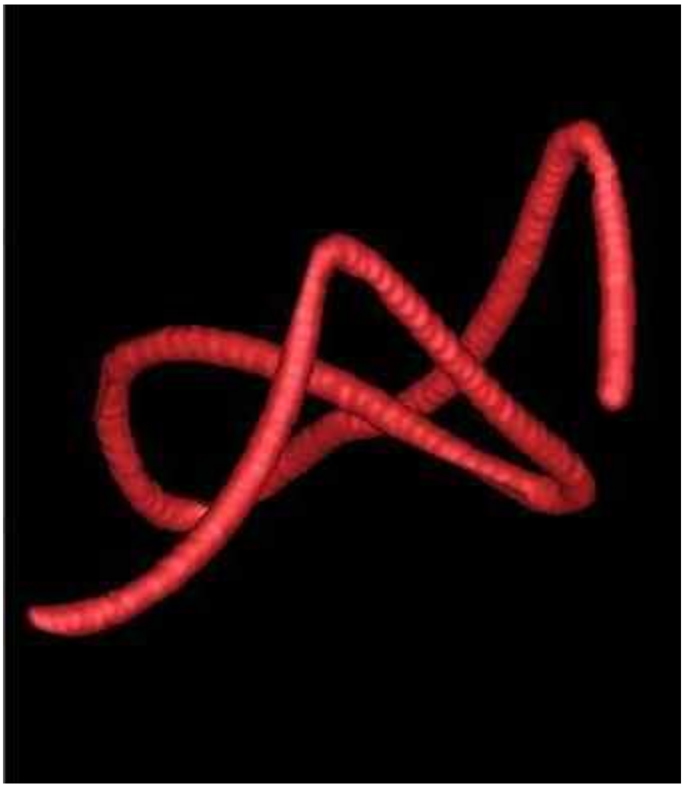

Figure 2.2 Tubular structure with multiple complex bends.

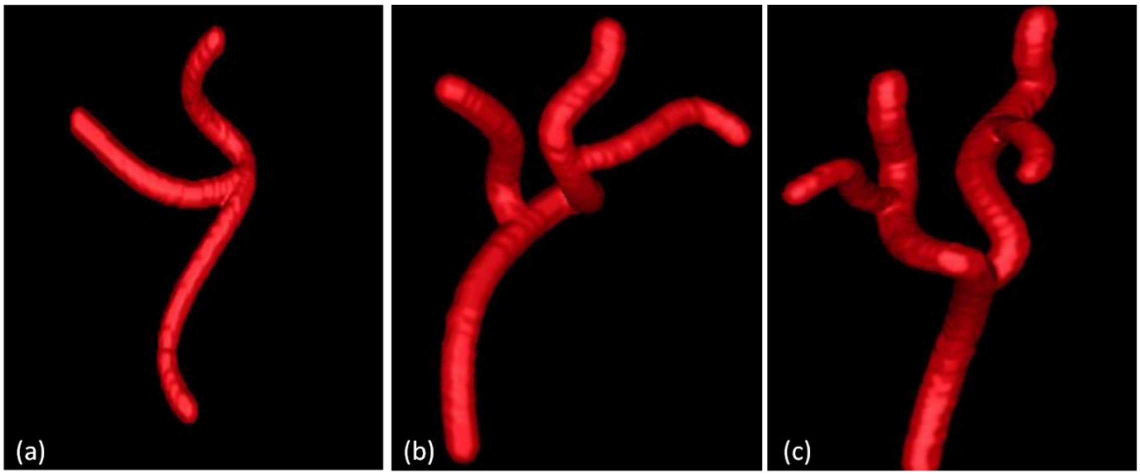

Figure 2.3 Different connected tubular structures a) and b) simple bifurcation c) complex bifurcation.

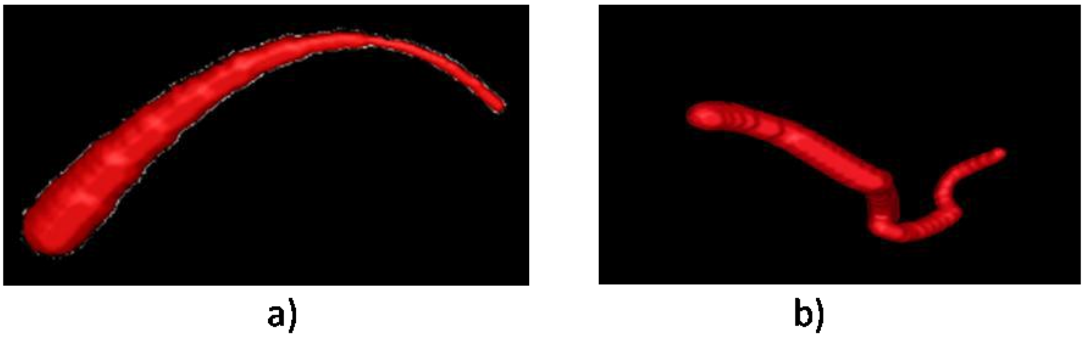

Figure 2.4 Curves with varying diameter

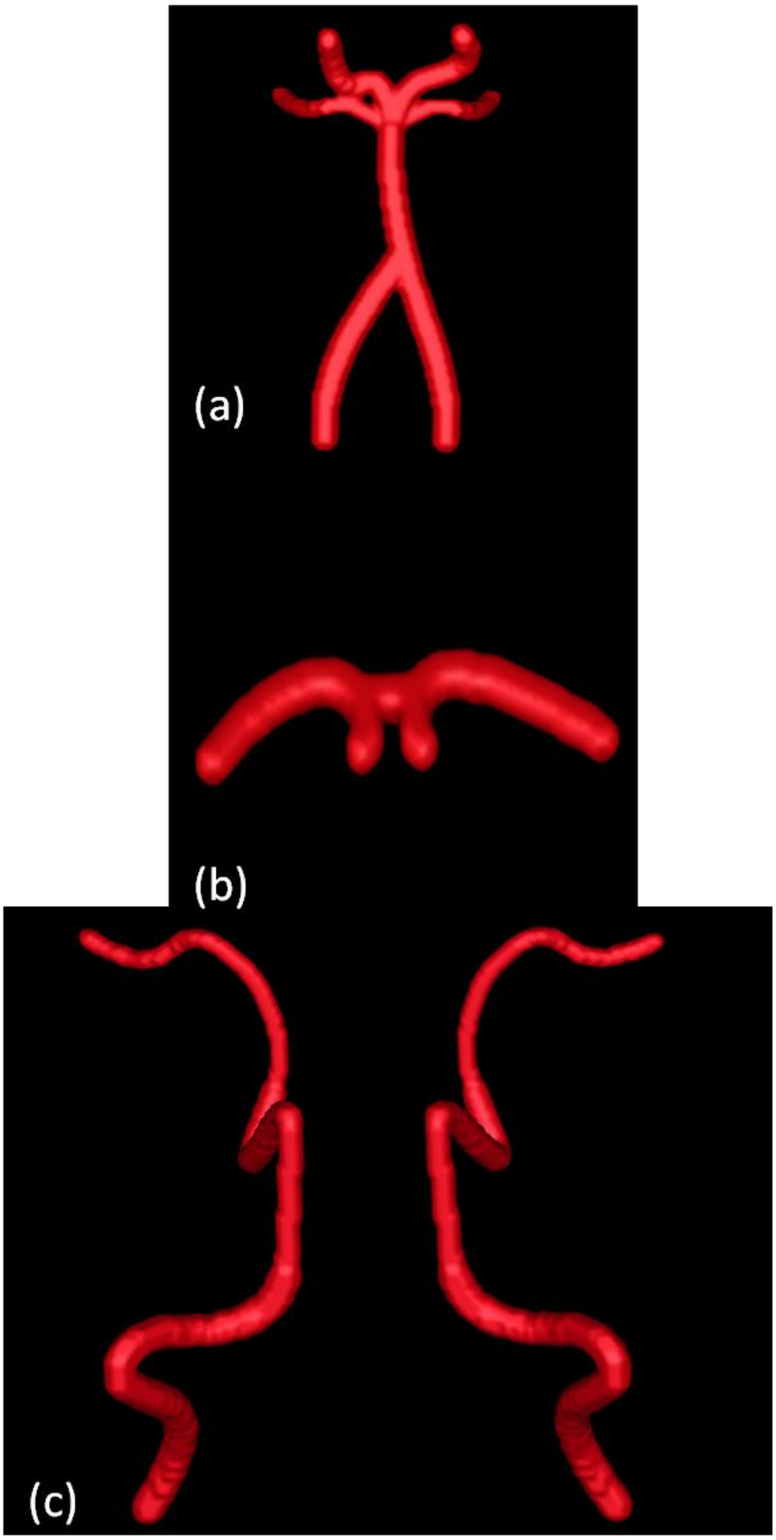

Figure 2.5 Different carotid arterial segments, (a) Basilar Artery, (b) ACA, (c) ICA

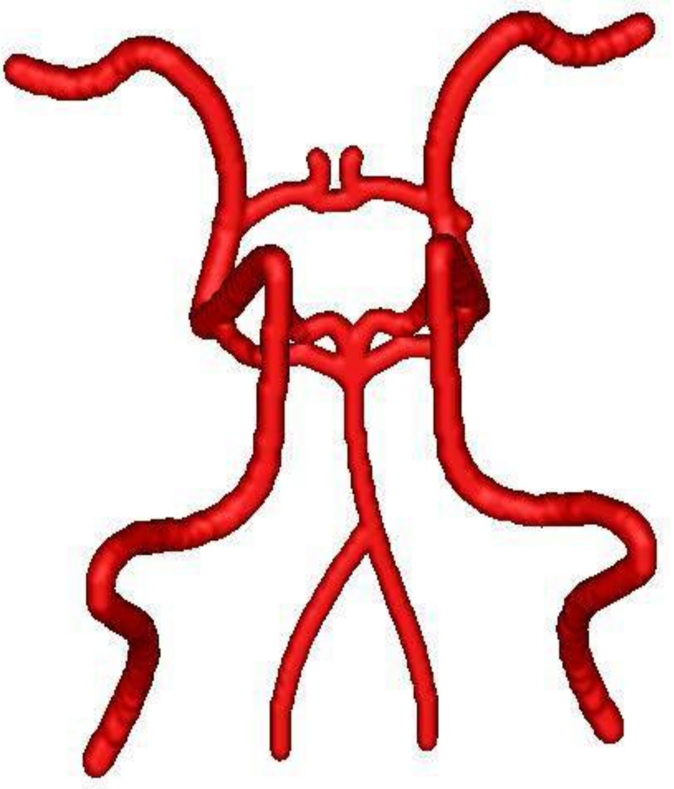

Figure 2.6 3-D rendering of a complete cerebrovasculature around the Circle of Willis

According to the present study these types of structures are common in carotid region. In Figure 2.2 some more complexity is inserted in the form of a simple curve. The curves may have single or multiple branches, as shown in Figure 2.3. Some curves with variable radius is shown in Figure 2.4.

2.5 Design of Complex Digital Phantoms

After designing some simple structures, a few complex digital phantoms are generated for detailed hemodynamic analysis. These complex structures can be classified in two categories; 1) approximate synthetic structures that mimic the real orientation of the cerebrovascular tree that do not use any real CTA data as reference and 2) the accurate phantoms that are generated with the help of a 3-D GUI, with reference to patient's CTA data.

2.5.1 Approximate Structures

Approximate digital phantoms are generated in parts, keeping in mind the approximate geometry of the different structural sub-parts in the cerebrovascular tree.

In this process, at first the Basilar Artery (Figure 2.5 (a)), the ACA (Figure 2.5 (b)) and the left and right ICAs (Figure 2.5 (c)) are designed. The complete cerebrovascular phantom, around the Circle of Willis is then generated and shown in Figure 2.6. The cerebrovascular phantoms are designed and visualized with 3-D rendering support [130][117]. The volumetric data is generated in accordance with the actual arterial tree, present around the Circle of Willis of human brain. It may be noted that the current structure is approximate and does not map any real data. These approximate structures are used to study the arterial curvatures, bifurcations, joins and possible modeling of digital-fluid flows as discussed in the subsequent Chapter of the thesis.

2.5.2 Accurate Structure using in vivo Data

CTA, already discussed in Chapter 1, is a medical imaging procedure that utilizes computer-processed X-rays to produce tomographic images for different 'slices' of specific areas of the body. These cross-sectional images are used for diagnostic and therapeutic purposes in various medical disciplines [131][132]. The images are in DICOM format which is the standard for medical imaging.

Accurate arterial phantoms are designed by working with *in vivo* data samples, and by generating ground truth markers with the help of a self-developed Qt based annotation GUI tool (Figure 2.7). It may be worth mentioning in this context that existing VMTK library [133] may serve the similar purpose, in analysis of fluid flow dynamics. However, the necessity to generate accurate phantoms with possible options for modeling of non-vascular structures has prompted us to develop the current model. 3-D phantoms as well as the generated accurate arterial structure (Figure 2.8) also help in digital hemodynamic modeling in carotid vasculatures that can eventually help in detection of structural anomalies in vasculature, like arterial blockage, abnormal arterial outpouching etc, and also in estimation of arterial rupture risks. The real CTA images are first uploaded in the GUI and then the approximate start and end points and the corresponding radius values are fed to the algorithm.

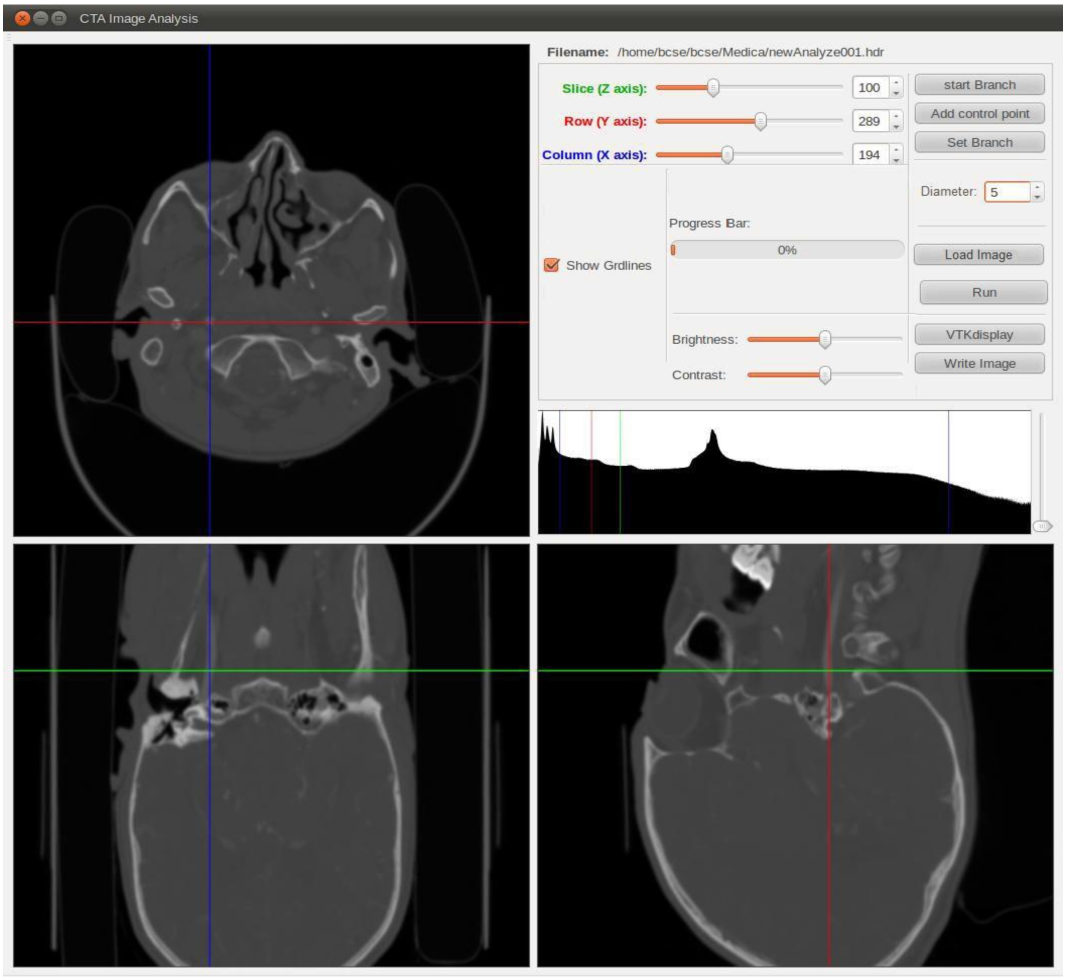

Filename: /home/bcse/bcse/Medica/newAnalyze001.hdr

Slice (Z axis): 100

Row (Y axis): 289

Column (X axis): 194

Diameter: 5

☑ Show Grdlines

Progress Bar: 0%

Figure 2.7 QT based GUI

The developed software then generates the synthetic structure using the algorithm, already discussed in Section 2.3 of the thesis. The following images illustrate the data which are generated with the designed GUI tool and a snapshot of the real data in axial, saggital and coronal views. Figure 2.8 shows digital phantoms of the most vital arteries of cerebrovasculature, the ICA and ACA. Figure 2.9 provides two views of the combined structure of approximate digital phantoms.

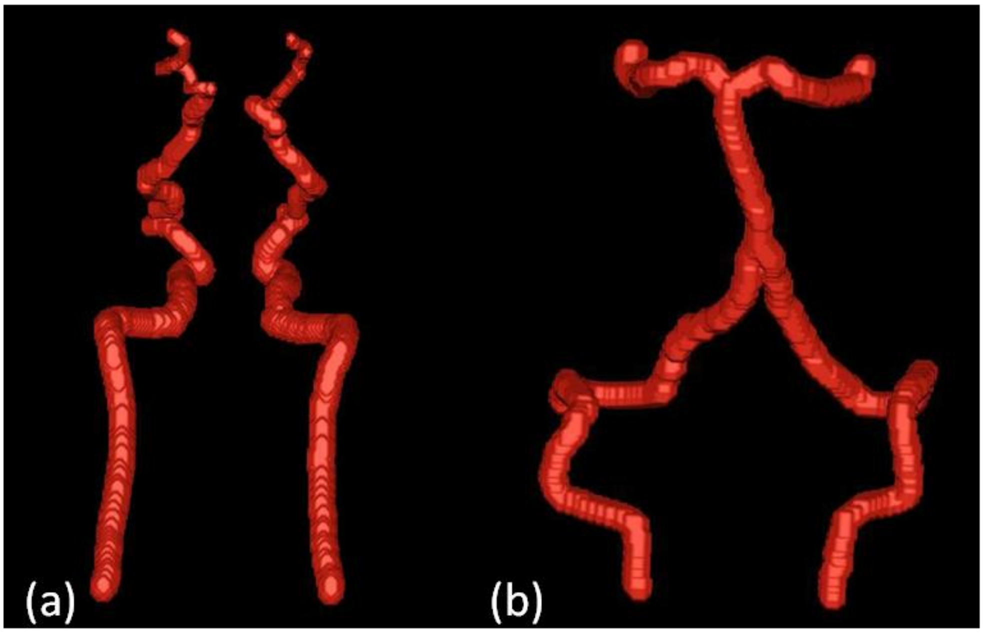

Figure 2.8 Arterial segment of (a) ICA (b) ACA of accurate phantom

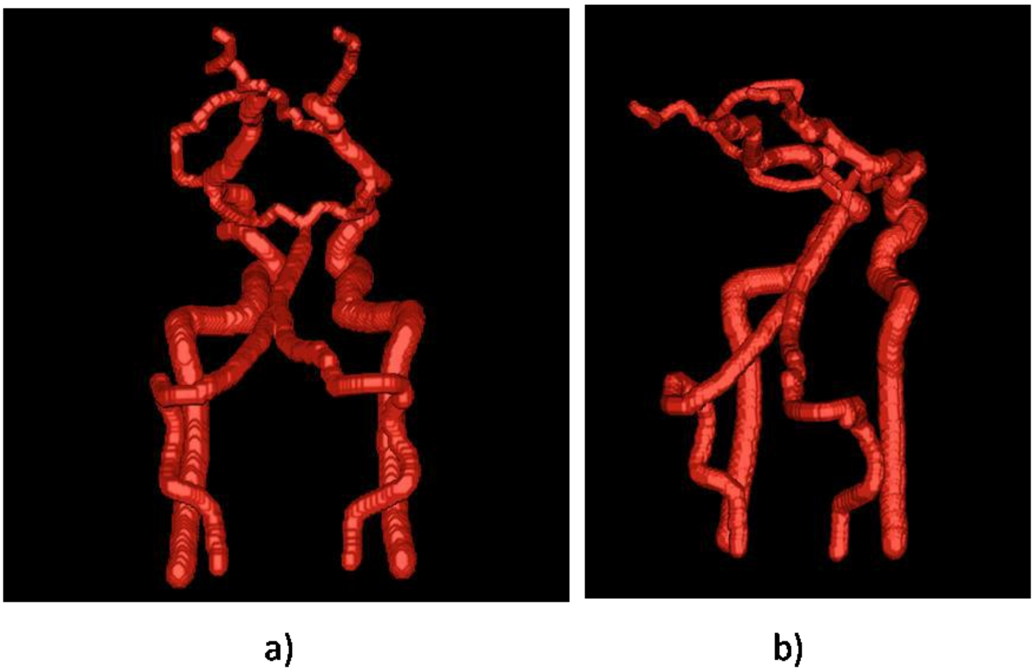

Figure 2.9 3-D rendering (two views) of the accurate phantom using the popular ITK-snap software a) front view b) side view

2.6 Discussion

Advantages of making phantoms of vascular structure to do in depth research of vascular diseases are: firstly, phantoms can imitate different types of vascular diseases and provide various blood flow signatures and secondly they can be used repeatedly for experimentation.

The theory and methodology used to design the phantoms of human cerebrovascular structure, is described in this Chapter. The sphere based approach is used here to design the 3-D mathematical model. a custom-designed 2-D/3-D user interface is used to develop the approximate and accurate phantoms. Multiple tubular structures with varying diameters are combined to generate the complete arterial phantom, around the Circle of Willis, situated at the base of the brain.

The developed framework proposes a robust solution to multi-level vascular branching with varying vessel diameter.

Chapter 3

FDT and its Application in Segmentation of Cerebrovasculature from Human CTA

Segmentation of cerebrovascular structure from human CTA image is an important task before subsequent hemodynamic analysis in the segmented vasculature. Automatic or semiautomatic segmentation of the vasculature from its surroundings is an active area of research in the field of medical image analysis. It helps researchers as well as clinicians to explore the underlying hemodynamics, which is one of the major factors in determining one’s vascular health. In this present study, carotid arteries which supply oxygenated and nutrient-filled blood to entire cerebral system, are in the center of interest. Anatomical analysis of the vessel network is the first step towards exploration of the blood flow patterns in the vasculature. The anatomy of carotid arteries along with *Circle of Willis* is already explained in Chapter 1. From the introductory discussion of first Chapter it is known that the left and right internal carotid arteries, anterior and posterior cerebral arteries (left and right), anterior and posterior communicating artery form this circular vasculature. The basilar and middle cerebral arteries are also part of this circle as already discussed.

The present study focuses only on the segmentation of vasculature using mathematical model from human cerebral CTA images. CTA images are 3-D grayscale images where each voxel is represented by 8 bit character or 16 bit unsigned short value. Numeric value of a voxel denotes the intensity of the voxel. Artery, veins and soft tissues acquire small intensity values, whereas bones take high intensity values. Arteries and veins are denoted together as vessels. Intensity of vessels and soft tissues are highly overlapping.

In this present study, the main interest is in segmentation of arterial tree of human cerebrovasculature.

It has been observed that in general intensity of vessels lies between 130 and 500 Hu(Hounsfield unit), as described in reference [124], but there is almost zero overlapping around the middle point of this intensity scale. Hence, voxels within this intensity range are considered as object voxel and rest of the intensity regions are taken as background.

FDT based existing works on segmentation of CTA images [100][124][112][134] need a lot of human interactions. Another most challenging part of the segmentation process is the segmentation of vessel and bones in the region of overlapping intensities. In CTA images of human brain, there are high overlap of intensities among the regions of soft tissues, bones, arteries and veins which makes the images fuzzy in nature and accurate segmentation a challenging work. The concept of FDT has been widely used before in various segmentation algorithms [135][136][137][138][109]. Researchers have adopted various FDT-based and fuzzy morphoconnectivity-based approaches to separate objects residing in overlapping intensity regions [100][124].

The present study illustrates the design of cerebrovascular phantoms using FDT-based geodesic paths [139]. An improved segmentation method of human carotid vasculature also has been developed [140].

In the subsequent discussions, the underlying theory and notations related to the proposed algorithm will be introduced first, followed by the literature review, methodology of proposed algorithm and experimental results.

3.1 Theory and Notations

In this Section, the basic theoretical foundation of this work is presented. The concept of Adjacency, Distance Transform, FDT, Fuzzy membership construction are discussed briefly.

3.1.1 Adjacency Concept

A 3-D cubic grid is expressed by $\{Z^3 \mid Z$ is the set of positive integers$\}$. A point on the grid, often referred to as a voxel, is a member of $Z^3$and is denoted by a triplet of integer coordinates. Conventional 26 adjacency [141] is used here, i.e. two voxels P=(x_1, x_2, x_3)

and $Q=(y_1, y_2, y_3) \in Z^3$ are adjacent if and only if, $\{\max(|x_i - y_i|) \leq 1 \mid 1 \leq i \leq 3\}$, where $|\cdot|$ means the absolute value. Two adjacent points in a cubic grid are often referred to as neighbours of each other. Twenty-six neighbors of a voxel P excluding itself is symbolized as $N^*(P)$.

3.1.2 Binary Image

A k-dimensional binary image can be defined as a function, F from the elements of an $n_1 \times n_2 \times \ldots\ldots \times n_k$ array to $\{0,1\}$. The elements are called as pixels if $k = 2$ and are called as voxels if $k \geq 3$. By convention, voxels having value 0 are called background voxels and value 1 is used to represent foreground (or object) voxels.

In case of 3-D image, $F: \Omega \subset \mathrm{Z}^3 \rightarrow \{0,1\}$, where $\Omega = n_1 \times n_2 \times n_3$. Hence an object $\mathcal{O}$ is represented as a set of all the foreground voxels: $\mathcal{O} = \{ p \in \Omega | F(p) = 1\}$. The elements of its complement, $\mathcal{O}^C$, forms the set of background voxel in Ω. Here a voxel or point (P) is represented by a triplet of integer coordinates i.e. $P = (x_1, x_2, x_3)$. Concept of conventional 26 adjacency [142] is used here.

3.1.3 Distance Transformation

Distance transformation (DT) has been widely used in the field of general image processing as well as in medical image processing. Distance has a wide variety of application like detection of clusters and regularities in an image, dissection of regions into pieces, detection of extended part of an object, detection of centerline of an object [143] etc.

DT is a basic geometrical operator which converts a binary image into a gray scale image, where the gray scale value at each pixel location is proportional to the distance of the corresponding pixel in the binary image from the nearest background pixel. In practical, distance is calculated locally in a small neighborhood for each and every pixel. Besides Euclidean distance, two other popularly used distance metrics are city block distance and chess board distance [143].

In 2-D space, city block distance (d_4) between two given pixels locations $(x_1, y_1), (x_2, y_2)$ respectively, can be mathematically expressed as,

$$d_4\big((x_1,y_1),(x_2,y_2)\big) = |x_1 - x_2| + |y_1 - y_2|$$

In contrast, chess board distance (d_8) between the same two pixels in 2-D space can be mathematically expressed as,

$$d_8\big((x_1,y_1),(x_2,y_2)\big) = max(|x_1 - x_2|, |y_1 - y_2|)$$

The propagation of city block distance from a single point is shown in Figure 3.1. Distance is propagated from a single center point numbered as 0. If one can connect the equidistant points, it will take the diamond like shape that is why city block is also called diamond distance.

The Figure 3.2 shows the propagation of chess board distance from a single center point marked by 0. If the equidistant points are connected, it will take a square like shape. Chess board distance is sometimes also called square distance.

The objective of a good DT algorithm is to make a close approximation of the Euclidean distance. Mathematical expression of DT is defined in[144].

Let, given a 2-D binary image $F(x,y)$,

$$\mathcal{O} = 1, set\ of\ object\ pixels$$

$$\mathcal{O}^C = 0, the\ set\ of\ background\ pixels$$

A distance map $D(\mathcal{O})$ is an image such that for every pixel, $(x,y) \in O$ there is a corresponding pixel in $D(\mathcal{O})$ where,

$$D(\mathcal{O}) = min(distance|(x,y), \mathcal{O}^C|)$$

This concept of DT can be expanded to any arbitrary dimension as described in [145][144]. DT is an essential step in many 2-D/3-D image processing tasks [64] like merging and segmentation, clustering and matching, finding out centre of maximal discs/centre of maximal balls, skeletonization etc. The distance transformation algorithm works on a binary image and converts it to an image where the value of each foreground pixel/voxel depicts the distance from the nearest background pixel/voxel. Over the years various distance transformation algorithms have been proposed both in 2-D and 3-D [145][146][147][148]. Among the different proposed distance metrics, cityblock distance (4-distance) and chess board distance (8-distance) are popular in two dimension and in

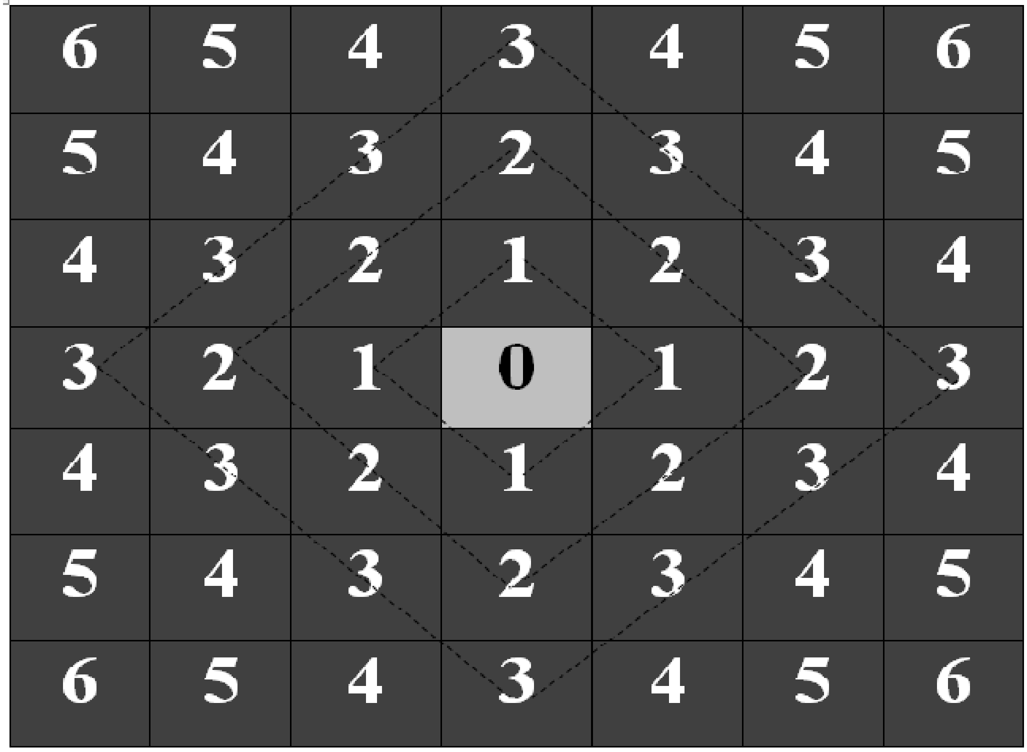

6	5	4	3	4	5	6
5	4	3	2	3	4	5
4	3	2	1	2	3	4
3	2	1	0	1	2	3
4	3	2	1	2	3	4
5	4	3	2	3	4	5
6	5	4	3	4	5	6

Figure 3.1 Propagation of city block distance from a center point

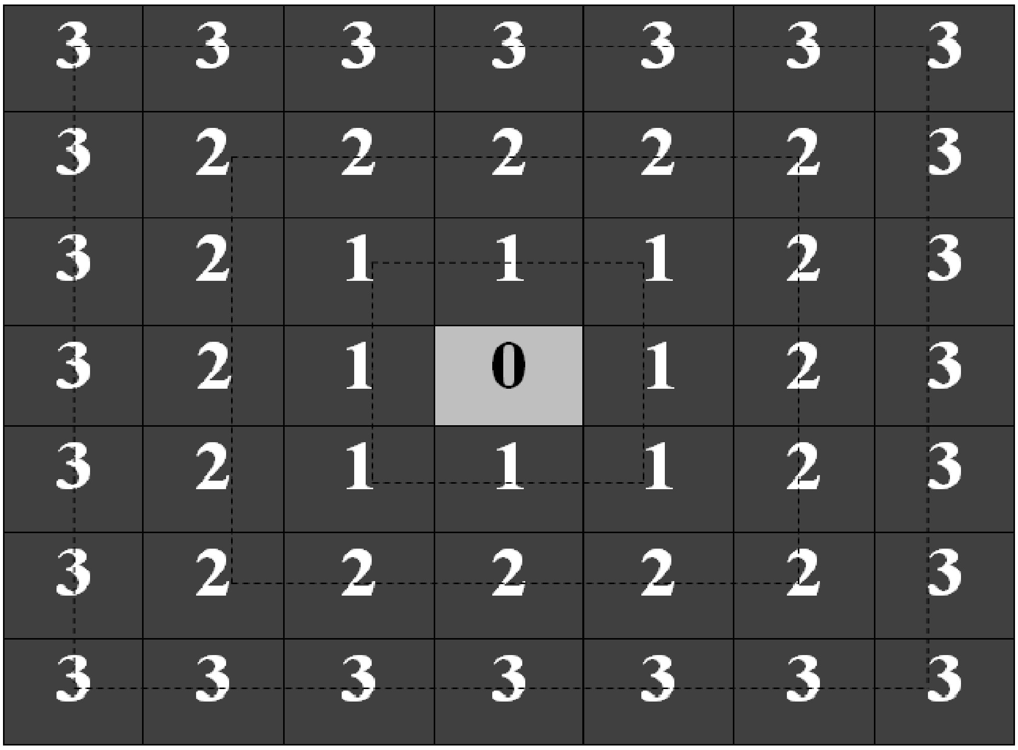

3	3	3	3	3	3	3
3	2	2	2	2	2	3
3	2	1	1	1	2	3
3	2	1	0	1	2	3
3	2	1	1	1	2	3
3	2	2	2	2	2	3
3	3	3	3	3	3	3

Figure 3.2 Propagation of chess board distance from a single center point

three dimension these are 6-, 18- and 26-distance. If $P=(x_1,x_2,x_3)$ is a point in a 3-D image, then DT value of that point will be,

$$\mathrm{DT}(P) = \begin{cases} DT(Q_i) + d_k, & DT(Q_i) + d_k < DT(P) \\ DT(P) & \end{cases}$$

where, Q_i is the neighbor of P, i=1,2,...,26, d_k=1,2,3 is the approximate Euclidean distance of P from three different kinds of neighbor voxels, i.e. 6-neighbors, 18-neighbors and 26-neighbors. In the present work, three approximate Euclidian distance values are 10, 14 and 17 for 6, 18 and 26-neighbors respectively. In case of binary images DT performs well enough. But in case of segmentation of arterial structure and reconstruction of the same, distinction between vessel and soft bones is very crucial which cannot be done in DT image. Therefore, application of FDT is suitable in the present work.

3.1.4 Fuzzy Distance Transform

The application of hard distance transform is not appropriate for fuzzy objects. Here instead, the term FDT is appropriate and is used in literature to represent DT for fuzzy objects. In several image processing applications, researchers usually deal with noises, down sampling etc. and FDT is the tool to deal with these inaccuracies in a well-defined manner. The theoretical and algorithmic foundation for FDT in both continuous and digital spaces are discussed briefly by P. K. Saha et al. in [149].

Overlapping intensities for arteries, veins, and soft bones in CT angiogram images makes it a fuzzy object. It is a challenging task to the researcher to extract a specific vasculature removing unintended elements. To apply the notion of fuzziness, the most important part is choosing the appropriate fuzzy membership function. The rules and techniques for constructing appropriate fuzzy membership function is briefly discussed in [150]. For the separation of iso-intensities, S. Basu et al. proposed a multi scale opening algorithm [134]. Lots of work has already been done for separation of conjoined fuzzy objects with shared intensities [124][151][100][152].

The theory of FDT is well established by Saha et al. in [149]. In this section, the formal notation related to the theory of FDT is introduced first. An object $\mathcal{O}$ is a fuzzy set $\{(p, \mu_{\mathcal{O}}(p)) | p \in \mathcal{Z}^3\}$, where $\mu_{\mathcal{O}}: \mathcal{Z}^3 \rightarrow [0,1]$ is the membership function. The support of an object $\mathcal{O}$, is the set of all voxels with non-zero membership value such that $\theta(\mathcal{O}) = \{p | p \in$

$\mathcal{Z}^3\ and\ \mu_{\mathcal{O}}(p) \neq 0\}$. $\bar{\theta}(\mathcal{O}) = \mathcal{Z}^3 - \theta(\mathcal{O})$ is the background. FDT accounts for both partial voxel occupancy and spatial heterogeneity of an object distribution. The length of a link $< p, q >$ is calculated as $\frac{1}{2}\left(\mu_{\mathcal{O}}(p) + \mu_{\mathcal{O}}(q)\right)||p - q||$, where $||.||$ denotes any Euclidean L2 norm. The length of a path $\pi =< p_0, p_1, \dots, p_l >$ in a fuzzy object $\mathcal{O}$, denoted by $\prod_{\mathcal{O}}(\pi)$ is sum of the length of all links along the path i.e.

$$\prod\nolimits_{\mathcal{O}} = \sum_0^{l-1} \frac{1}{2}\left(\mu_{\mathcal{O}}(p_i) + \mu_{\mathcal{O}}(p_{i+1})\right)||p - q||$$

The fuzzy distance between two voxel $p, q \in Z^3$ in an object $\mathcal{O}$, expressed as $\omega_{\mathcal{O}}(p, q)$ is the length of one of the shortest path from p to q, i.e.,

$$\omega_{\mathcal{O}}(p, q) = \min_{\pi \in \mathcal{P}(p,q)} \prod\nolimits_{\mathcal{O}}(\pi)$$

where, $\mathcal{P}(p, q)$ is the set of all paths from p to q. The FDT of an object $\mathcal{O}$ is an image $\{(p, \Omega_{\mathcal{O}}(p)) | p \in \mathcal{Z}^3\}$, where $\Omega_{\mathcal{O}}: \mathcal{Z}^3 \rightarrow \mathfrak{R}^+$ denotes the FDT value at a given point, $\mathfrak{R}^+$ is the set of all real numbers including zero, $\Omega_{\mathcal{O}}(p)$ is the fuzzy distance from the background or is defined as the fuzzy distance between p and its nearest points in $\mathcal{Z}^3 - \theta(\mathcal{O})$.

$$\Omega_{\mathcal{O}}(p) = \min_{q \in \overline{\theta(\mathcal{O})}} \omega_{\mathcal{O}}(p, q)$$

3.2 Literature Review

There are several applications of FDT, especially in image analysis domain. In the following literature review first some literatures on DT will be discussed, then FDT based segmentation. So the literature review is broadly classified as (i) Distance transform; (ii) FDT based segmentation.

(i) Distance Transform

The DT conception was introduced earlier in the mid 1960s by Rosenfeld and Pfaltz [153][154]. They considered the City block DT; the Chessboard DT, where steps in the 8-neighbourhood (edge and point neighbors) are allowed; and the Octagonal DT where the previous two DTs are mixed. These are all usually called “path-generated” DTs. The chessboard DT has several bad properties and should not be used.

Early works on DTs were presented in 2-D. As the Cityblock and Chessboard DTs are rotation dependent, according to the location of the object DTs’ values change. Therefore, weighted DTs were introduced, where edge-neighbor and point-neighbor steps get different lengths. Montanari [155] suggested weights 1 and √2, while Hilditch and Rutovitz [156] suggested 2 and 3, as integers are easier to handle. However, it was not until the 1980s that Borgefors computed optimal weights [146], which turned out to be 0.955 and 1.369, with 3 and 4 as the best integer approximation with a maximum distance difference between directions of about 8% (which is lower than for Montanari's more intuitive suggestion, where the maximum difference is 9%). If the neighborhood is extended to 5 × 5, the difference can be lowered to 2%, by using weights 5, 7, and 11 for edge, point and knight-neighbors, respectively [146]. Regularity issues for weighted DTs are discussed in [157].

G. Borgefors et al. [146] described DT of an image in a very unique way, it described DT as a method that assigns to each non feature point of the image the minimum distance from a feature point, as opposed to the usual notion of distance of a point from its nearest boundary point, thus extending the idea from binary to fuzzy image. It is an old approach that tries to approximate Euclidean distance transform in iterative fashion by considering a 7x7 neighborhood by integer approximation of the exact distance function. In the later part six different distance functions are described and their pros and cons are elaborated.

T. Saito et al. [158] proposed a way to find the Euclidean distance transformation and the Voronoi diagram based on the exact Euclidean metric for an n-dimensional picture (n-dimensional picture does not refers to the recent notions of 6-D pictures by MIT media labs, here n is at-max 3 in practice). It discussed about four algorithms that computes DT by serially connecting n-dimensional filters resulting in much faster solution.

O. Cuisenaire et al. [147] investigated a method that computes exact Euclidean DT by propagation, using bucket sorting. At first an approximate DT is calculated using coarse neighborhood and then it is gradually refined with increasing order of neighborhood but keeping it restricted under the tiles of the image obtained from Voronoi diagram, for keeping the computational costs low.

F. Y. Shih et al. [159] proposed a way to compute Euclidean distance transformation(EDT) saving more time than bucket sorting, in two scans using a 3×3 neighborhood. By recording the relative x- and y-coordinates, an optimal two-scan algorithm was discussed which can compute the EDT correctly and efficiently in a constant time without iterations.

H. Eggers et al. [143] proposed two new error-free sequential EDT for binary images in 2-D, sufficient 1 and sufficient ∞ propagation. Iterative propagation of contours via least Euclidean distance path is studied. The distance information of each point, is updated directly by a distance suggestion. This algorithm promises a better solution with respect to computation cost, than existing algorithms.

DT and their reverses are easy to extend to higher dimensions which can be found in several literatures[145][144].

H. Embrechts et al. [160] proposed one algorithm to find out the EDT by a divide and conquer approach based on a fast sequential algorithm for the Signed EDT (SEDT). The partial calculation of SEDT is tuned to act as the partial calculation of the Voronoi diagram. The algorithm has two local calculation steps whose computational complexity is proportional to the number of pixels of the sub regions and a global calculation step with complexity proportional to the image perimeter.

Rosenfeld recommended the use of an adjacency pair (κ1,κ0) where κ1 is used for object voxels and κ0 is used for background voxels [141]. Specifically, in a 3-D cubic grid, 26-adjacency is used for object voxels and 6-adjacency is used for background voxels, or vice versa. He convincingly demonstrated that use of such an adjacency pair leads to a workable framework of digital topology, which holds many important classical properties, including the Jordan curve property. Although the use of two different adjacency relations appears to be somewhat paradoxical, it is the form of digital topology that has become most popular.

(ii) FDT based Segmentation

S. Basu et al. [124] described a new algorithm to separate two structures which shared a common intensity. This algorithm also can work for structures which are conjoined at several unknown positions and scales. They used CTA of patients and applied their novel algorithm to segment the vasculature with intracranial aneurysms. To separate vessels from bone in the common intensity space becomes a real challenge. They combined FDT and a morphologic function to segment the bone and vessels. The accuracy has been tested on phantoms which is generated mathematically, vessel cast phantom of CT image of pig pulmonary and CT angiography images of cerebral vasculature of human.

P. K. Saha et al. [100] applied a novel multiscale topomorphologic approach for opening of two isointensity objects fused at different locations and scales is presented and thereby separated arterial and venous trees in 3-D pulmonary CT images. The method is intended to solve the following two fundamental challenges: how to find local size of morphological operators and how to trace continuity of locally separated regions. These challenges are met by combining FDT, a morphologic feature with a topologic fuzzy connectivity, and a new morphological reconstruction step to iteratively open finer and finer details starting at large scales and progressing toward smaller scales.

S. Basu et al. [134] separated conjoined fuzzy objects using their multi-scale opening (MSO) algorithm. They also developed a mathematical morphological operator and applied that to separate. They made physical cast phantom and segmented arteries and veins of a pig lung. They also evaluated their algorithm’s performance using mathematical phantoms and separated arteries and veins of complete carotid vascular structure using patient’s CTA data.

P. K. Saha et al. [161] established theoretical properties of a MSO algorithm for two conjoined fuzzy objects, and introduced its extension to separate two conjoined fuzzy objects with different intensity properties. In addition, its applications to artery/vein separation in pulmonary CT imaging and carotid vessel segmentation of patients’ CTA with intracranial aneurysms are presented. Results of application of the method in separating arteries and veins in a physical cast phantom of a pig lung are presented. Experimental results using this algorithm on patients' CTA data demonstrate a high average accuracy of 96.3% with 95.1% sensitivity and 97.5% specificity and a high reproducibility of 94.2% average agreement between segmentation results from two mutually independent users. Approximately, 25-35 user-specified seeds/separators are needed for each CTA data through a custom-designed graphical interface requiring an average of 30 min to complete carotid vascular segmentation in a patient's CTA dataset.

Z. Gao et al. [112] separated Artery/Vein **(**A/V) via *in vivo* imaging using multiscale topomorphologic opening (MSTMO) algorithm which they developed. The method starts with two sets of seeds, one for each of A/V trees and combines FDT and fuzzy connectivity in conjunction with several morphological operations leading to locally adaptive iterative multiscale opening of two mutually conjoined structures. The method has achieved 99% true A/V labeling in the cast phantom and, almost, 92-94% true labeling in human lung data. Reproducibility of the method has been evaluated using multiuser A/V separation in human CT data along with contrast-enhanced CT images of a pig's lung at different positive end-expiratory pressures (PEEPs). The method has achieved, almost, 92-98% agreements in multiuser A/V labeling with ICC for A/V measures being over 0.96-0.99.

3.3 Research Objective

From the above literature survey it is understood that FDT based segmentation is useful for segmentation of conjoined structure in shared intensity space. In this work, a novel approach is developed to segment the cerebrovasculature using FDT based geodesic paths. Detailed methodology is described in the following section.

3.4 Methodology

The whole image is represented as an undirected graph $G = (V, E)$, where V is the vertex set denoted by $\{\, P \mid P \text{ is a voxel in the 3-D image} \,\}$, E is the set of edges denoted by $E = \{(P_1, P_2) | P_1 \text{and } P_2 \text{ are adjacent} \}$.

The first step of the methodology is to find the centre point of the presumed artery between input seed points and then draw spheres in these points with radius equal to the FDT value of that point. A sphere $S(P, r)$ with centre $P = (x_c, y_c, z_c)$ and radius r is the locus of all points (x, y, z) in z^3 such that,

$$(x - x_c)^2 + (y - y_c)^2 + (z - z_c)^2 = r^2$$

Geodesic path [150] is defined as minimum cost shortest path between two points in two or three-dimensional space. Dijkstra’s shortest path algorithm has been used for geodesic path propagation with modification so that shortest path will always pass through the nearest local maxima point if it exists, otherwise it will pass through the maximum FDT value point in its neighbourhood. To force the geodesic path between two seed points to pass through nearest local maxima points or maximum FDT value point, edge weight between any point and corresponding nearest local maxima point or maximum FDT value point should be minimum. Here a cost function β is introduced that computes edge weights between a point $P = (x_1, x_2, x_3)$ and one of the locally deepest points $Q = (y_1, y_2, y_3) \in Z^3$ as follows:

$$\beta(P, Q) = \left(\frac{2}{(DT\,(P) + DT\,(Q))}\right) \times DIST\,(P, Q)$$

where, $\mathrm{DIST}\,(\mathrm{P},\mathrm{Q}) = \sqrt{(\mathrm{x}_1-\mathrm{y}_1)^2+(\mathrm{x}_2-\mathrm{y}_2)^2+(\mathrm{x}_3-\mathrm{y}_3)^2}$.

Dijkstra’s algorithm which is basically known as a greedy method, chooses a neighbor that is connected through the edge with minimum cost from current point for next iteration. In this current work the algorithm will always choose the nearest local maxima point or in other words, maximum FDT value point in the neighbourhood of the current point due to cost function β. After termination of this algorithm, it will provide connected centre points of the presumed artery. If sphere is drawn taking these points as centre and radius equal to the FDT values of the point, the desired segmentation will be done.

Manual interaction facilities of selecting and editing different seed points are supported within the developed graphical user interface (GUI). With the help of the GUI, pairs of seed points are taken as input and visualized the segmented results in axial, coronal, sagittal views. The 3-D rendition of the segmented part is shown with the help of popular ITK-SNAP software [117]. Here the work is focused on segmentation of arterial tree from original patient’s CTA images. In this segmentation algorithm first geodesic path is generated between two end points. The flow of the algorithm is shown in Figure 3.3. The algorithm is applied on two different types of data: 1) mathematically generated approximate phantoms and 2) segmented arterial trees from patient’s CTA images. Figure 3.4, Figure 3.5 and Figure 3.6 expose how the proposed algorithm actually works with mathematically generated approximate arterial phantom to find the geodesic path. Figure 3.4 shows that the proposed algorithm generates discrete set of geodesic points on binary phantom data. Figure 3.5 shows some of the intermediate steps of geodesic points generation through six images (Figure 3.5a–f). Total 18 initial seed points are taken to generate the set of geodesic points. The accuracy of the generated geodesic points is checked by adding the set of secrete points as an overlay image with original image with the help of ITK-SNAP s/w in Figure 3.4. Now, the results on original patients’ CTA images are shown in Figures 3.7, Figure 3.8 and Figure 3.9. Figure 3.7 shows the six phases of segmentation results on one patient’s data. The intermediate steps of gradual segmentation of the arterial tree from its surroundings are shown by the images in Figure

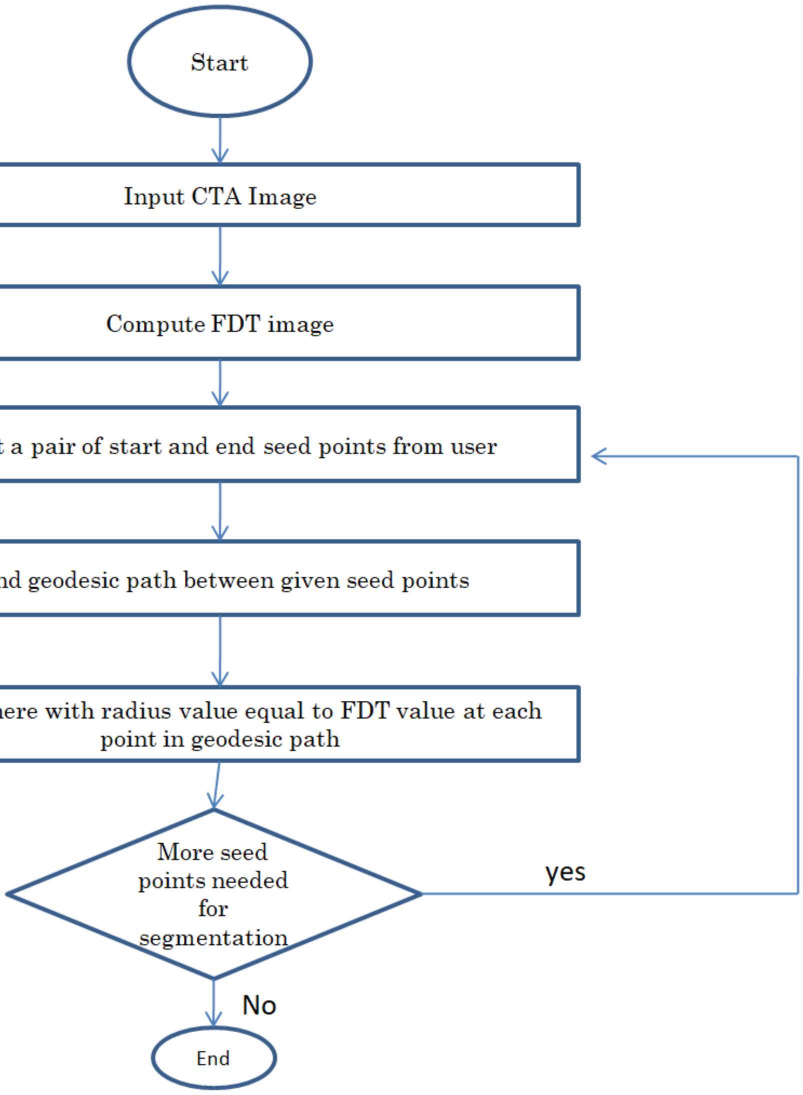

Figure 3.3 Flow chart representation of the proposed algorithm

3.7a–f. A total of 14 seed point is used for segmentation. Initial seed points are taken in two different fashions: (1) start and end points and (2) joining points. The long segments generated by the first way, start and end points are taken initially and the intermediate points are generated by the algorithm. To generate the in-between small segments, the second way is chosen. If a point is chosen as a joining point, the proposed algorithm generates a set of geodesic points such that a path is created by joining these points.

3.5 Segmentation Results

Segmentation results are shown on eight patients' CTA image in Figure 3.8. Blue colored portion in Figure 3.8f shows the presence of aneurysm in the cerebrovasculature. The accuracy of all the segmented data are verified by overlaying the phantoms with the original images. Figure 3.6 shows the overlay of one patient's CTA image with the original image in axial, coronal and sagittal views and 3-D rendition with the help of ITK-SNAP s/w. Proposed algorithm for segmentation of cerebrovasculature is compared with the MSO algorithm proposed by P. Saha et al. in [151].

Table 3.1 Comparative analysis of number of seeds required for segmentation of arterial tree from the other components in MSO algorithm and the proposed algorithm

Image ID	**Number of vessel seeds used in MSO Saha et al. [151]**	**Total no. of seeds (vessel + bone + seperator) used in MSO Saha et al. [151]**	**Total number seeds in present algorithm**
1016	14	33	12
2005	28	50	13
3029	13	41	14
2001	14	45	12
3032	9	46	13
3036	8	35	14
2008	16	34	14
2009	15	30	10

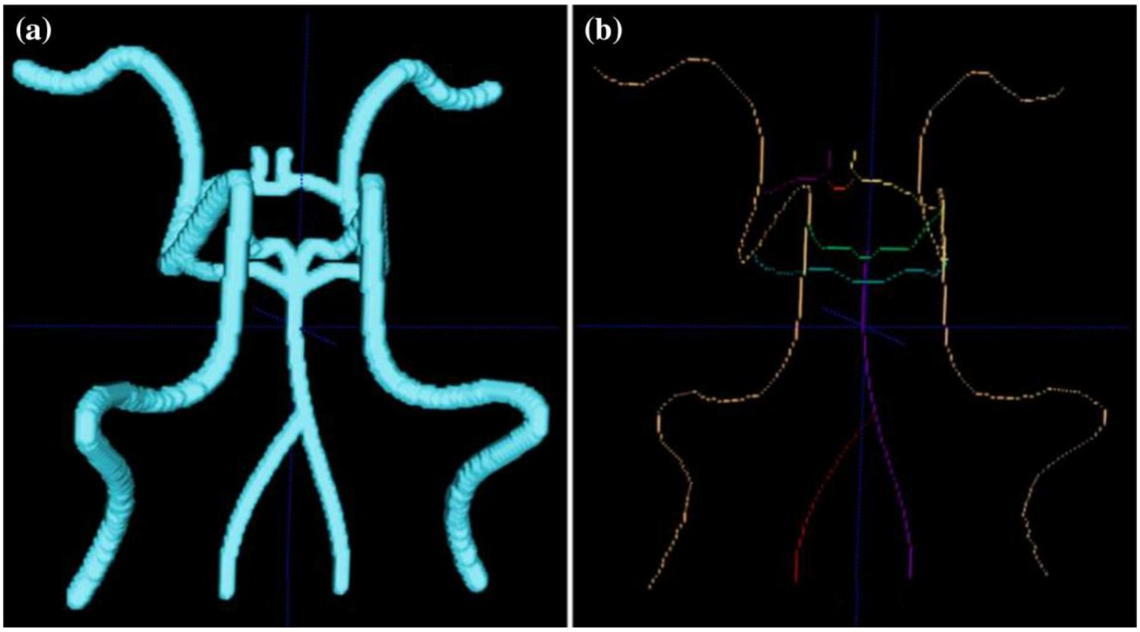

Figure.3.4 A Mathematically generated binary phantom. (b) Discrete set of geodesic points after applying the proposed algorithm on (a)

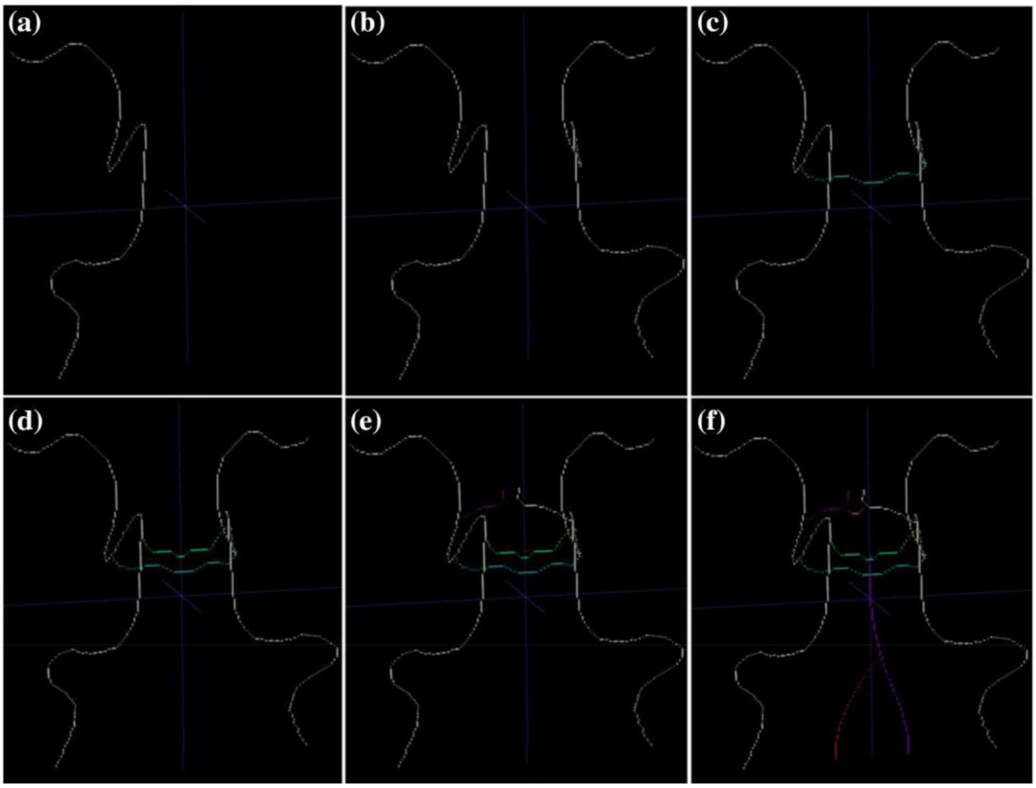

Figure 3.5 a–f Intermediate steps of generation discrete set of geodesic points for the mathematical phantom image shown in Fig.3.4a

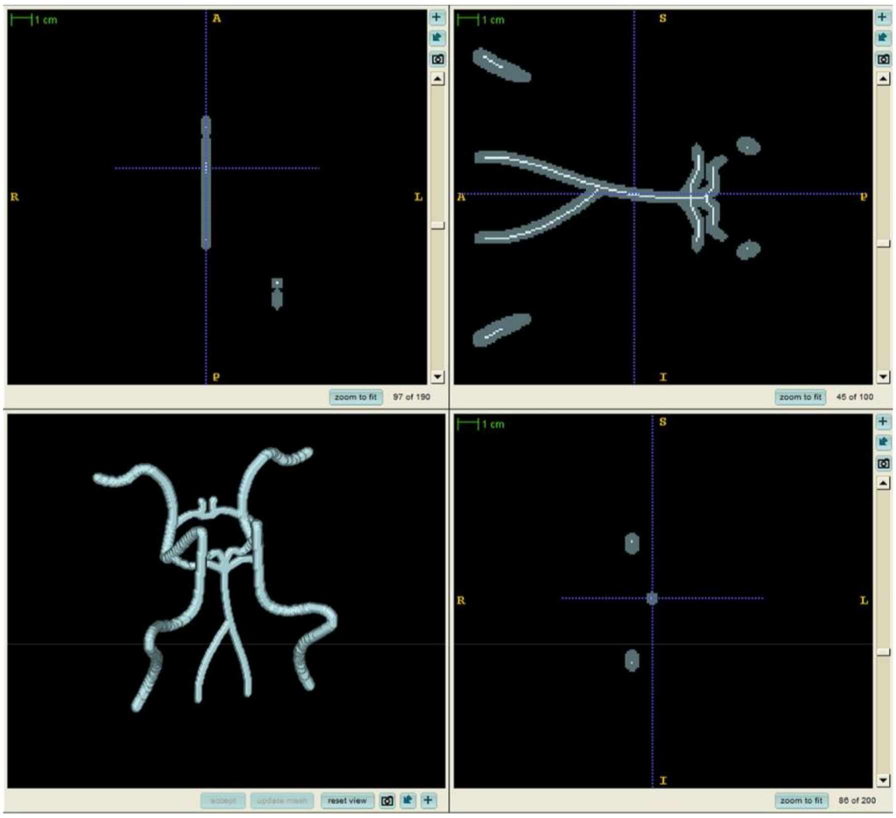

Figure 3.6 Overlay of the set of discrete geodesic points with the original binary phantom data

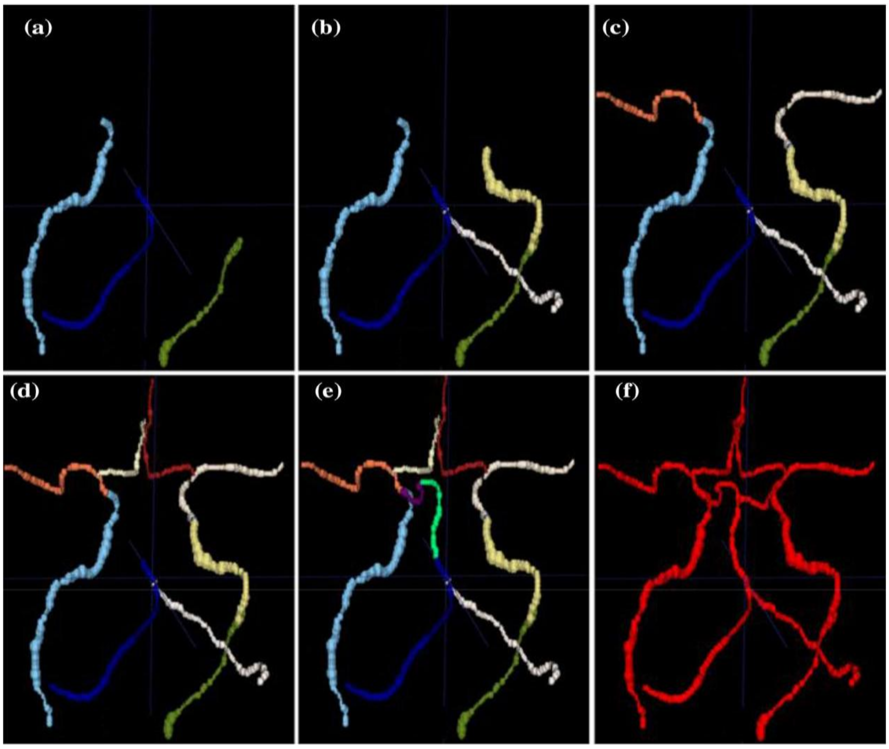

Figure 3.7 Six phases of segmentation of vasculature from a CTA image (Data id-3036)

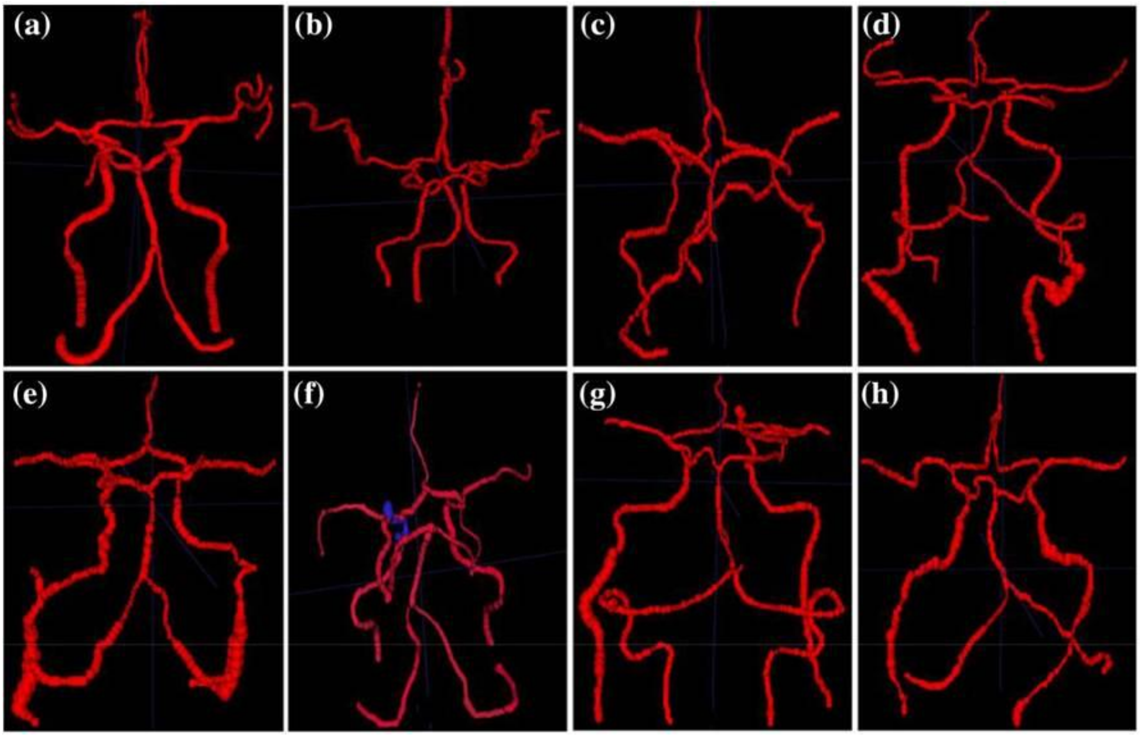

Figure 3.8 a–h Segmentation of circle of Willis part from 8 different CTA images. Image id—a 2005, b 1016, c 2001, d 2008, e 2009, f 3029,*blue coloured* portion is aneurysm g 3032, h 3036

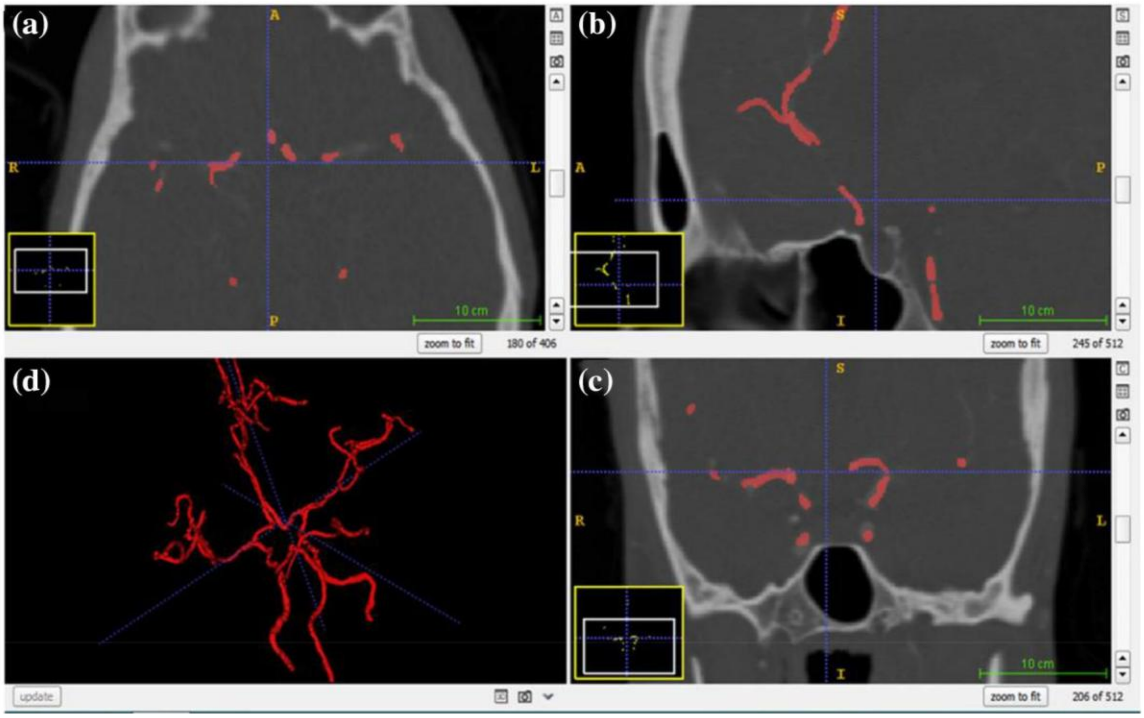

Figure 3.9 A segmented vasculature is shown of the original CTA image with the help of ITK-SNAP s/w

From Table 3.1, it can be easily seen that the number of vessel seeds required for reconstructing arterial tree for all the patient’s images are lesser than the original MSO algorithm [161]. In addition to the less number of seed points, the advantage of the proposed algorithm is that at the beginning users have to select only vessel seed points for segmenting arterial tree from the other components. On the contrary, in MSO algorithm the users have to select three different types of seed points, e.g. vessel seeds, separator seeds and the bone seeds.

3.6 Discussion

The present work is focused on proper segmentation of vasculature from soft bones in the overlapping intensity area. It also targeted towards reducing the number of user interaction in the segmentation process. This work has adopted FDT-based geodesic path propagation approach, and it successfully outperformed the pervious approaches made by P. K. Saha et al. [151] and other research groups. Geodesic points and FDT are used to find the radius of the arterial tube. This method is semiautomatic, and the user can modify the generated digital phantom structures to make it more accurate. The present algorithm is both efficient and precise. Digital phantoms generated through this algorithm can be helpful in studying the arterial bends, bifurcated regions, joins and possible modeling of digital fluid flows in human cerebrovasculature. ITK-SNAP [117], open-source software, has been used to overlay generated phantom structures over original CTA images. This segmented human cerebrovascular structure has been used for hemodynamic analysis which is discussed in subsequent chapters. Digital phantoms are also of use in a range of other bio-imaging applications, and similar synthetic structures may be generated for analysis of structural/plastic changes in hippocampal dendritic spines [162].

Chapter 4

Digital flows: Theory and Application

Vascular disease is the outcome of disrupted blood supply to particular parts of the body. The present study focuses on specifically cerebrovascular diseases which are the consequences of insufficient blood flow or no blood to some area of the brain. The areas which are deprived of adequate blood supply actually deprived of nutrients and oxygen, the essential element to function properly. This interrupted blood supply can lead to Stroke, Transient ischemic attack etc [163][164]. The arteries which supply blood full of oxygen to the different parts of the brain may be blocked with cholesterol deposition which can gradually break and cause blood clots [82]. If the vessels of the brain are smaller in size, the cholesterol deposition and the blood clots can become trapped in that, decreasing blood supply to the area. This can lead to life-threatening disease like stroke and heart attack due to blockage in the artery.

Work on the flow analysis within the blood vessels is going on since the middle of the last century but nowadays due to (i) growing computational power, (ii) advancement in imaging equipment and technology, (iii) reconstruction of geometry techniques as well as (iv) the availability of efficient numerical algorithms, the use of computational techniques in fluid dynamics for the study of physiological blood flows is becoming an active area of research. Actually this progress happens to be possible because of the awareness that numerical models can describe blood flow quantitatively in vital vascular sites and to express the relationships between vessels shape, hemodynamics, and a family of clinical indicators like WSS, vorticity etc. those correlates with the risk of failure due to artery occlusion for stenosis or aneurysm rupture [165]. It is accepted that once a mild stenosis is found to be built in the artery, biomechanical parameters changes and that changes from the blood flow along with stress distribution in the arterial wall may lead to further progression of the disease. Usually blood flow is laminar, but if due to some reason artery diameter become narrowed and for that velocities increase then obviously it leads to make the nature of flow pulsatile. This periodic unsteadiness of flow nature makes the transition from laminar to turbulence. A comprehensive study and understanding of local hemodynamic surroundings, wall modifications influence on flow patterns, adaptations of the vascular wall can have useful clinical applications [166].

Flow simulation techniques, medical imaging data acquisition which is non-invasive such as CT scan, MRI make possible to construct 3-D models of vasculature. Measurement technologies like Doppler ultrasound have enhanced to furnish correct information of the flow characteristics.

There are many existing methods to calculate the flow through the generated phantoms. But they are costly, time consuming and need experts to handle.

4.1 Literature Review

These literatures are mainly confined into two categories; (1) flow related, (2) computational model related.

(i) Flow Related

H. Bode et al. studied the velocity of the flow in the basal cerebral arteries in detail. Transcranial Doppler-Sonography has been used for this. This study has been undertaken on children of different age group. This study resulted with the conclusion that cerebral blood flow increases with the increasing velocities of flow. There is a decrement in cerebrovascular resistance during infancy. For all age group intracranial flow velocities are assessed. The assessing method is non invasive.

A. F. van Raamt et al. [168] did a retrospective study to know the actual characteristics which are correlated with the whole arterial blood flow to the brain. This study has been done in the patients with symptomatic vascular disease. The experimentation was done with data collected from 636 subjects (536 men,100 women, mean age58 years) with symptomatic vascular disease. The total volume flow rate (tVFR) was measured. The result showed that in comparison to general population tVFR increased in patients who has symptomatic vascular disease. This study also showed that the tVFR is lower in patients with diabetes than those without diabetes. Age is also one of the factor which decreases tVFR.

N. Shahcheraghi et al. [169] studied about how to understand the time-dependent flow. For this study reconstruction of human aorta has been done. In this paper, the numerical simulations have been done on realistic geometry as well as flow pulse. However, wall motion is not considered. The analysis on flow, pressure, stress can be used in future for different studies to find some vital biological significance. Many diseases which can be seen in large aorta, with different states, can be studied with changes in different parameter like flow pulse shape and Reynolds number.

(ii) Computational Models Related

J. Brunette et al. [170] validated computational models of coronary arteries which is atherosclerotic in nature. Heart attack is resulted from an atherosclerotic plaque rupture. This rupture occurs in response to both stress (mechanical) and inflammatory processes. A novel method to validate the computational model was built for coronary artery with atherosclerosis.

Different studies on velocity variance of blood flow in the arteries are done in [171][172][173]. It demonstrates that the flow reducing stenoses be precisely detected by this procedure. It must be emphasized, however, that data are not yet available to show that ulceration can be sensed by this approach. Several plaques that are not large enough to decrease distal pressure and flow but which may be the site of initial ulceration can also be identified. A small proportion of stenoses may undergo more rapid progression to severe stenoses and occlusion. Uceration, hemorrhage, and thrombosis, are the influences involved in this rapid progression may be giving growth to complex unstable plaque. Depending on human age, blood velocity inside the arteries is fluctuating. Plaque is developed due to irregular flow velocity.

A. K. Gupta et al. [174] and W. J. Vankan et al. [175] applied hierarchical quantification technique. In the first paper they implemented a model for carotid arterial blood flow using finite element method. Navier–Stokes theorem is used for blood flow simulation and arterial wall is depicted with elastic compliant model. From this literature, general pattern of flow can be reproduced. The investigation results are agreeing with the finding, got experimentally, which can be found in literature.

J. Chen et al. [175], J. Lu et al. [176], Z. Lou et al. [177] presented that local hemodynamic behaviors are dependent on the rheological properties of blood, the geometry of the bifurcation, and the properties of the arterial wall. The non-Newtonian fluid has a property of a flattened axial velocity profile due to its shear thinning behavior and has lower velocity gradients at the divider wall and positive velocity gradients at the non- divider wall as the difference between the velocity distributions for the Newtonian and non- Newtonian fluid is evident.

S. W. Lee et al. [178], D. Doorly et al. [179], F. M. A Box et al. [180], C. K Zarins et al. [181] discussed on arterial bifurcations geometry and nature of blood flow inside that. The hemodynamics of models differ from subject to subject which is derived from *in vivo* imaging. This study shows that geometry plays the main role to define the nature of the WSS patterns. Arterial disease, in the form of atheromatous plaques, is occurred at the bending portion of artery and also in the vicinity of branches. The physical basis of dimensionless similarity parameters was discussed and their use in characterizing flow regimes emphasized.

The primary task in CFD simulations is modeling of arterial geometry from medical images. Reconstruction of phantom can be done from MRI or CTA images. In both physical and digital phantom of arteries blood flow analysis is done by different methods. Various parameters affect this flow in phantom. A general idea regarding the flow methods is specified in the next section.

Z. Lou et al. [177] did a study on non-Newtonian behavior of blood flow on the hemodynamics at the aortic bifurcation that partially cause atherogenesis. A 2-D numerical model was proposed. A weak form of Casson equation was used for describing the blood rheology. It shows that non-Newtonian property of blood did not make radical changes in flow patterns. It increases the shear stresses and a higher resistance to flow separation.

G. Jungquist et al. [172] took a population-based sample of 478 men aged 69 years living in Malmo, Sweden. A Doppler ultrasonic examination of their carotid arteries was done and cerebrovascular symptoms & signs were taken of the same population separately. Among 471, a significant abnormalities in carotid blood flow velocity (moderate stenoses [30 − 60% diameter reduction] in 20%, severe stenosis [> 60%] reduction or occlusion in 5%) was found in 117(25%) men. During the year before examination in 9(2%), stroke was reported in $28\,\text{men}(6\%)$. There was a relation between ipsilateral hemispheric stroke/TIA and severe carotid disease $p < 0.001$. Four of seven men with total occlusion had a stroke or a clinically confirmed TIA.

4.2 Research Objective

In spite of above works, digital modeling of the flow patterns is not available in the literature. To easily find out the basic curvature, complexity of the curve and to have some information regarding flow, like the direction of the flow, a 3-D hypothetical flow model is proposed in this present chapter, which is allowed to pass through the generated datasets of carotid arteries.

4.3 Theory of Digital Flow

In this present work, a 3-D hypothetical angular fluid flow model is developed using FDT in 2-D digital space which is referred to as 2-D digital flow. Hypothetical fluid flow theory is first established in 2-D space and then in 3-D space. The above mentioned structure can be considered as a 3-D bounded region, well separated from the background. When the 3-D digital flow is allowed to pass through these structures in a

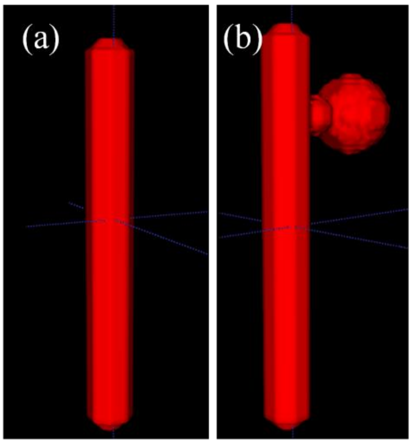

Figure 4.1 (a) 3-D rendering of a simple tubular structure (b) 3-D rendering of a simple tubular structure with aneurysm-like outpouch

particular direction, the hypothetical fluid flows towards that direction with some divergence angle. Flow starts from a single point and it wets those points which come into its way. But the fluid cannot wet those points of the vessel which are not in the direction of the flow. As the curve bends its angle changes and the flow divergence angle does not match the bending angle of the curve. As a result, the flow in the previous direction stops and a new flow start from those bending points to the direction of the curvature. Flow stops when it reaches the one or more extreme ends of the curve.

4.3.1 Digital Flow in 2-D

An image may be considered as a two dimensional (2-D) grid represented by Z^2 | Z is the set of integers. A grid point is referred to as a pixel, is an element of Z^2 and is represented by a pair of integer coordinates. Standard 8-adjacency is used here and two adjacent pixels are referred to as neighbors of each other. The set of 8-neighbors of a pixel p excluding itself is denoted by $N^*(p)$.

Let S denotes a set of pixels, a flow ω in S from $P \in S$ is defined by a set of parameters $\{P, \alpha, \beta\}$, where α is the direction of the flow from p, β is the flow angle. The image surface on which the flow takes place is considered as object of interest and the boundary points are the obstacles which block the flow. A digital flow ω from $p \in S$ to $q \in S$ is bounded by a set of wetted points W, such that $p, q \in W, W \in S$ and q is in $N^*(p)$. Figure 4.2 below shows the flow from P to its neighbors $\{q_1, q_2, q_3\}$, with flow angle $\beta = 45^0$ in $N^*(p)$ for two successive iterations.

Let us consider a flow from P having the direction of flow α and let the set of wet points in $N^*(P)$ be $\{q_1, q_2, q_3\}$, then the flow angle β is defined as the $max_{1 \leq i \leq 3} |P \angle q_i|$, such that $|\angle|$ represents the absolute angle of the digital straight line $\overline{\mathrm{P, q_i}}$ with the flow direction α. Figure 4.3 (a)-(d) above describes 2-D digital flow in 4 different directions in brief.

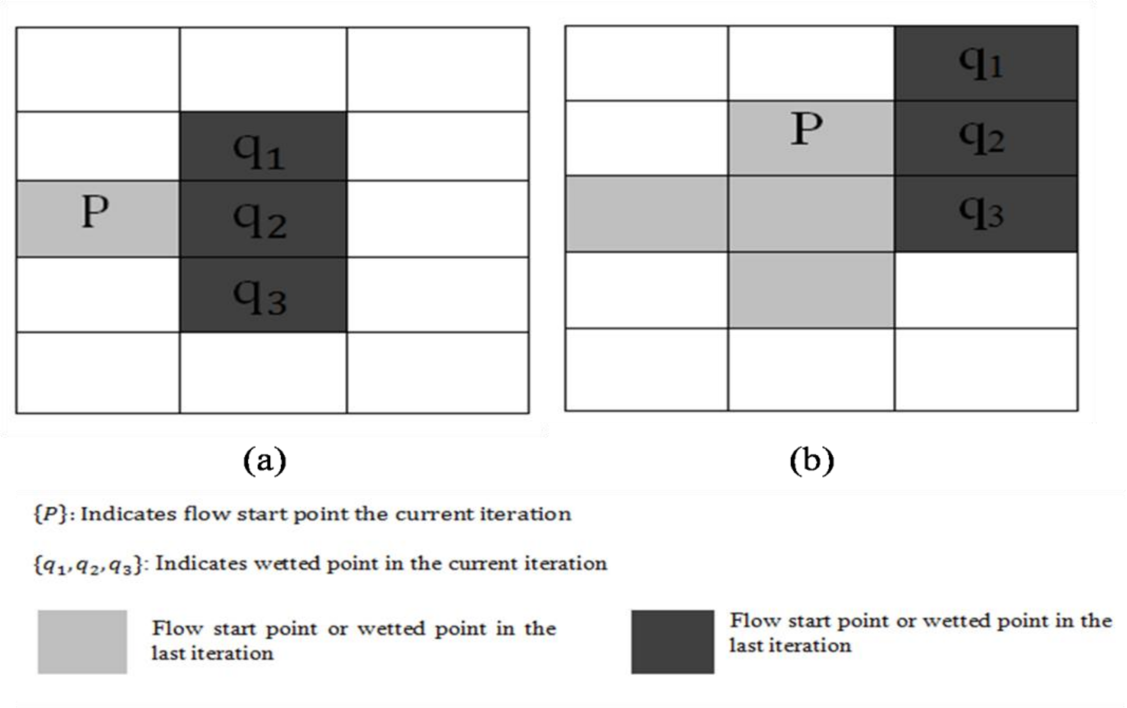

Figure 4.2 Iterative flow from point P to its neighbors$\{q_1, q_2, q_3\}$ (a) 1st iteration (b) 2nd iteration

4.3.2 Digital Flow in 3-D

A three dimensional (3-D) cubic grid, is represented by z^3 $|z$ is the set of integers. A grid point is referred to as a voxel, is an element of z^3 and is represented by a triplet of integer coordinates. Standard 26-adjacency is used here, i.e., two points $p = (x_1, x_2, x_3)$, $q = (y_1, y_2, y_3) \in z^3$ are adjacent if and only if $max_{1 \leq i \leq 3}|x_i - y_i| \leq 1$, where $|.|$ returns the absolute value. Two adjacent voxels are referred to as neighbors of each other; the set of 26-neighbors of a voxel p excluding itself is denoted by $N^*(p)$.

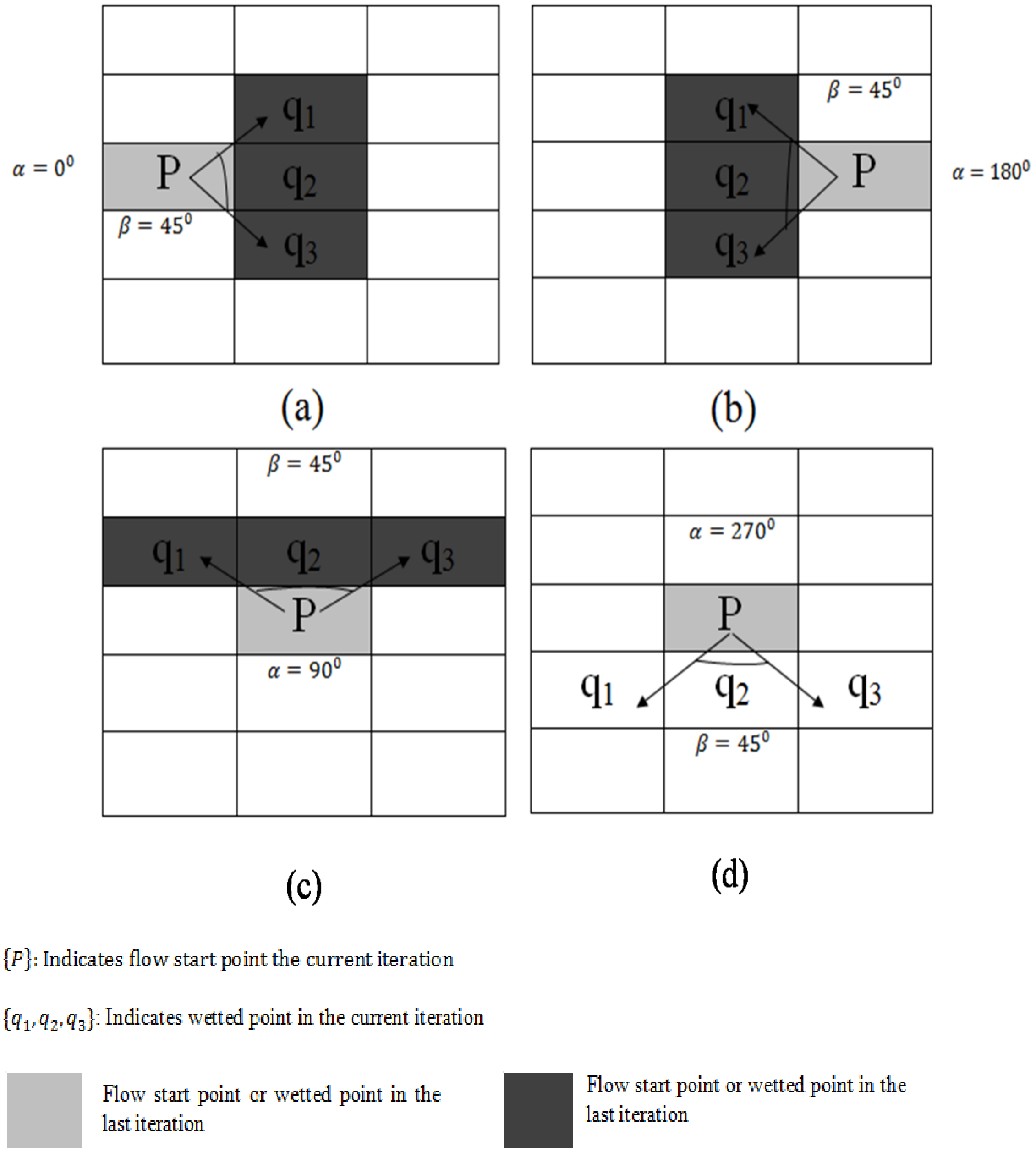

Figure 4.3 Schematic diagram of flow with different flow direction α and flow angle $\beta = 45^0$

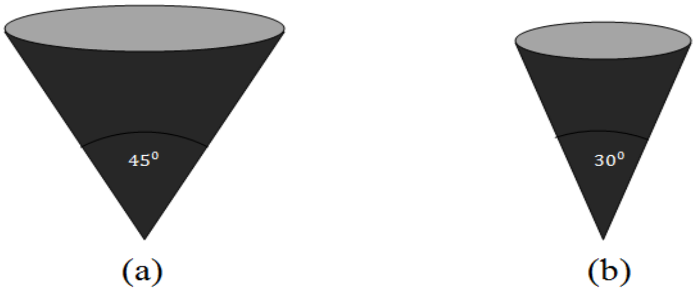

Figure 4.4 (a) Generation of solid angle for flow divergence angle 45^0 (b) Generation of solid angle for flow divergence angle 30^0

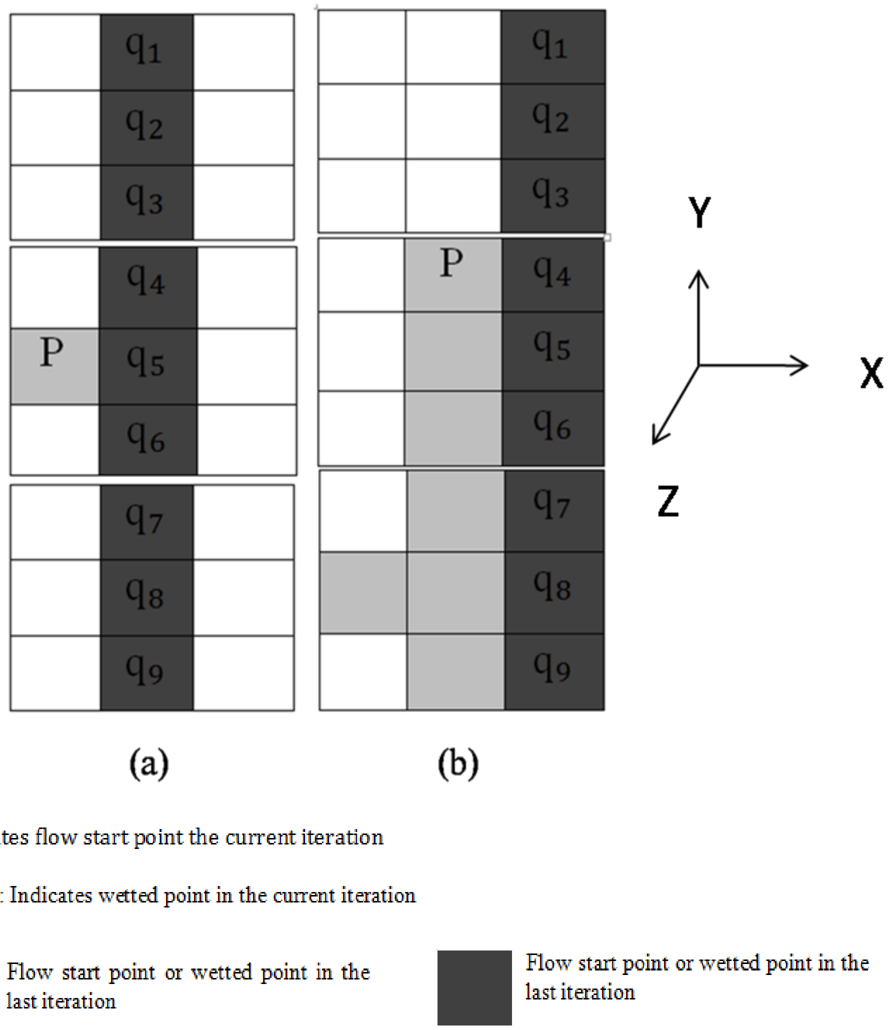

Figure 4.5 Iterative flow from point p to its neighbors; (a) 1st iteration (b) 2nd iteration.

Let S denotes a set of voxels, a flow ω in S from $p \in S$ is defined by a set of parameters $\{P, \alpha, \beta\}$, where α is the direction of the flow from p, β is the flow angle. When flow is projected from a particular voxel with a definite divergence angle, it forms hypothetical conical structure. The voxels inside the conic structure are the wet voxels. Shape of the conic structural changes with the change of flow divergence angle because number and position of wet voxels change. Figure 4.4 illustrates the idea.

Let us consider a flow from P having the direction of flow α and let the set of wet points in $N^*(P)$ be $\{q_1, q_2, q_3, \dots \dots, q_{n-1}, q_n\}$, $1 \le n \le m, m \in N$ then the flow angle β is defined as the $max_{1 \le i \le n} |p\angle q_i|$, such that $|\angle|$ represents the absolute angle of the digital straight line $\overline{p, q_i}$ with the flow direction α. Boundary voxels are considered as blocking region of the flow. Flow is projected along major six directions i.e. +ve and –ve directions of each of the three axis. Flow along six axes directions for only one iteration with flow angle $\beta = 45^0$ is well described by the Figure 4.6, Figure 4.7, Figure 4.8, Figure 4.9, Figure 4.10, Figure 4.11.

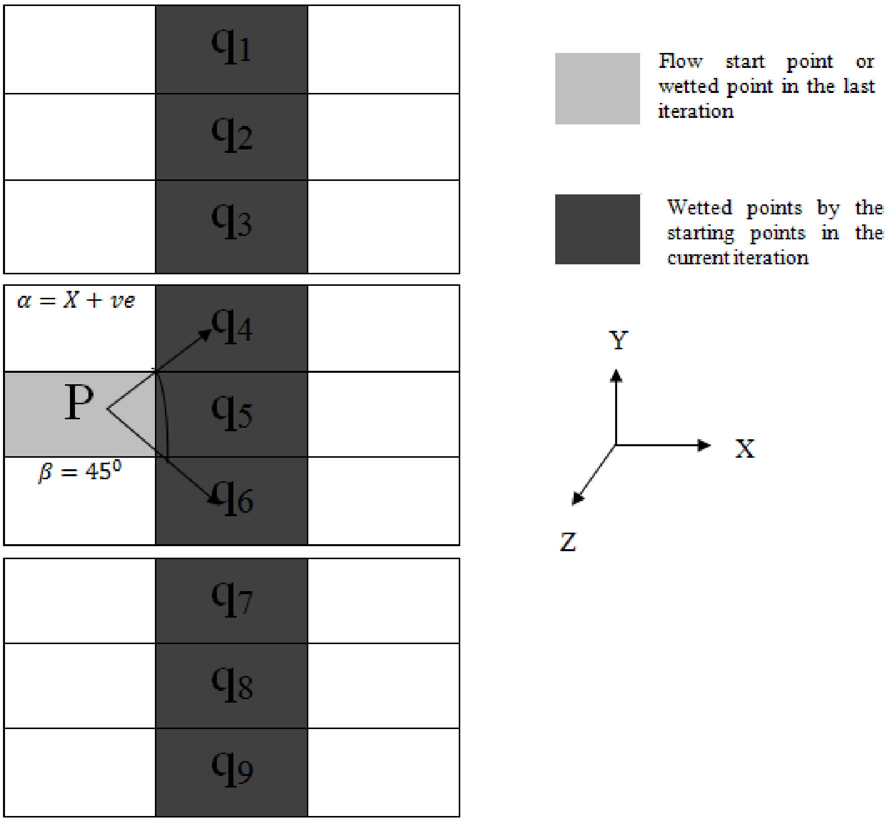

$\{P\}$: Flow start point in the current iteration $\{q_1, \dots, q_9\}$: Wetted points in the current iteration

Figure 4.6 Result of flow(one iteration) on a 3D plane, $\beta = 45^0$; $\alpha = +ve\ X$.

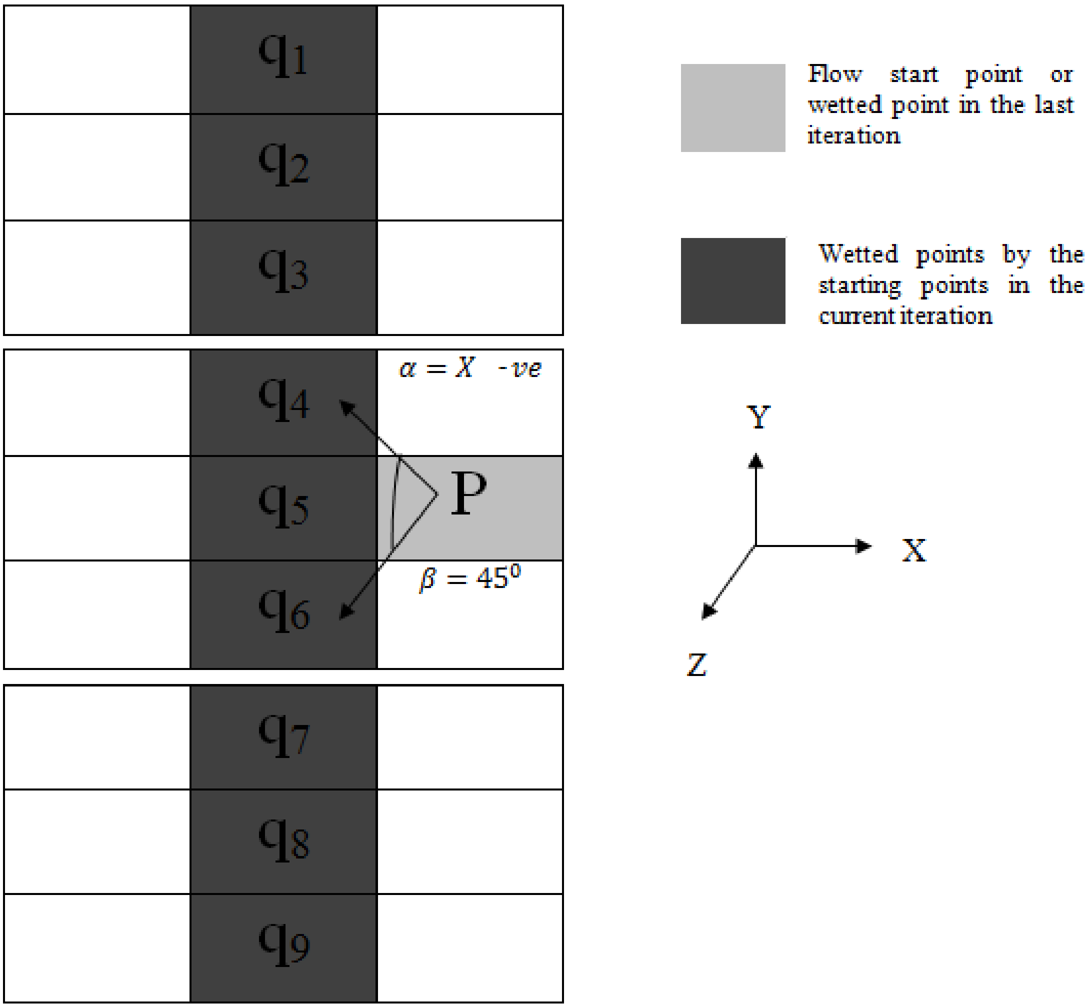

$\{P\}$: Flow start point in the current iteration $\{q_1, \dots, q_9\}$: Wetted points in the current iteration

Figure 4.7 Result of flow after one iteration on a 3D plane, $\beta = 45^0$; $\alpha = -ve\ X$.

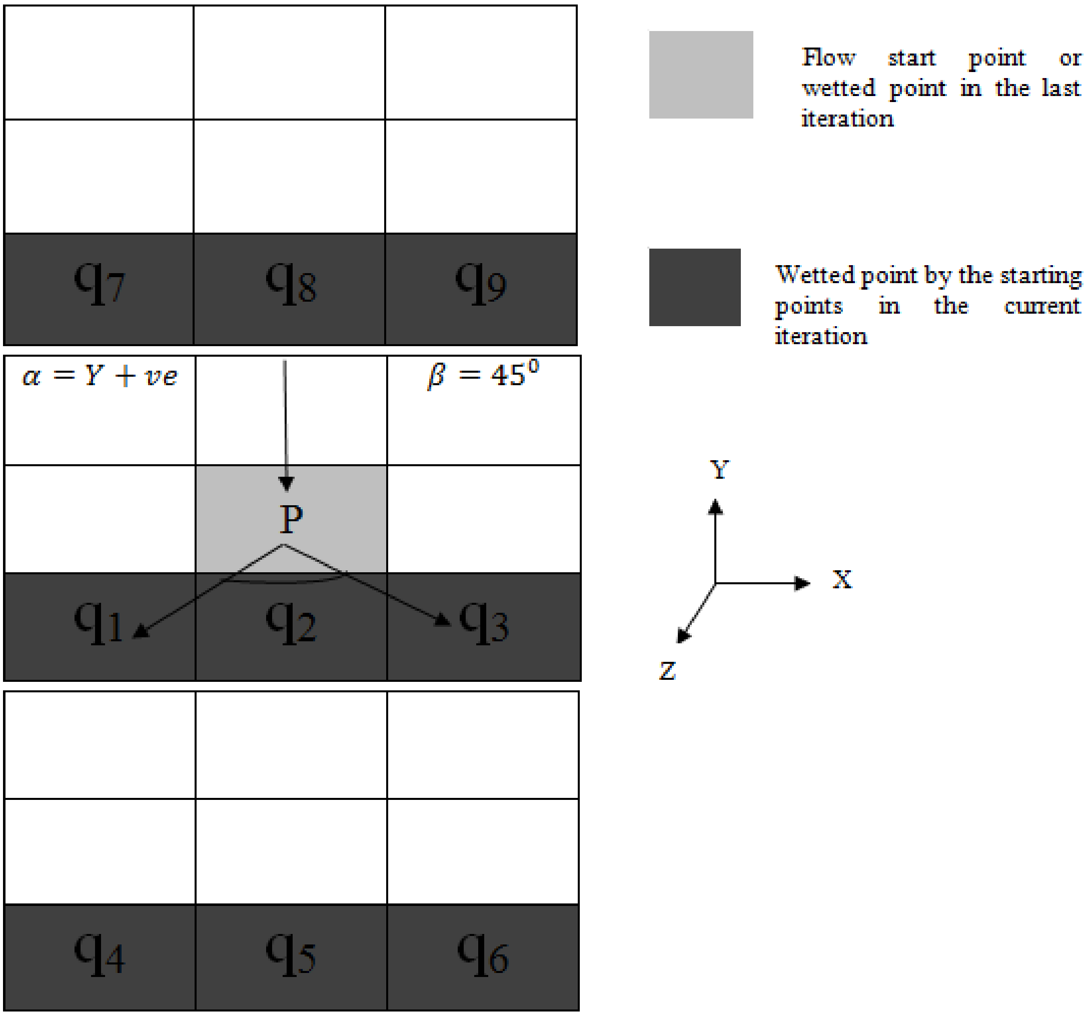

$\{P\}$: Flow start point in the current iteration $\{q_1, \dots, q_9\}$: Wetted points in the current iteration

Figure 4.8 Result of flow after one iteration on a 3D plane, $\beta = 45^0$; $\alpha = +ve\ Y$

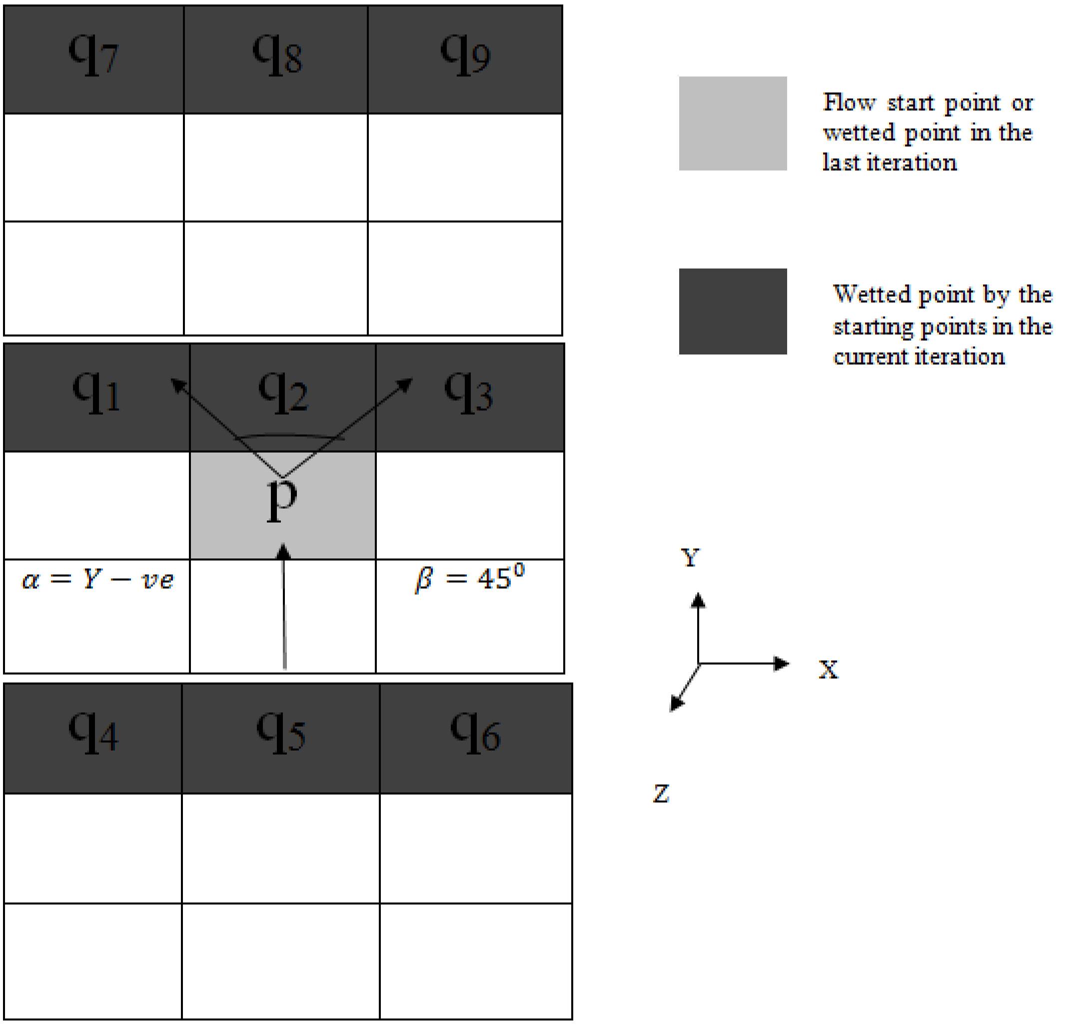

$\{P\}$: Flow start point in the current iteration $\{q_1, \dots, q_9\}$: Wetted points in the current iteration

Figure 4.9 Result of flow after one iteration on a 3D plane, $\beta = 45^0$; $\alpha = -ve\ Y$

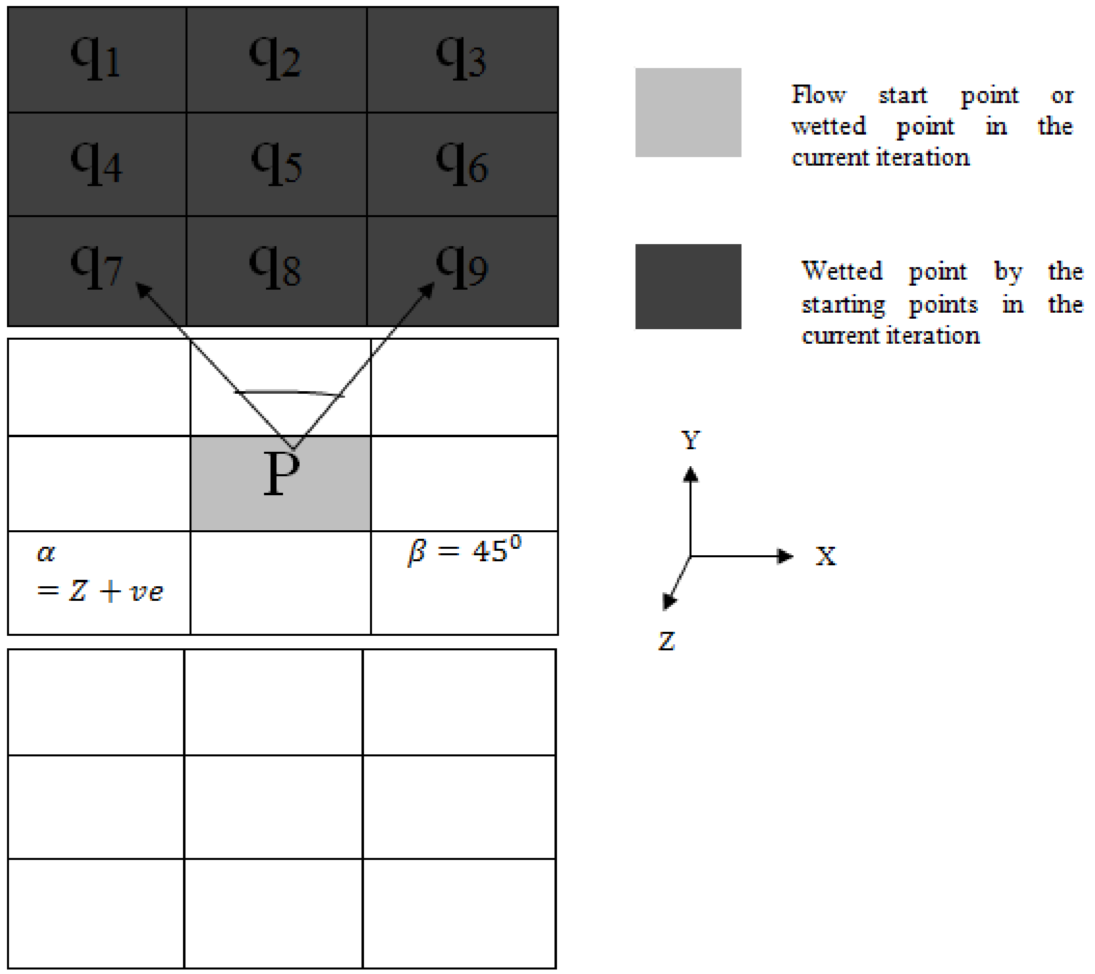

$\{P\}$: Flow start point in the current iteration $\{q_1, \dots, q_9\}$: Wetted points in the current iteration

Figure 4.10 Result of flow after one iteration on a 3D plane, $\beta = 45^0$; $\alpha = +ve\ Z$

Now the flow ω is iteratively propagated from each wet point $q \in W$ as $\{q, \alpha, \beta\}$. There is no obstruction along the path of the flow except the boundary wall which blocks the flow. In this current scenario flow is started from one voxel and initially it wets nine points along the flow direction with a definite flow divergence angle in the first iteration. Each such wetted voxels act as a potential flow start point in the next iterations and the flow is regenerated again. The flow is continued in this way until a termination condition is reached i.e. when a wetted neighbor does not have any neighbor to wet in the next iteration.

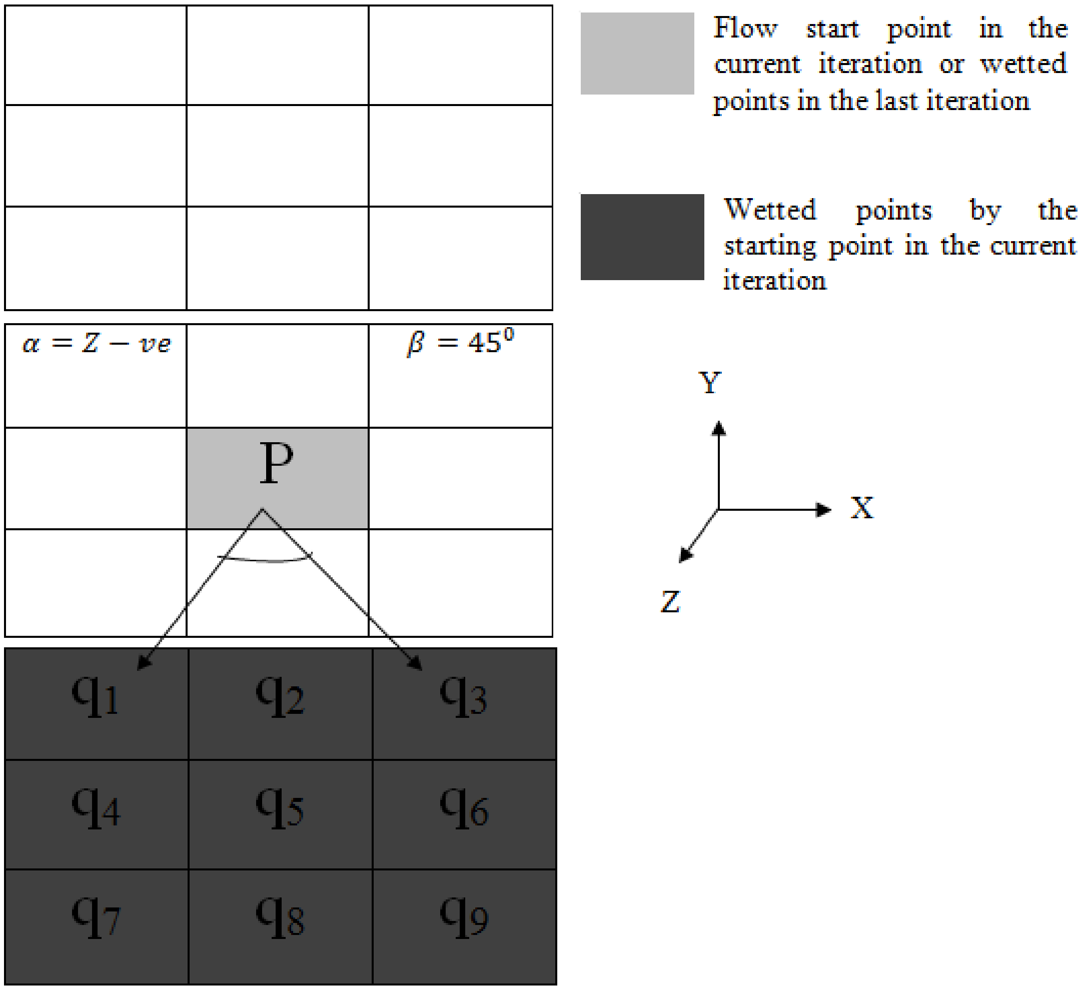

$\{P\}$: Flow start point in the current iteration $\{q_1, \ldots, q_9\}$: Wetted points in the current iteration

Figure 4.11 Result of flow after one iteration on a 3D plane, $\beta = 45^0$; $\alpha = -ve\ Z$

4.4 Experimental Results

In the current work 3-D digital flow is applied on different digital structures specifically, three different datasets are prepared for qualitative evaluation of the developed 3-D Digital Flow model

- Simple geometrical structures like Tube-shape, Y-shape, T-shape etc.
- Synthetic phantoms of human cerebrovasculature like small ACA-segment, ICA-segment, major arterial segment with circle-of-willis.
- Generated cerebrovascular tree from human CTA.

Over the years, many algorithms have been developed to extract vasculature from human CTA or MRI images [38][182]. In last two chapters, the reconstruction process of human cerebrovasculature from human CTA is discussed.

All of the above mentioned datasets is again divided into two types: one with embedded saccular aneurysm like bulb irregularities and another without any irregularities. Figure 4.1(a) and Figure 4.1(b) shows 3-D rendering of a simple tubular structure without aneurysm and with aneurysm respectively. As a visualization software ITK-SNAP-3.0.0 [117] is used.

4.4.1 3-D Digital Flow in Simple Geometrical Structures

Flow nature in some geometrical structure are shown below. To denote six possible directions of flow, six different color codes are used here. Figure 4.12 shows different color codes for six different directions.

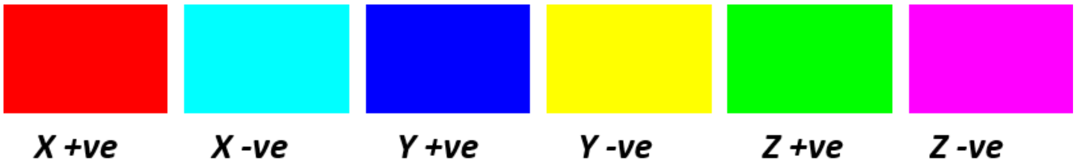

Figure 4.12 Color code for six different directions

Figure 4.13 shows the flow nature in simple tubular structures with and without aneurysm. Figure 4.13(a) shows structure without aneurysm before flow. The same directional color code will be used throughout this work. As this is simple tubular structure without bends, the dominance of single directional flow can be observed as shown in Figure 4.13(b). Multidirectional flow at the flow initiation region can be seen, where the hypothetical fluid tries to perfuse in all possible directions but gets blocked by the boundary wall and take the maximum length path. Figure 4.13(c) shows structure with aneurysm before flow. In Figure 4.13(d), a vortex is formed both at the aneurysm neck and aneurysm dome.

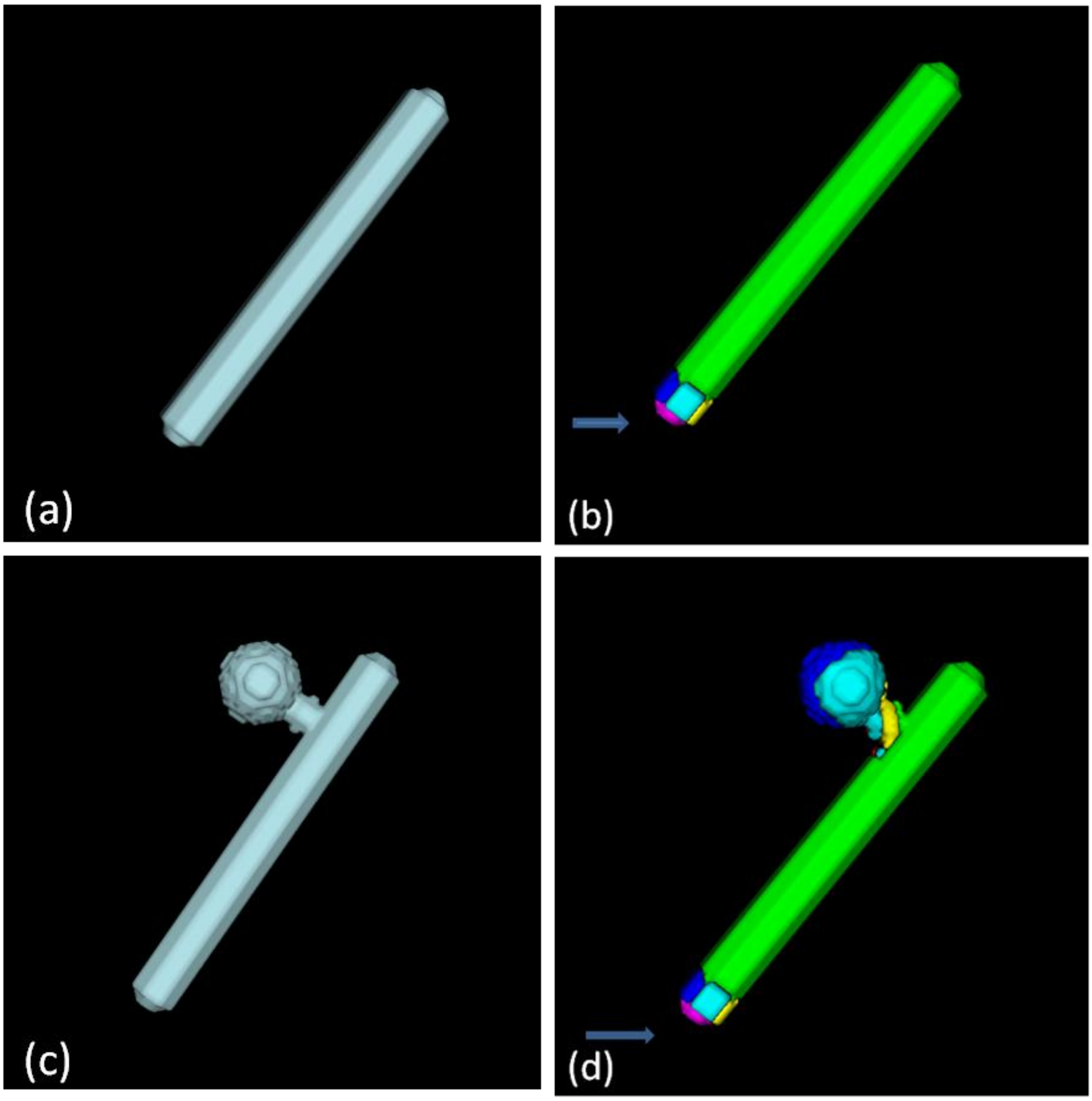

Figure 4.13 Rendering of simple tube a) tube without aneurysm before flow b) tube without aneurysm after flow c) tube with aneurysm before flow d) tube with aneurysm after flow

Figure 4.14 shows the simulation 3-D digital flow in a simple right hand structure. Figure 4.14(a) shows structure without aneurysm before flow. The dominance of single directional flow can be seen in Figure 4.14(b). Counter flow can be seen at the flow initiation region and at the region of bending. Flow starts from the arrow marked point in Figure 4.14(b) and try to perfuse in all possible directions but gets blocked by the boundary wall and take the direction of longest path. Again flow stops at the bending region because here the bending angle is greater than the flow diversion angle (45^0). Flow is reinitiated again from these points and tries to move in all possible directions but takes the direction of longest path.

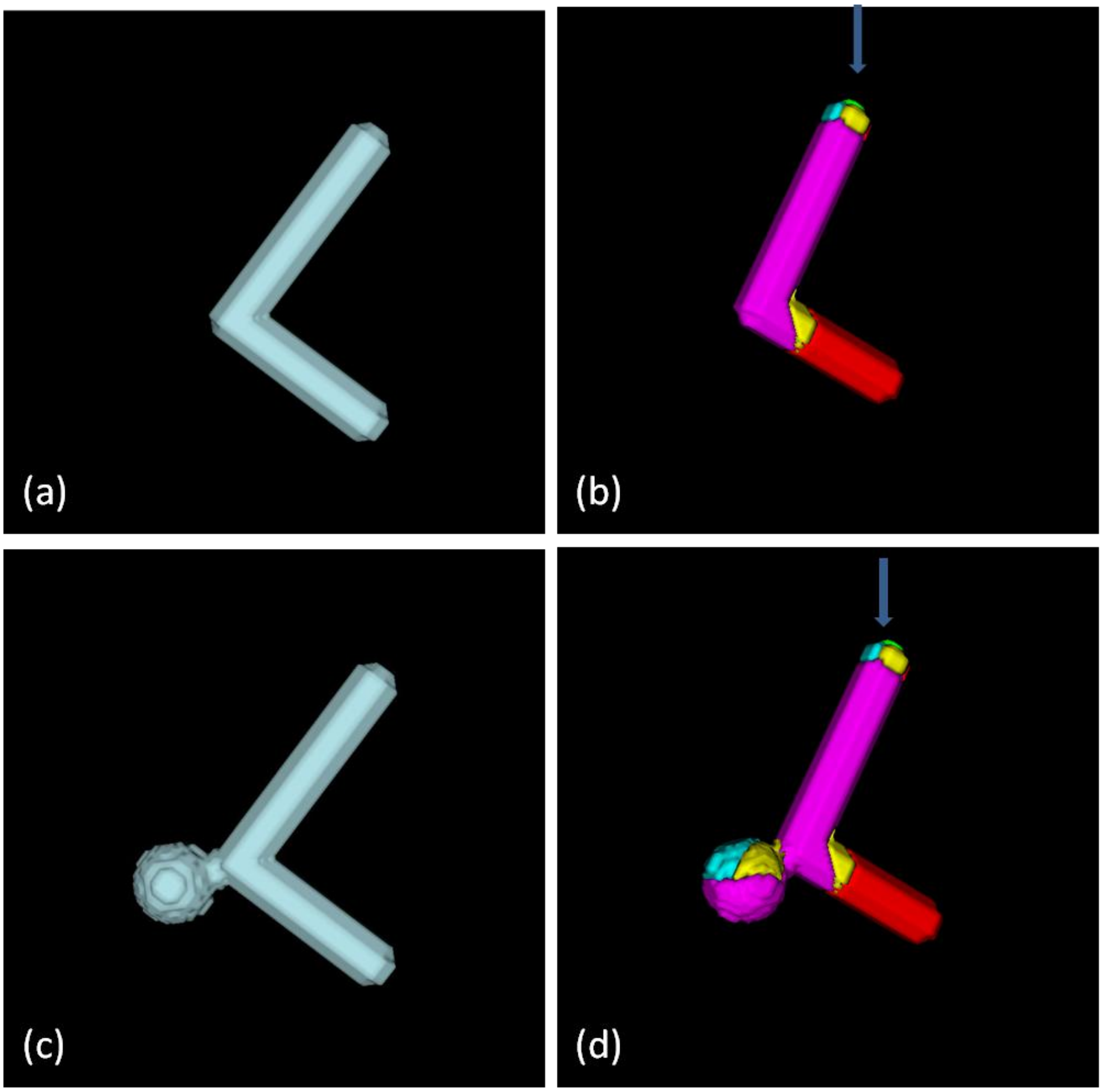

Figure 4.14 Rendering of simple structure a) simple structure without aneurysm before flow b) simple structure without aneurysm after flow c) simple structure with aneurysm before flow d) simple structure with aneurysm after flow

Figure 4.14(c) shows structure with aneurysm before flow. In Figure 4.14(d), counter flow can be seen both at the region of aneurysm and bending region of the curve. At the region of aneurysm initiation flow stops and again restarts, and a vortex is formed. Figure 4.15 shows the T-shape structure and before flow and after flow situation are displayed. Figure 4.15(a) shows structure without aneurysm before flow. In Figure 4.15(b), flow is started from the arrow marked point. It tries to move in the all possible directions but gets blocked by the boundary wall and travels through the maximum length path. Flow gets blocked at the junction as the bending angle is greater than the flow diversion angle and is again restarted. As a result a vortex is formed at the junction area. Figure 4.15(c) shows structure

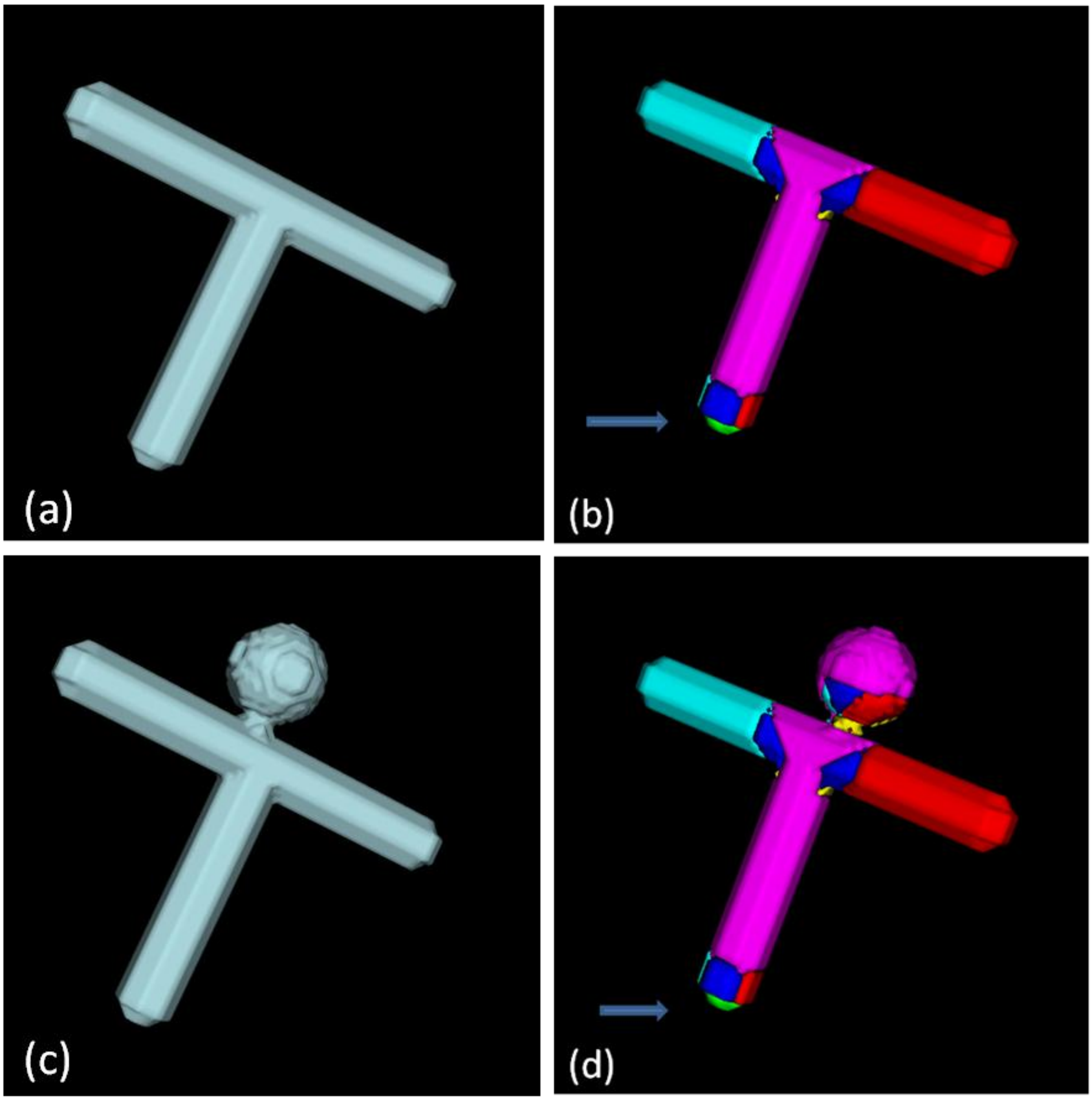

Figure 4.15 Rendering of T-shape structure a) T-shape without aneurysm before flow b) T-shape without aneurysm after flow c) T-shape aneurysm before flow d) T-shape with

with aneurysm before flow Figure 4.15(d) shows the flow signature in T-shape with embedded aneurysm. Vortex can be seen at the aneurysm neck and aneurysm surface also because of the same reason. Figure 4.16 shows flow signature in Y shape like curve. Figure 4.16(a) shows structure without aneurysm before flow. In Figure 4.16(b), one directional flow can be seen except region around the starting point, marked by arrow. Here, flow does not stop at the junction points as the bending angle is not greater than the flow diversion angle. Figure 4.16(c) shows structure with aneurysm before flow. In Figure 4.16(d), vortex is formed at the region around the starting point, around aneurysm initiation and aneurysm

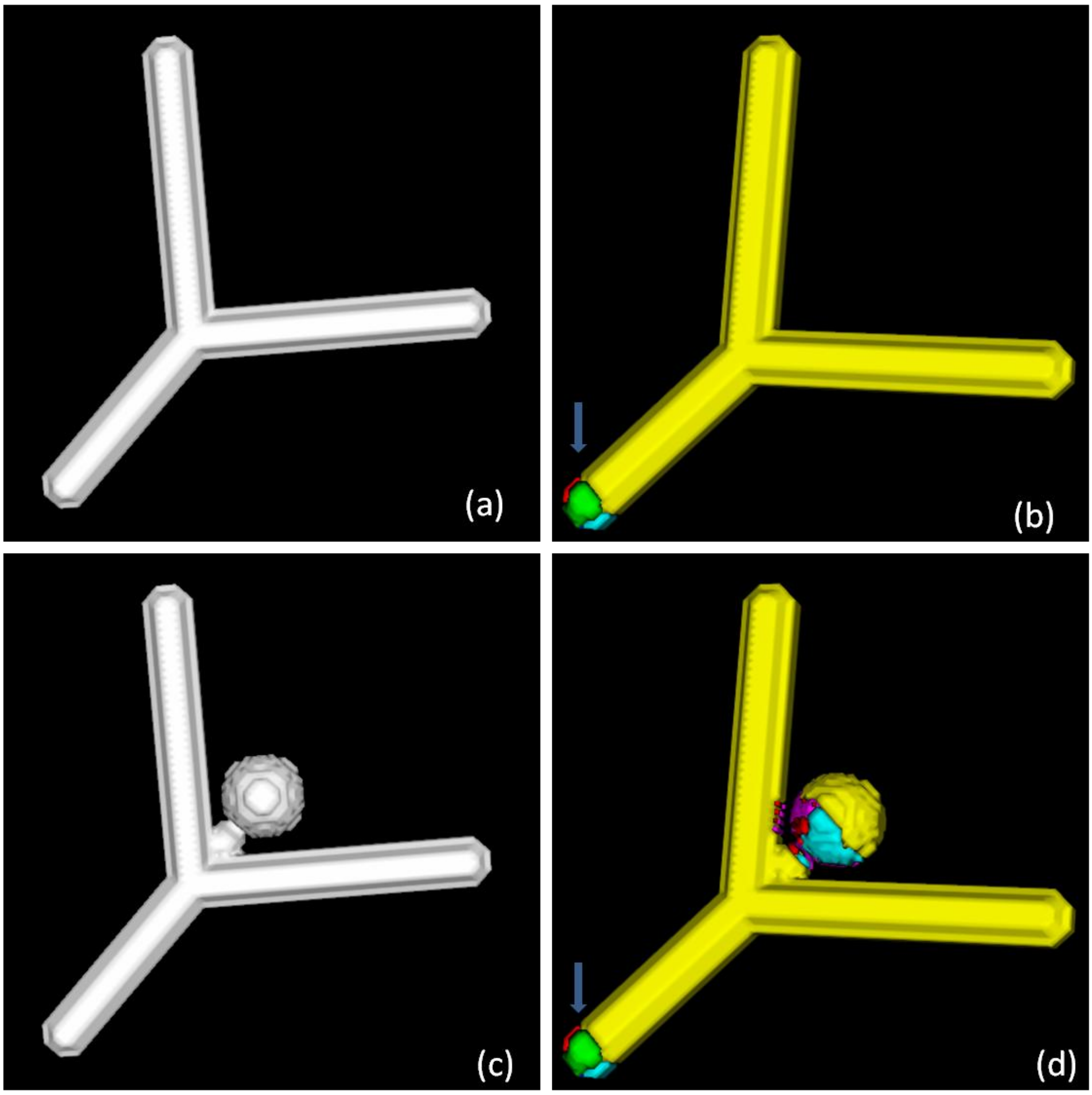

i

Figure 4.16 Rendering of Y-shape a) Y-shape without aneurysm before flow b) Y-shape without aneurysm after flow c) Y-shape aneurysm before flow d) Y-shape with aneurysm after flow

surface. As the bending angle of the curve at aneurysm is greater than the flow diversion angle, counter flow takes place.

4.4.2 3-D Digital Flow in Approximate Cerebrovascular Phantom

Here, the flow signature is analyzed on approximate cerebrovascular phantom. Approximate cerebrovascular phantoms are the geometrical and anatomical model of the

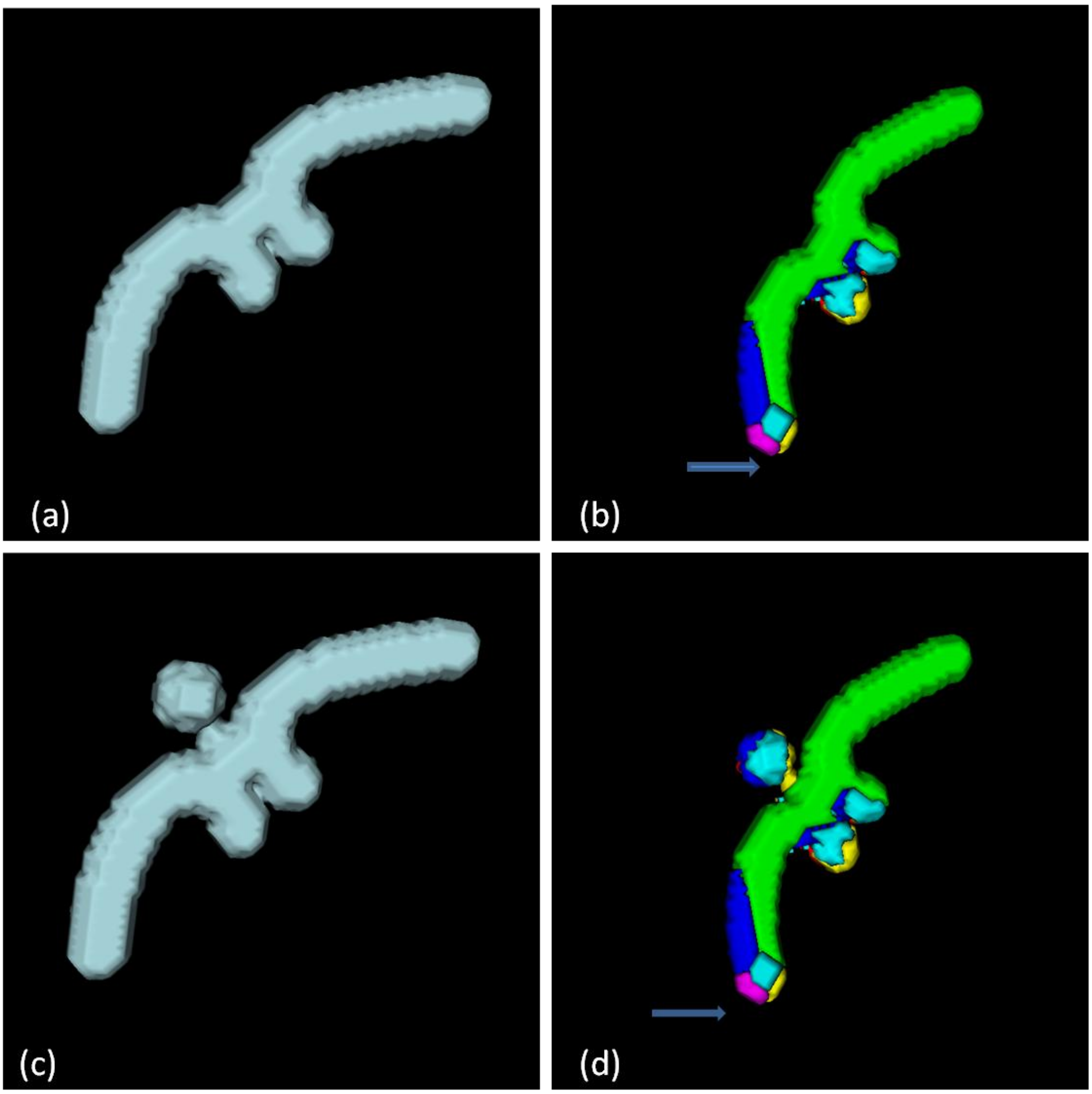

Figure 4.17 Rendering of small ACA segment a) ACA without aneurysm before flow b) ACA without aneurysm after flow c) ACA aneurysm before flow d) ACA with aneurysm after flow

small arterial segments of human cerebrovasculature like ACA, ICA, Basilar Artery, Circle of Willis etc. Figure 4.17 shows the flow directional map on a small ACA segment phantom. Figure 4.17(a) shows structure without aneurysm before flow In Figure 4.17(b), flow is started from the arrow marked point. Multi-directional flow can be seen at many places, as this is a complex curve. A vortex can be seen at the junction region. Figure 4.17(c) shows structure with aneurysm before flow. Figure 4.17(d) shows flow directional map of an ACA segment with aneurysm. Flow is started from the arrow marked point. Flow signatures are same as figure 4.17(b), except an extra vortex is at the aneurysm

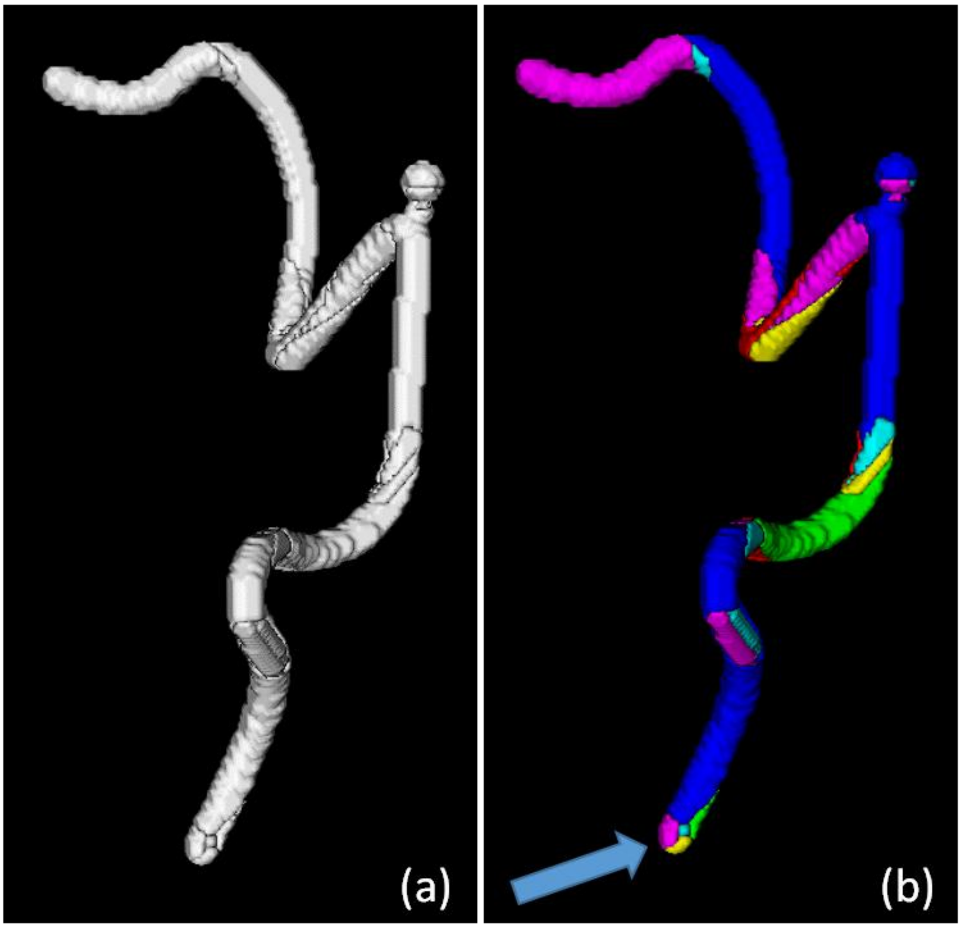

Figure 4.18 Rendering of ICA model a) ICA with aneurysm before flow b) ICA with aneurysm after flow

area. Figure 4.18 shows the flow directional map in an ICA phantom. Figure 4.18(a) shows the ICA structure before flow. Flow is started from the arrow marked point in figure 4.18(b). The dominance of multi-directional flow at the bending regions can be seen, where flow stops and is restarted again. Vortex is formed at the aneurysm area (see Figure (b)). Figure 4.19 shows the flow directional map in Basiler artery and complex bifurcation model. Figure 4.19(a) is the structure of Basiler artery without aneurysm and 4.19(b) is showing the flow directional map in the Basiler arterial structure with aneurysm. Multi-directional flow is observed throughout the curve. In the same way flow directional map is shown for complex bifurcation model without and with aneurysm in 4.19(c) and 4.19(d).

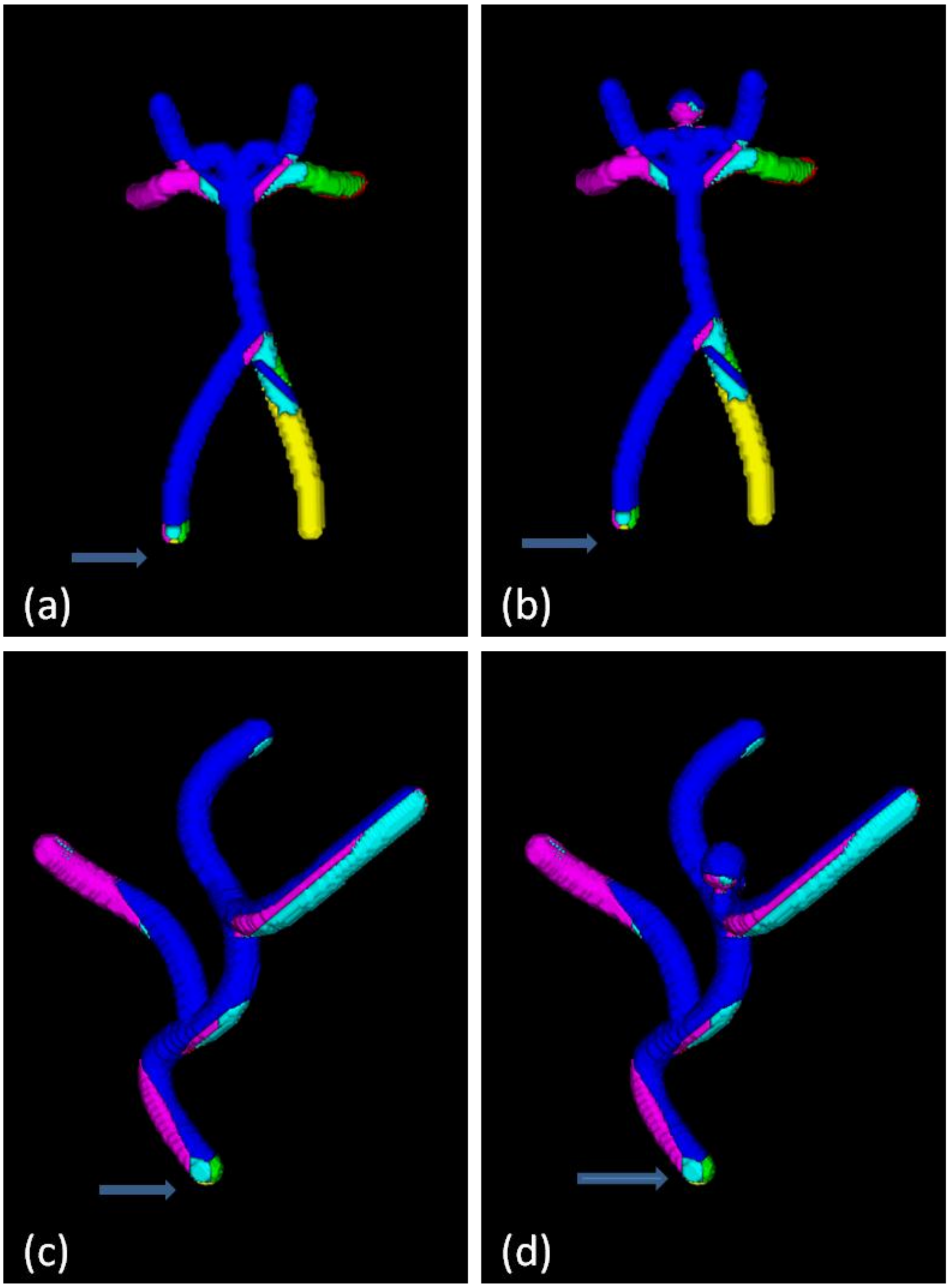

Figure 4.19 a) Basiler artery model without aneurysm after flow b) Basiler artery model with aneurysm after flow c) Complex bifurcation model without aneurysm before flow d) Complex bifurcation model with aneurysm after flow

Figure 4.20 displays the flow signatures in a phantom covering major arteries and Circle of Willis. Figure 4.20(b) to Figure 4.20(e) shows different flow signatures for different starting point of flow. In real blood flow situation it is not possible to assume the underlying geometry to be single inlet. Flow situation slightly differs with respect to real blood flow scenario. This situation may be overcome by multiple flows in single structure.

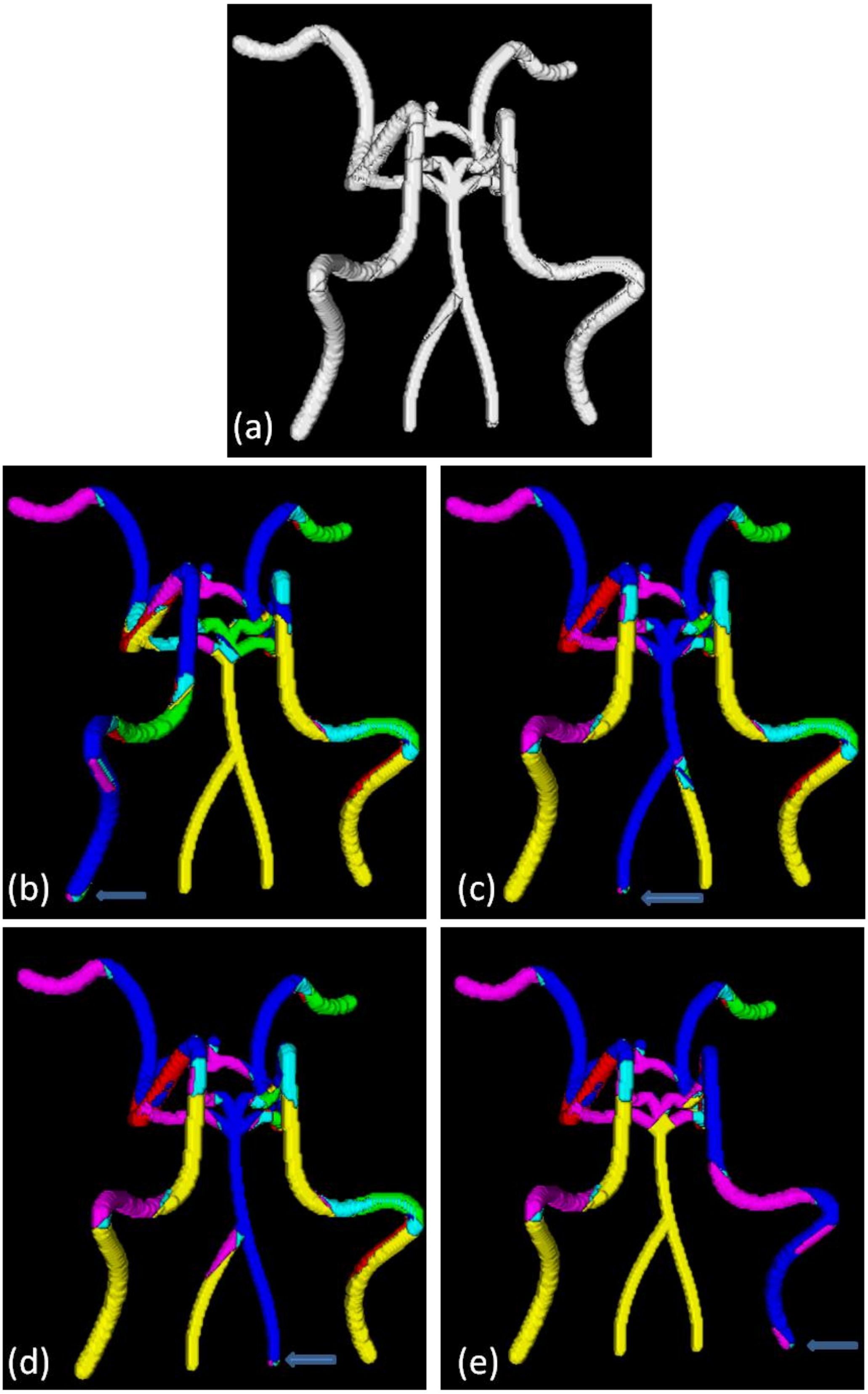

Figure 4.20 Rendering of major arteries and Circle of Willis a) major arteries and Circle of Willis b)-e) flow signatures for the arrow marked starting point

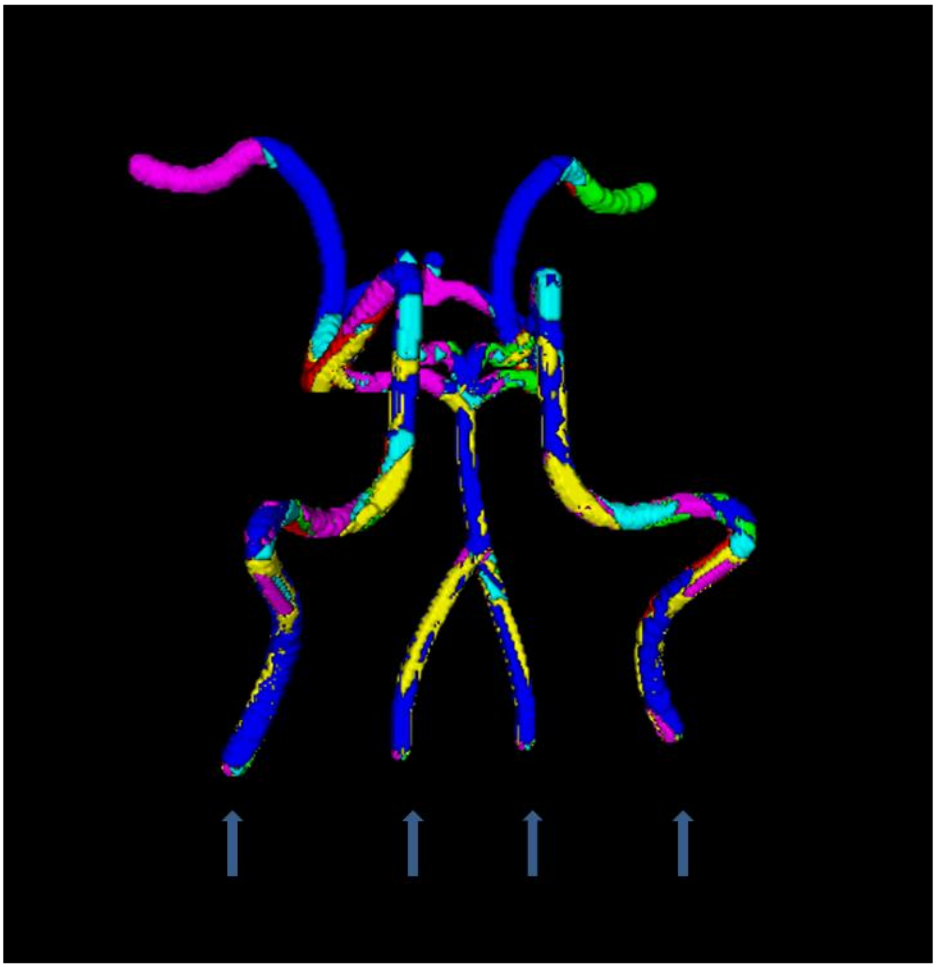

Figure 4.21 Flow direction map in major arteries around the Circle of Willis model according to maximum velocity at each voxel.

For more accurate flow signatures digital phantoms are considered with multiple flow inlets. So phantoms have to be considered with multiple inlet structure i.e. multiple start points of flow. The concept of digital velocity will be used to correctly map the flow signatures which will be close to real blood flow situation. Digital velocity model will be discussed thoroughly in next chapter. In Figure 4.21, flow is started from the each of the four lower extreme ends of the arterial structure. At each voxel the maximum of four different velocity is taken and accordingly the direction of the flow is chosen.

4.4.3 3-D Digital Flow in Cerebrovascular Structure Generated from Human CTA

The 3-D digital flow is finally applied to a third kind of dataset, i.e. segmented arterial structure generated from patient's CTA image. Figure 4.22, 4.23, 4.24, 4.25, 4.26 depict the flow signature for different flow start points in extracted arterial tree of human cerebrovasculature.

To reflect the near accurate blood flow scenario, digital flow velocity model is used. Figure 4.27 depicts the near accurate flow scenario in the extracted arterial structure. Flow is started from all of the extreme ends below the arterial structure.

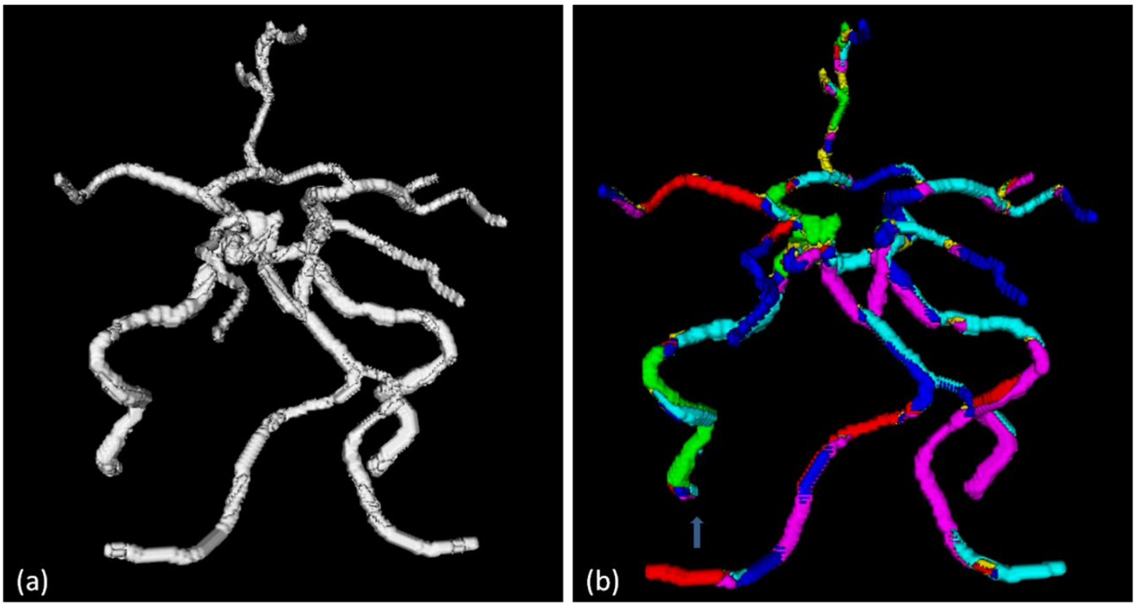

Figure 4.22 Flow signatures on accurate phantom of human cerebrovasculature (a) Phantom before flow (b) Phantom after flow from the starting point marked by arrow.

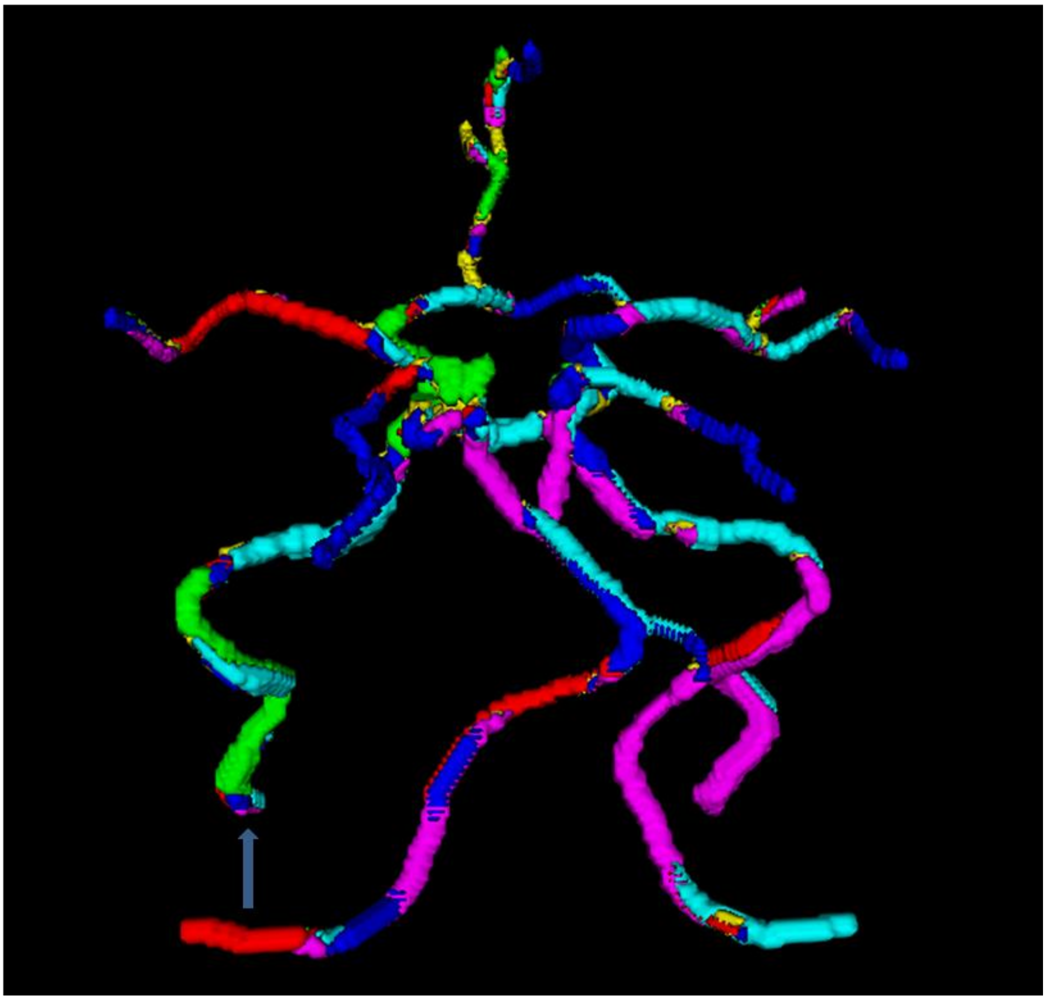

Figure 4.23 Flow signatures on accurate phantom of human cerebrovasculature when the flow start point is the arrow marked point.

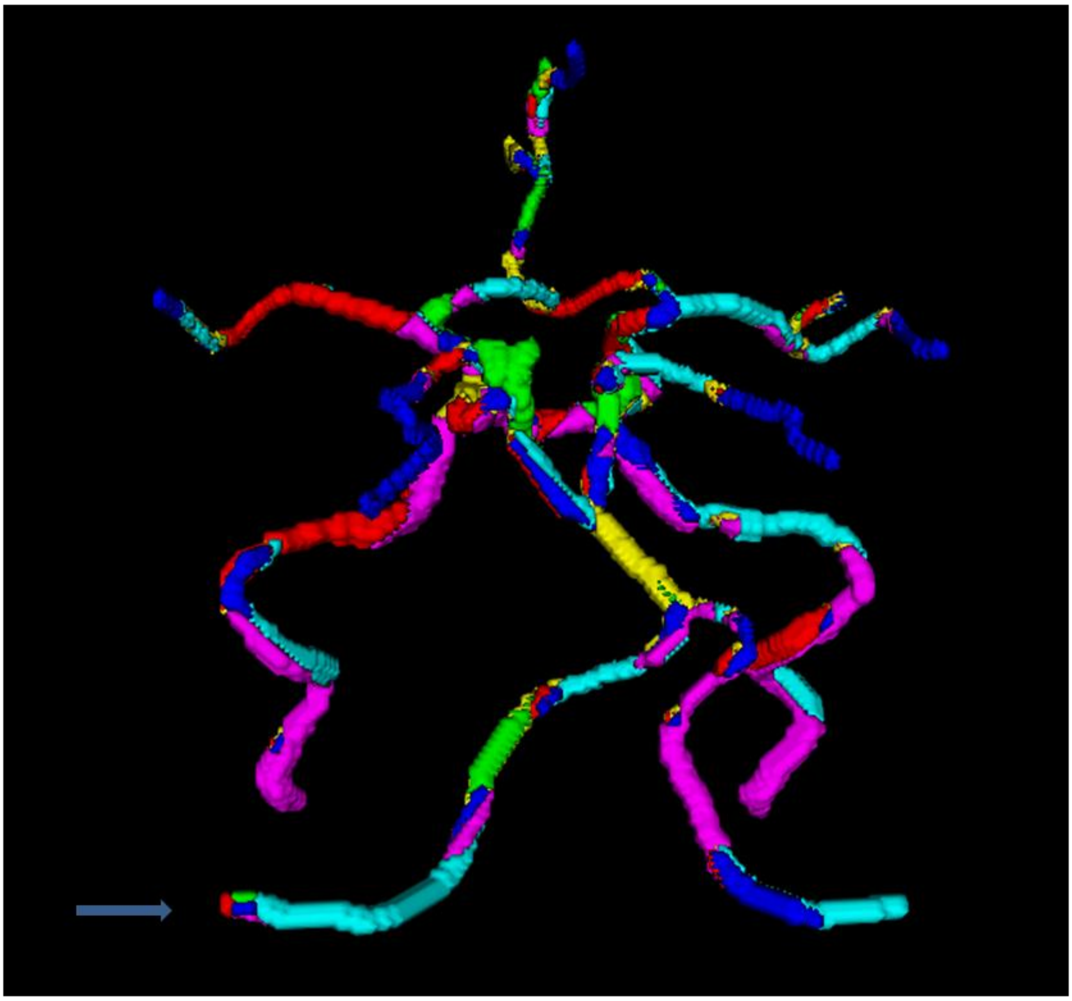

Figure 4.24 Flow signatures on accurate phantom of human cerebrovasculature when the flow star point is the arrow marked point.

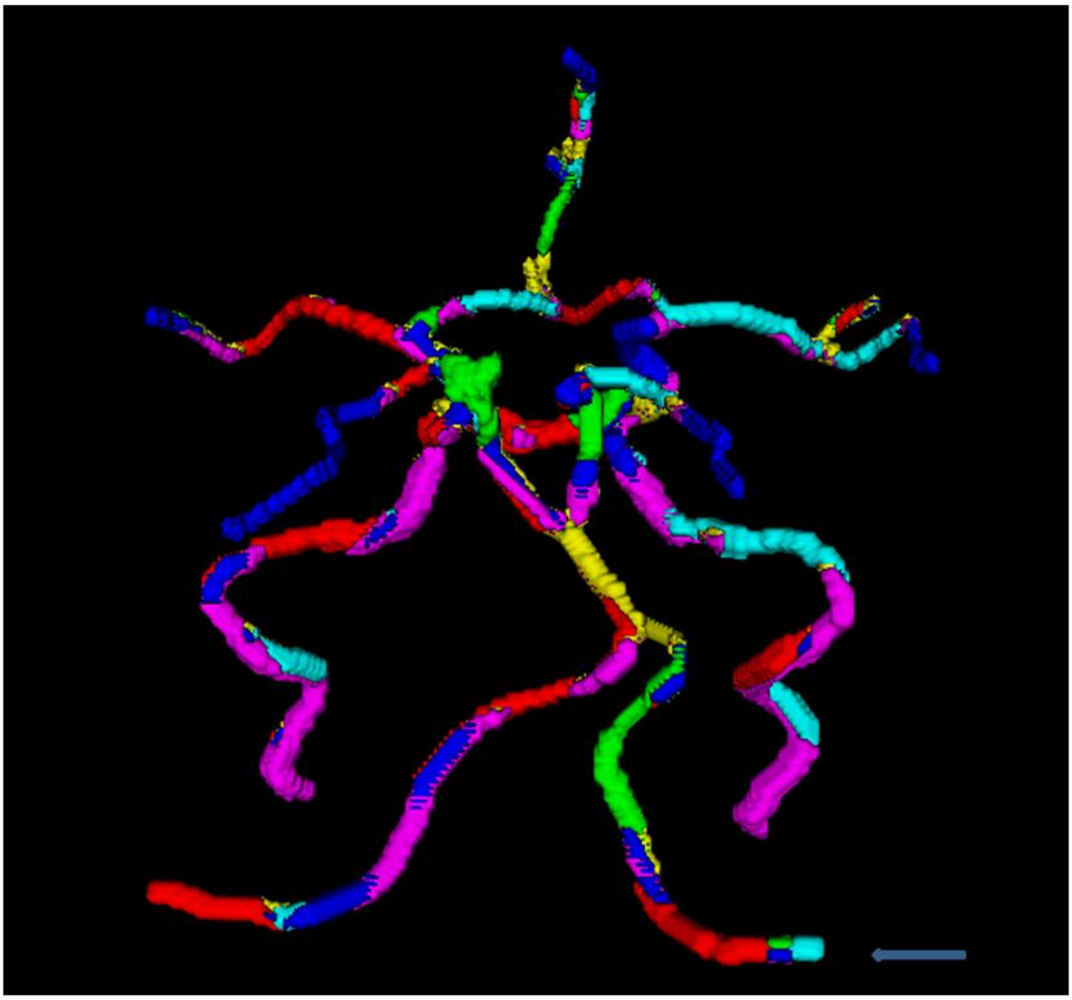

Figure 4.25 Flow signatures on accurate phantom of human cerebrovasculature when the flow start point is the arrow marked point.

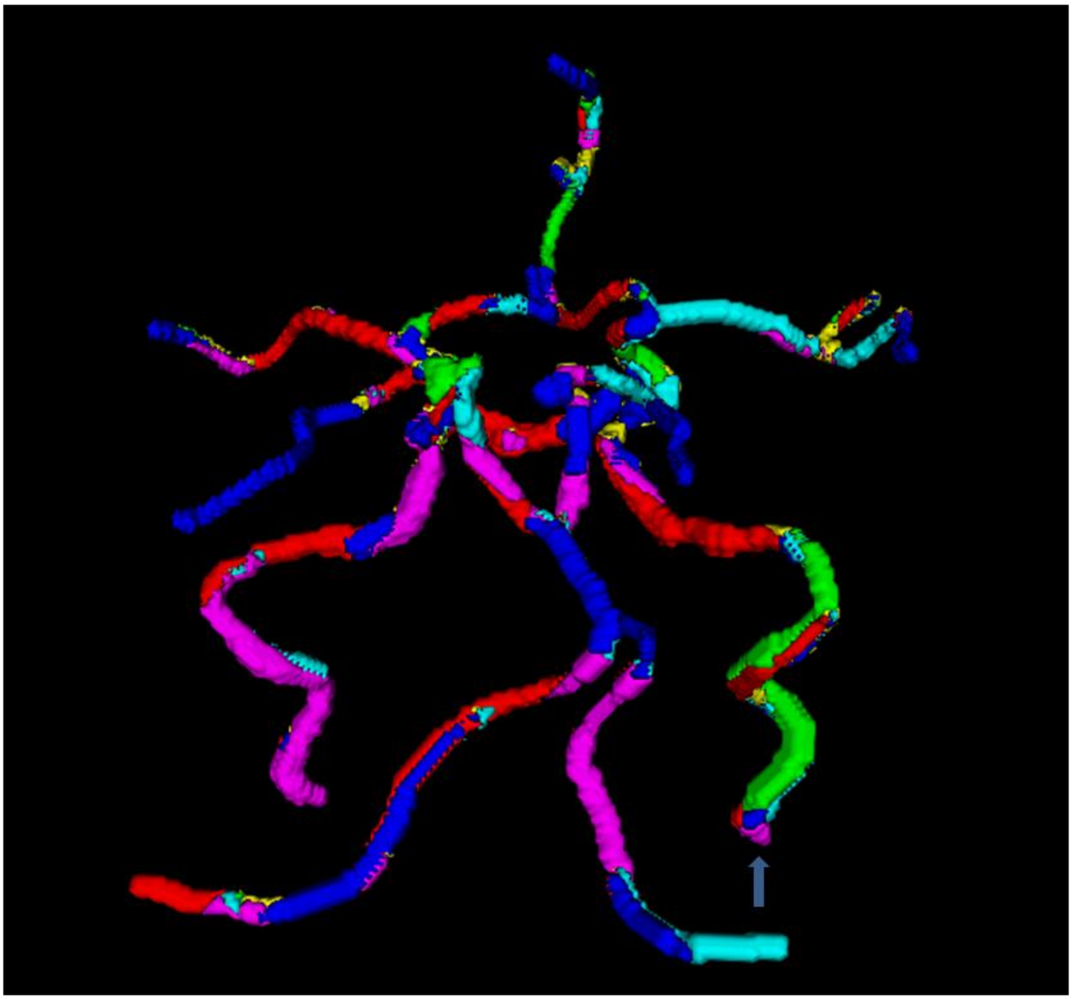

Figure 4.26 Flow signatures on accurate phantom of human cerebrovasculature when the flow start point is the arrow marked point.

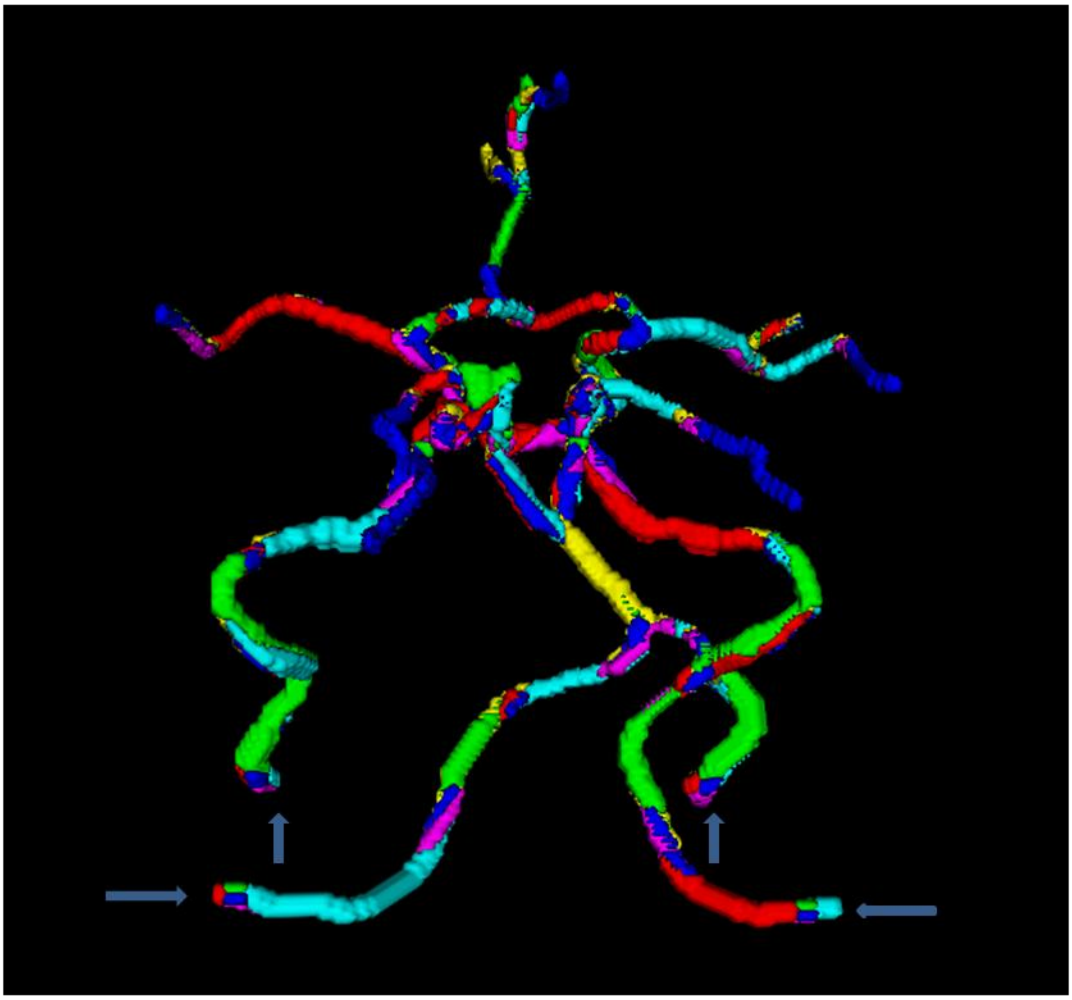

Figure 4.27 Flow direction map on an accurate phantom of major arteries and Circle of Willis extracted from human CTA, according to maximum velocity at each voxel.

4.5 Discussion

As mentioned in the beginning, the 3-D digital flow algorithm is implemented in three different kinds of datasets. This 3-D digital flow is a novel concept and this theory will be used in next chapter for hemodynamic modeling.

Chapter 5

Hemodynamic Modeling of Human Cerebrovascular Structure

Irregular flow transmissions through the blood vessels are the main cause of various vascular diseases. The relationship between the hemodynamic properties and the vascular biology is not yet fully explored. However, any internal flow is strongly influenced by the geometry of its conduit. Hemodynamic parameters like flow velocity, WSS etc. vary from one person to other person due to their specific vascular geometry. The work is motivated to explore how hemodynamic behavior changes due to its underlying arterial geometry.

5.1 Literature Review

The literatures are divided into four major subgroups- (i) The role of hemodynamics on different cerebrovascular diseases, (ii) Relation of hemodynamic shear stress with aneurysm rupture risk, (iii) CFD modeling of hemodynamic characteristics, (iv) WSS and its regional effect on the growth of aneurysm or any anomaly.

(i) The Role of Hemodynamics on Different Cerebrovascular Diseases

A. M. Malek et al. [11] discussed about the role of hemodynamic shear stress in atherosclerosis. A. Sarrami-Foroushani et al. [103] explored how intra-aneurysmal hemodynamics of ICA aneurysm is effected by the heart rate and flow rate in ICA. Basically, hemodynamics is considered to play a significant role in the process of initiation, growth and rupture of intracranial aneurysm. This study also reinforced the significance of patient specific flow analysis and CFD simulation through which the consequence of diverse blood flow situation on the hemodynamics of aneurysm could be assessed.

The above mentioned literatures mainly discussed about the role of hemodynamics in the growth and progression of different cerebrovascular diseases like aneurysm, atheroclerosis.

(ii) Relation of Hemodynamic Shear Stress with Aneurysm Rupture Risk

D. A. Vorp et al. [183] described that rupture or disruption of Abdominal aortic aneurysm (AAA) happens if the mechanical stress value on the aneurysm wall exceeds the power or strength of the tissues of the wall. For this reason, prior realization of the stress distribution of AAA wall is necessary to assess the rupture risk of the aneurysm. They devised a methodology of non-invasive estimation of wall shear stress distribution for real AAAs according to different kind of patients.

M. L. Raghavan et al. [184] had proposed a completely noninvasive method of estimating AAA wall stress distribution that does not involve any added requirement or expenditure for the AAA patient. It is believed that this proposed method may allow for the estimation of rupture risk of an AAA which is more sound biophysically with respect to the widely used criteria of 5-cm AAA diameter.

M. F. Fillinger et al. [185] devised an procedure to do *in vivo* analysis of abdominal aortic aneurysm and its wall stress and rupture risk prediction. This study proposed a new three-dimensional computer modeling method for the calculation of AAA wall stresses for disrupted and symptomatic one. It also worked for electively repaired AAAs. This system uses CT scan data along with blood pressure to evaluate wall stress and compare it with known clinical measure involved in assessing the risk of rupture. According to their test results the value of peak wall stresses which is calculated in vivo at the time of rupture for AAAs found to be greater than the case of electively repaired AAAs. This result persists even when it is matched for maximum diameter.

D. A. Vorp et al. [186] analyzed the impact of wall stress(mechanical), diameter and asymmetry in AAA. The asymmetry of an AAA, and also aneurysm diameter plays a major role in determining mechanical wall stress. Although the critical diameter criterion is a highly influential factor to determine the severity of an AAA, the tendency of disruption might not be same in aneurysms having nearly same diameter.

M. F. Fillinger et al. [187] showed that the wall stress(peak) of AAA in living body is likely to be inflated at the time of rupture than with electively repaired one. This study proposed with a thorough analysis of rupture risk varied over time for the patients who are under observation. For a time period of minimum 6 months, wall stress distributions of AAA of the selected patients were tracked using CT scans. 3-D computer modeling and finite element analysis along with blood pressure are also tracked during observation. According to the noted observations, patients who would have experienced catastrophic outcome had peak AAA wall stress higher to diameter in differential analysis. Elevated wall shear stress causing rupture is not found to be a simple instantaneous event even near the time of rupture.

(iii) CFD Modeling of Hemodynamic Characteristics

A. Chien et al. [188] performed a comparative testing of the hemodynamic properties of smaller aneurysms situated at the same locations. They selected 6 internal carotid arteries, and ophthalmic artery aneurysms that had smaller than 10mm diameter for the study. The proposed method was Image-based CFD in simulative environment for analyzing the hemodynamic properties of aneurysm. Velocity, WSS related to flow were also taken into the observation and both their absolute and relative value were compared with the parent artery. The properties were found same in all small aneurysms (ruptured and unruptured) though for normal and bigger size, WSS is higher in the case of ruptured aneurysms than the unruptured one. The results indicated that the WSS of an aneurysm sac can act as a vital hemodynamic factor linked to growth and rupture of brain aneurysm.

(iv) WSS and its Regional Effect on the Growth of Aneurysm / Other Anomaly

L. Boussel et al. [102] rigorously elucidates how the low WSS region and growth of aneurysm are correlated. For medical treatment or surgery or for any therapeutic decision-making, determination of accurate criteria to predict aneurysm growth and consequent rupture are very important. In this context, study of intra-aneurysmal hemodynamic forces, predominantly WSS is of great importance as it promotes the advancement of aneurysmal disease.

5.2 Research Objective

The above mentioned literatures indicate that growth of the aneurysm is most likely to occur in the regions with abnormally low WSS.

Comparing the WSS distribution in ruptured and unruptured aneurysms, it can be stated that this distribution is higher in the aneurysm sac than the unruptured one. From the literature it is very much clear that hemodynamic parameters like velocity, WSS are suspected to be major factors related to the genesis and progression of some vascular diseases. So, hemodynamic analysis is very much necessary to detect or predict possible anomalous region which may be aneurysm in cerebrovascular structure. In the present work modeling of hemodynamic parameter like velocity and WSS in cerebrovascular structure have been explored with the help of developed 3-D digital flows as well as with the traditional CFD simulation method. Hence the present study has three aspects; (1) hemodynamic modeling using digital flow, (2) hemodynamic modeling using CFD, (3) comparative hemodynamic analysis on human cerebrovascular phantom with and without aneurysm.

5.3 Hemodynamic Analysis using Digital Flow Based Model

Blood flow is the uninterrupted circulation of blood to different body parts through vessel network. In general the physics of blood flow is called hemodynamics. As blood is a very complex and non-newtonian fluid and in addition to that vessels are not at all rigid tubes, the dynamics of blood flow is not well-explainable by classical hydrodynamics, rather best studied in rheology [189]. In this work cerebral blood flow through major arteries is considered. In an adult, the amount of cerebral blood flows per minute is 750 milliliters or 15 percent of the resting cardiac output. When the heart pumps, the blood moves through the blood vessels. Being elastic in nature, the vessel walls, causes the blood and the wall to exert forces on each other that in turn influence their respective motion. Among the several parameters, flow velocity and WSS are considered in the present study.

5.3.1 *Velocity Modeling using 3-D Digital Flow*

In this hypothetical fluid flow model, the fluid nature and important fluid parameter, viscosity is ignored for simplicity. The objective is to create a flow directional map through the underlying complex cerebrovascular geometry to analyze its structural and geometrical properties and detect any irregularity. In this proposed velocity model, flow is initiated with a random velocity and its value changes as the flow propagates and changes its direction. Figure 5.1 depicts the proposed velocity profile.

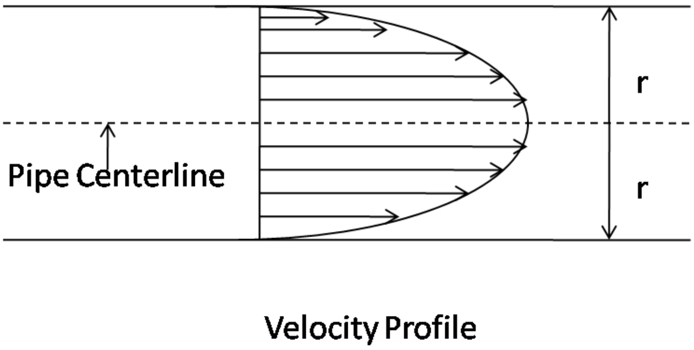

Figure 5.1 Velocity profile of the developed flow model

The assumption is that if the flow initiates from a point in the centerline of the curve, the velocity value is maximum along the centerline of the curve and it decreases towards the boundary of the curve. If the flow is not started from a point in the centerline, the velocity value will not be maximum along the centerline.

Let, V_0 be the initial velocity at the flow start point $S\ (x, y, z) \in C_i$, where C_i is the set of center voxels. Velocity at a voxel(x, y, z), $V_{x,y,z}$ depends on two components: one is flow component of its neighboring voxels and distance of the voxel from centerline.

$$V_{x,y,z} = \mu_F \times FDTR_{(x,y,z)}$$

$$\mu_F = \begin{cases} \max(\mu_i \cos\theta), if\ (x,y,z) is\ among\ 26\ neighbour\ of\ (i,j,k) \in C_i \\ \mu_i, if\ (x,y,z) is\ not\ among\ 26\ neighbour\ of\ (i,j,k) \in C_i \end{cases}$$

where $1 \leq i \leq 26$, $\theta = 0^0$ or $\theta = 35^0$ or $\theta = 45^0$.

$$FDTR_{(x,y,z)} = \frac{FDT(x,y,z)}{FDT(LM)}$$

Where LM is maximum FDT value of center voxel in $N \times N$ neighborhood of (x, y, z) or maximum FDT value in $N \times N$ neighborhood, if no center voxel in $N \times N$ neighborhood exists. Figure 5.1 shows the velocity profile of in a simple tubular structure. Flow is started from the arrow marked point in Figure 5.2(a). From Figure 5.2(b), it can be observed that the uniform and highest velocity exist along the centerline and it decreases towards the boundary wall.

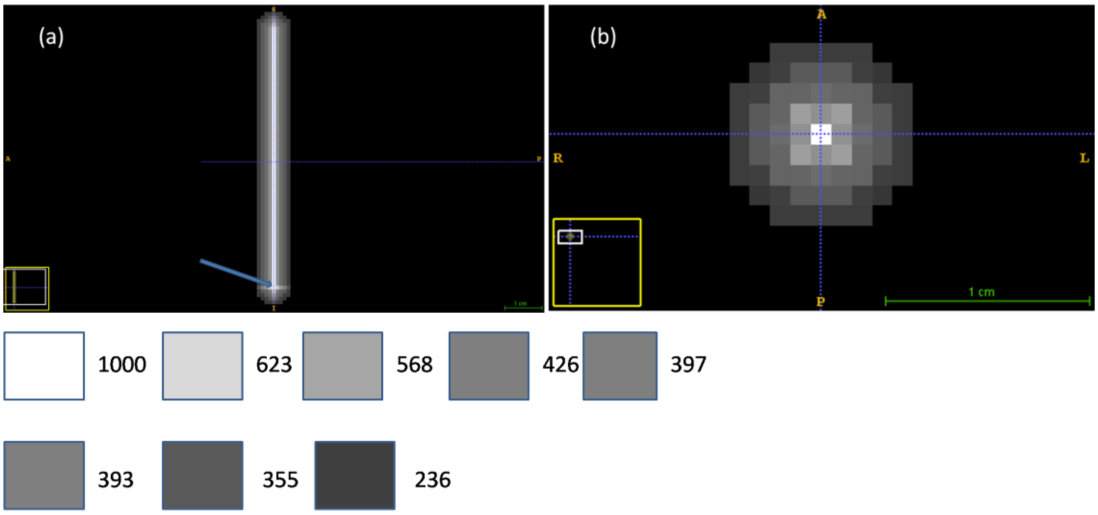

Figure 5.2 Velocity profile in a simple tubular structure a) Flow started from the arrow marked point and middle view of the tube b) top view of the tube

5.3.2 WSS modeling using 3-D digital flow

Due to viscosity, flow of blood engenders on the luminal vessel wall a frictional force per unit area known as hemodynamic shear stress. In arterial blood flow, the WSS expresses the force per unit area exerted by the wall on the fluid in a direction on the local tangent plane. There is substantial evidence that the WSS induced by the pulsatile blood flow in the arterial system affects the atherogenic process [190]. It is now widely accepted that the vessel segments that appear to be at the highest risk for development of atherosclerosis are those with low WSS or oscillating WSS, represents as τ_ω, such that

$$\tau_\omega = \mu\left(\frac{\partial u}{\partial y}\right)$$

Where μ is the dynamic viscosity, u is the flow velocity parallel to the wall and y is the distance to the wall.

In digital flow based model WSS at any point $P(x, y, z)$,

$$WSS(x, y, z) = rdmap(x, y, z) * FVPS(x, y, z),$$

where, rdmap(x,y,z)=rfdt(x,y,z)/rm(x,y,z).

rfdt = reverse fuzzy distance transform

rm = nearest local maxima in rfdt matrix

FVPS= flow value obtained from neighborhood.

In this present study as WSS is represented with the help of flow value and rdmap which is actually the rfdt value i.e. reverse fuzzy distance transform [191] in normalized form. Reverse fuzzy distance transform is the distance of any point from the centerline of the image.

5.4 Hemodynamic Analysis using CFD Model

The conventional move toward the study of the hemodynamic characteristics is the numerical simulation using finite element method [192]. Reconstruction of 3-D vascular structure using finite element methods with subsequent processing on that is a great challenge. Phantoms of human cerebrovasculature which are used for the present analysis, are designed using the Bezier curve based approach which is described in Chapter 2.

In this Chapter the CFD based hemodynamic analysis on two cerebrovascular phantoms, an anterior communicating artery, and a complete arterial tree including the *Circle-of-Willis,* will be done.

Here the step by step process involved in converting the surface mesh to a solid, which is needed for flow analysis using ANSYS Fluent software [95] are shown. Then, the analysis of velocity and WSS which are well known hemodynamic parameters have been performed using CFD simulations. A qualitative hemodynamic analysis on human cerebrovascular phantom is performed in this present study after doing several preprocessing tasks [193].

5.4.1 Preprocessing of 3-D Reconstruction for Flow Analysis

To do in depth hemodynamic analysis for carotid vasculature, development of appropriate 3-D mathematical model is one of the crucial tasks to be performed. To do the hemodynamic analysis through the finite element modeling synthetic 3-D structures are needed, resembling human carotid arteries. It is informative to note that the 3-D reconstruction involves two phases. During the first phase, cerebrovascular phantoms are designed which is discussed in Chapter 2 and then get a 3-D surface reconstruction for hemodynamic analysis. The second phase of the 3-D reconstruction process involves the conversion of the 3-D surface to a 3-D solid mesh. In case of complex structures, they have to be processed through different pre-processing methods that discard spurious edges and vertices etc. For generation of the initial surface mesh and for the rendering purpose MeshLab_64bit_v1.3.4BETA is used [194]. To convert the surface mesh to solid mesh, Rhinoceros 5.0 [195] have been used. Figure 5.3 (a) shows the initial surface mesh of a sample ACA phantom.

Figure 5.3 (b) shows the surface mesh of the same structure after edge and vertex reduction. The quality of the mesh has been improved through some methods in Meshlab 64bit. Figure 5.3 (c) shows the Moving Least Squares (MLS) projection of the phantom. In the Figure 5.3 (d-e) more preprocessing techniques have been applied to make the structure smoother. The quality of the mesh is represented using the color code, where “blue” regions represent best mesh quality. It may be observed, that the mesh quality has improved through different preprocessing steps applied on the structures, as shown in Figure 5.3(c-e). After all the smoothening operations, resurfacing method is applied over the phantom (see Figure 5.3 (f)). Conversion of the surface mesh to solid mesh using Rhinoceros 5.0 is shown in Figure 5.4.

5.4.2 Flow analysis using ANSYS

ANSYS [95] is a well-known CFD software and is used in this study for hemodynamic analysis on the cerebrovascular phantoms. It is widely used as a standard tool for finite element analysis. The Fluent module of ANSYS Workbench 16.0 is used here to analyze different hemodynamic parameters through flow analysis.

The solid structure of the 3-D phantom is loaded in the design modeler of ANSYS is shown in Figure 5.5(a). Then the mesh is generated on the structure where inlet and outlets are specified in “Red” regions (see Figure 5.5 (b)). Now this mesh structure is ready for subsequent flow analysis. Another major component of the cerebrovascular structure is the *Circle of Willis*. This is as shown in Figure 5.6 as a part of the complete cerebrovascular phantom. Here the final result is shown after converting the surface mesh to solid, without showing all the intermediate steps.

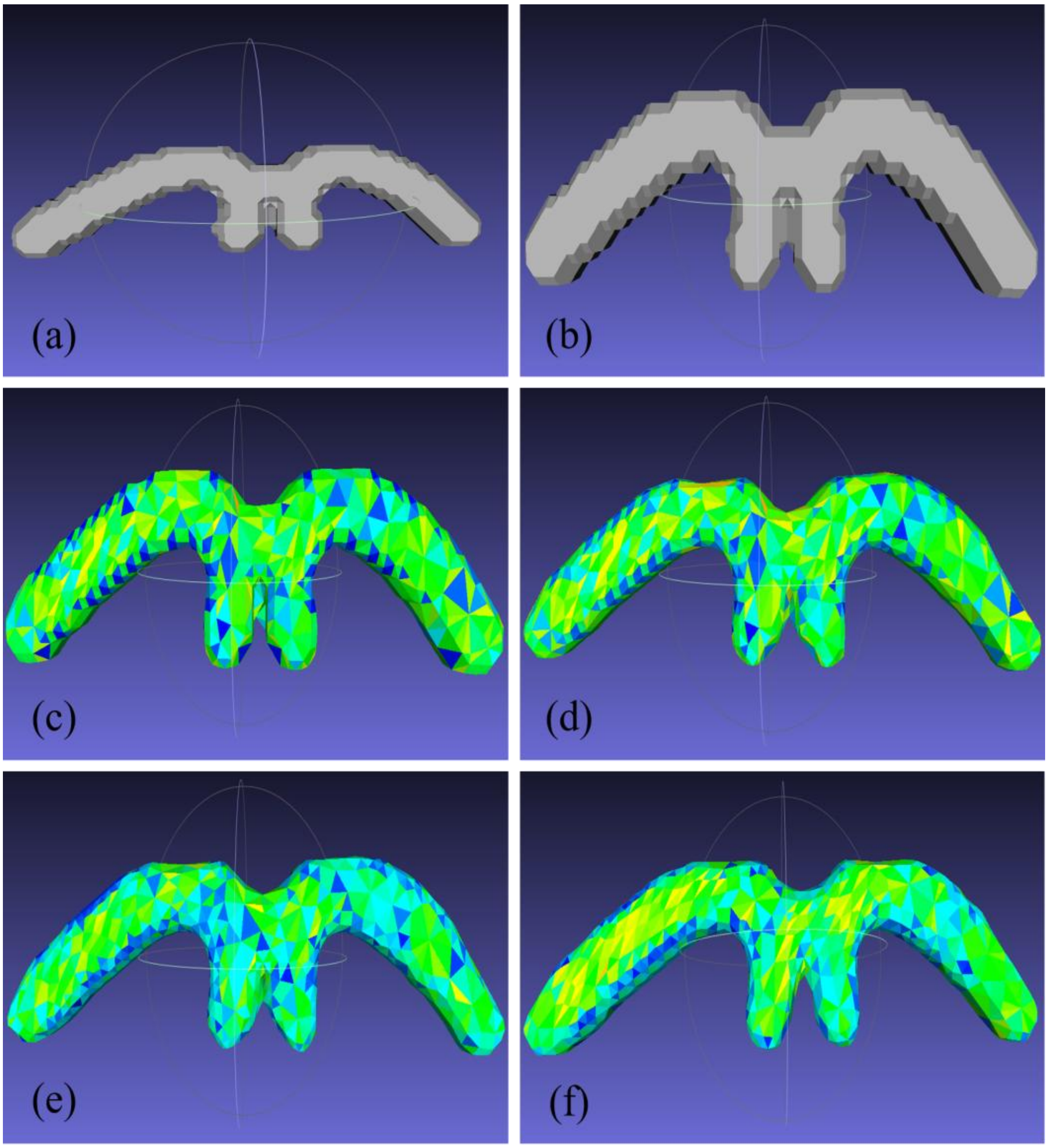

Figure 5.3 Rendering of 3-D cerebrovascular phantom for ACA (a) Initial Mesh (b) after edge reduction (c) after MLS projection (d) after Laplacian smoothening (e) after Taubin smoothing (f) final mesh after resurfacing and mesh enhancement.

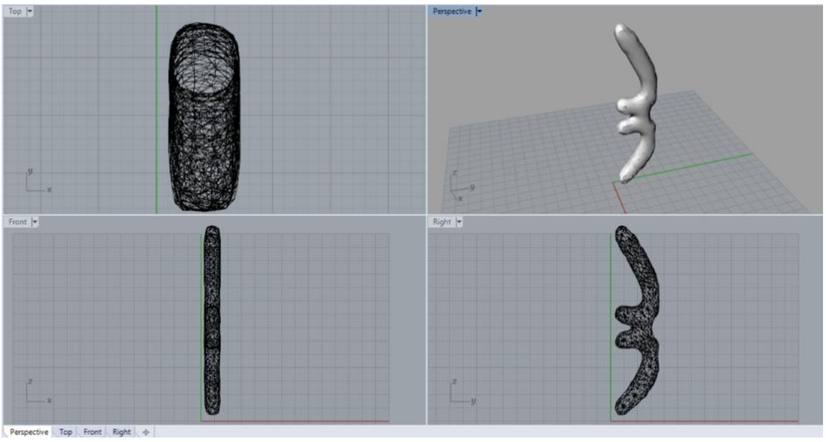

Figure 5.4 Conversion from initial surface mesh to solid mesh in Rhinoceros 5.0

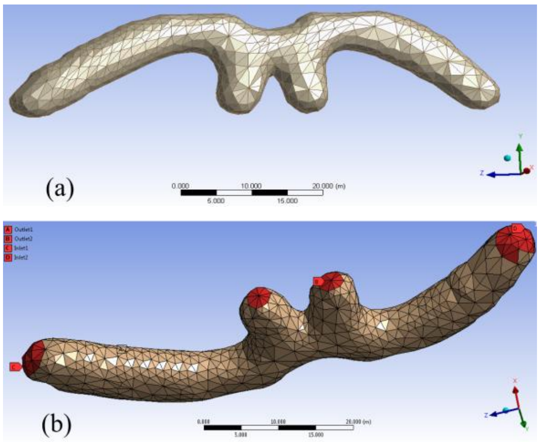

Figure 5.5 Meshing of solid model. (a) Solid design model in Ansys (b) Meshing in Ansys

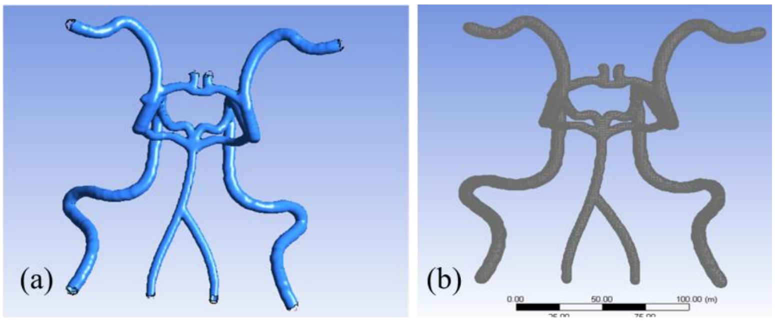

Figure 5.6 (a) Phantom of major arteries of human cerebrovasculature along with *Circle of Willis* (b) Mesh

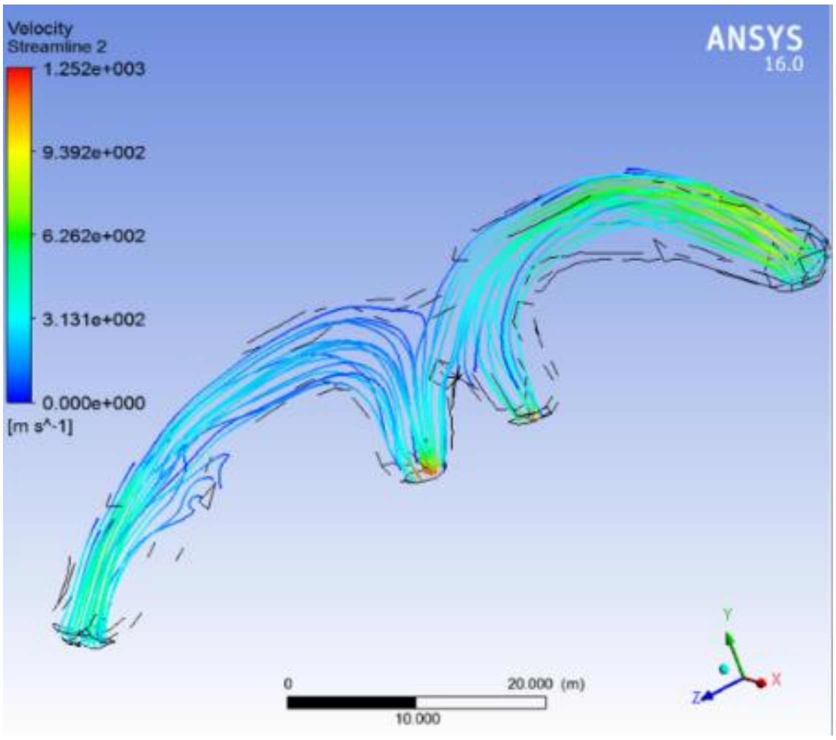

Figure 5.7 Flow through cerebrovascular phantom (ACA)

Velocity and WSS are the major hemodynamic parameters which are analyzed in the present work. The result using ANSYS Fluent software is shown in a contour filled way. Figure 5.7 shows the flow through cerebrovascular phantom. In Figure 5.8, the contour is filled with the velocity magnitude. In Figure 5.9, the WSS distribution for this phantom has been shown. The graphical representation of velocity magnitude is shown in Figure 5.10.

Finally, Figure 5.11 shows the result of flow analysis through the complete vasculature phantom which consists of major parts of carotid arterial structure including *Circle-of-Willis*. Here the lower four arterial regions are considered as inlets and the outlets are assumed in the upper sides of the arteries. The "Blue" regions show low velocity and shear stress in the vasculature, while the "Red" regions represent the highest velocity and shear stress respectively.

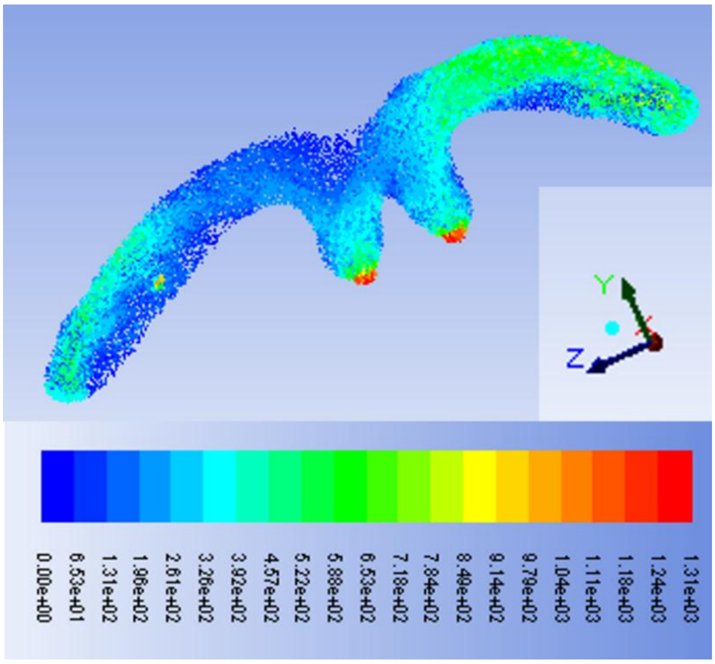

Figure 5.8 Contour of velocity magnitude for ACA

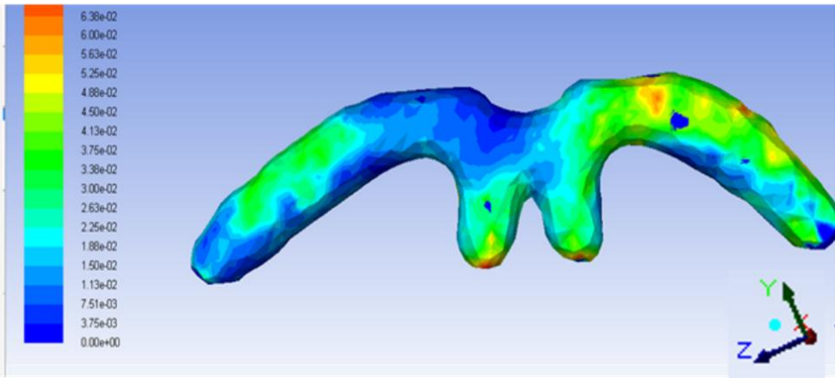

Figure 5.9 Contour of WSS (ACA)

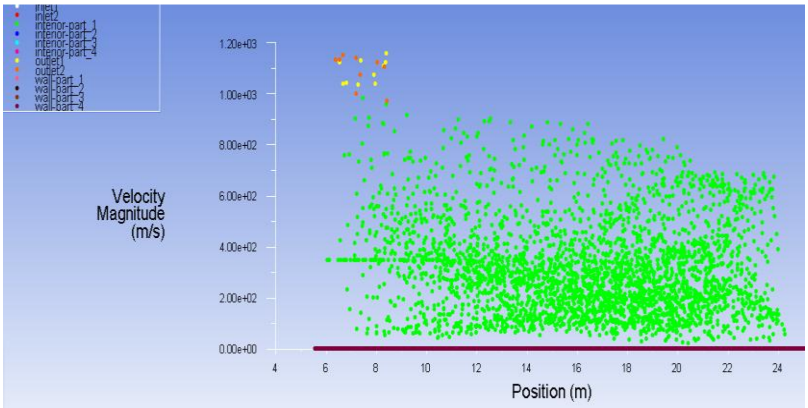

Figure 5.10 Velocity magnitude (ACA)

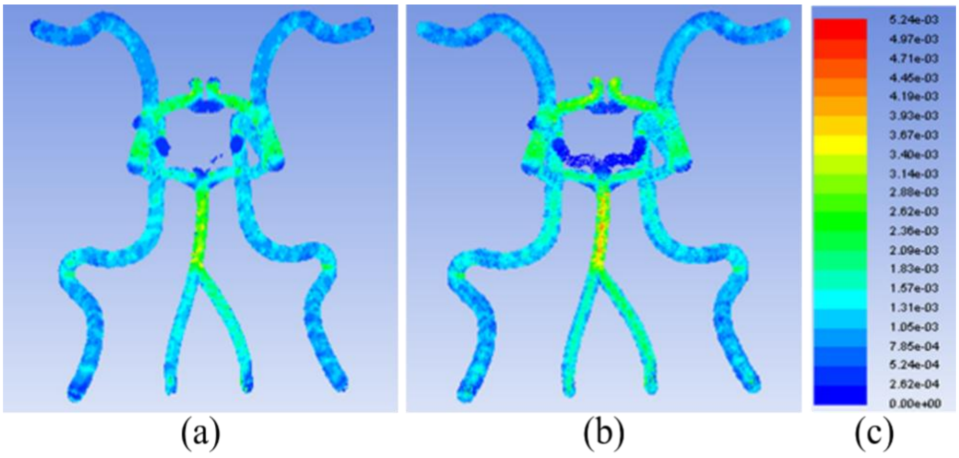

(a) (b) (c)

Figure 5.11 (a) Contours of WSS (b) Velocity vectors (*Circle-of -Willis*) (c) Transition of values with the transition from blue to red

5.5 Comparative Hemodynamic Analysis on Human Cerebrovascular Phantom with and without Aneurysm

Cerebral aneurysm, as discussed earlier, is an outpouch in the vessel wall located in the brain [196]. There is no such known preventive measure for this disease as the cause of this disease is not known. Numerous studies to know the particulars of hemodynamics of the artery, are being performed. Several studies have been tried to discover appropriate hemodynamic properties which correlates to the aneurysm initiation. Study of hemodynamic parameter like the blood pressure, velocity and WSS are performed to be connected to the development of the aneurysm [197][105]. The WSS affect on the growth of an aneurysm by acting directly on the endothelium cell. Moreover, high WSS magnitude or high spatial and temporal variation of WSS might mechanically damage the inner wall of artery [188][183].

In this connection, the purpose of the work presented here is to study the CFD based flow analysis and the effect of selected hemodynamic parameters on different cerebrovascular phantoms with and without aneurysm. A comparative hemodynamic analysis on human cerebrovascular phantoms with and without aneurysm is performed in this present study [198].

The first step is to preprocess or make ready the cerebrovascular structure with and without aneurysm for flow analysis using method discussed in section 5.4.1. Then flow analysis can be done through CFD based software ANSYS Fluent [95].

Some cerebrovascular structure with and without aneurysm are shown in following Figure 5.12.

In Figure 5.13(a) one complex bifurcation phantom geometry without aneurysm is shown and it underwent through flow analysis to get velocity vector (in Figure 5.13(b)), WSS (in Figure 5.13(c)) and static pressure (in Figure 5.13(d)). In Figure 5.14 the same complex bifurcation phantom but with aneurysm is considered. The mesh structure of the geometry of Figure 5.14(a) is shown in Figure 5.14(b). Mesh generation is one of the important steps before doing the flow analysis. Velocity and WSS are shown in Figure 5.14(c) and Figure 5.14(d) respectively.

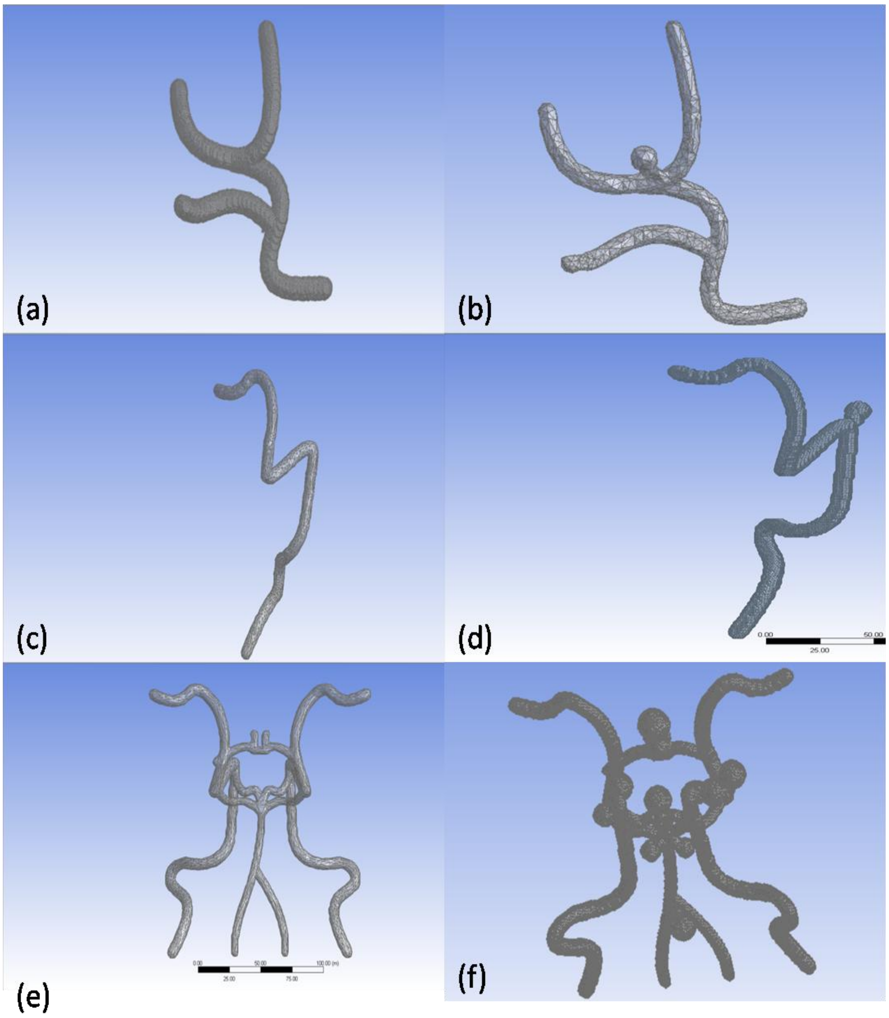

Figure 5.12 (a) Complex bifurcation structure without aneurysm (b) complex bifurcation structure with aneurysm (c) ICA (internal carotid artery) without aneurysm (d) ICA (internal carotid artery) with aneurysm (e) *Circle of Willis* without aneurysm (f) *Circle of Willis* with aneurysm

Analysis of the ICA (Internal carotid artery) without aneurysm is depicted in Figure 5.15. In Figure 5.15(a) mesh, Figure 5.15(b) flow streamline, Figure 5.15(c) velocity, Figure 5.15(d) static pressure are shown respectively. In Figure 5.16 the same phantom geometry (ICA) with aneurysm is analyzed. In Figure 5.16 (a) geometry (b) flow streamline (c) velocity (d) WSS are developed and shown respectively.

From the Figure 5.13, Figure 5.14, Figure 5.15 and Figure 5.16 it is very clear that there are several changes in hemodynamic parameter values if the phantom structure includes any aneurysm.

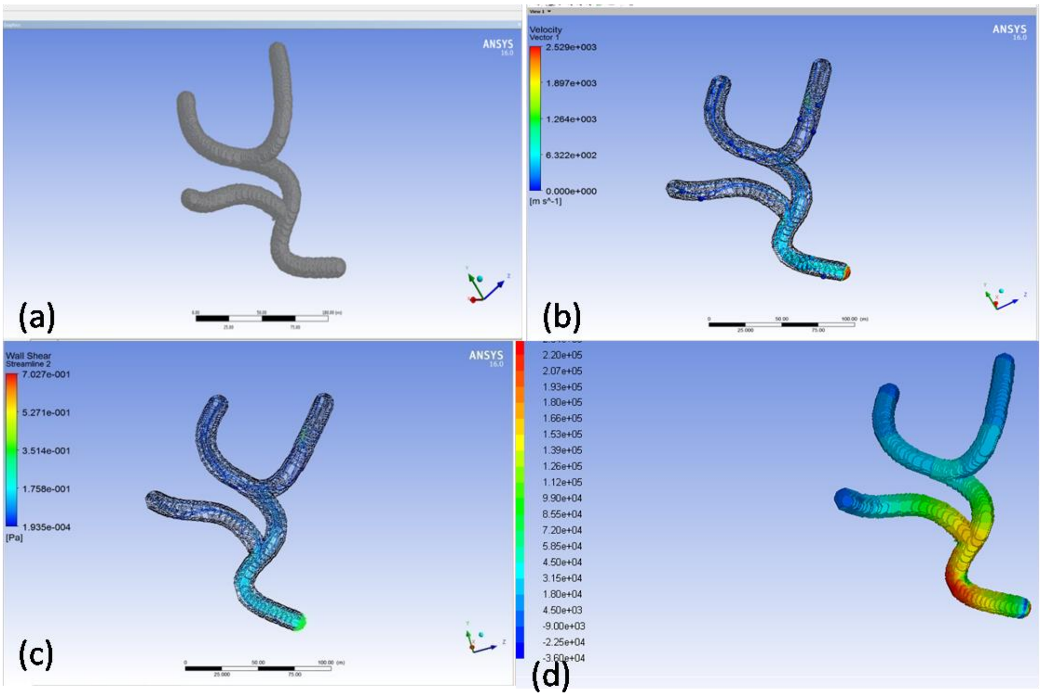

Figure. 5.13 Complex bifurcation without aneurysm (a) geometry (b) velocity vector (c) WSS (d) static pressure

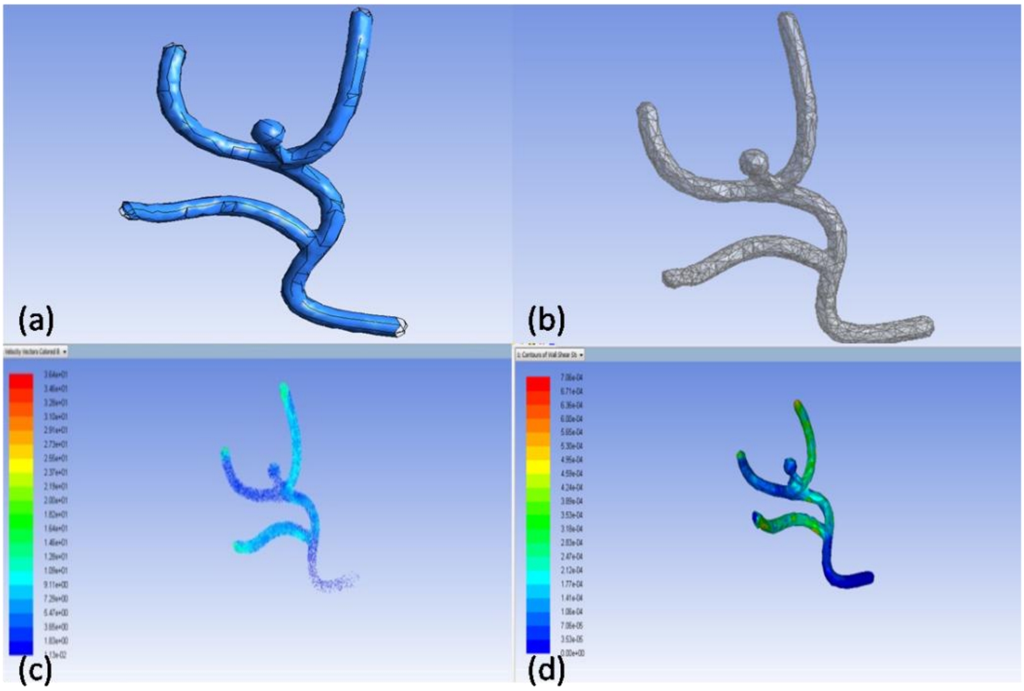

Figure 5.14 Complex bifurcation with aneurysm (a) geometry (b) mesh (c) velocity vector (d) WSS

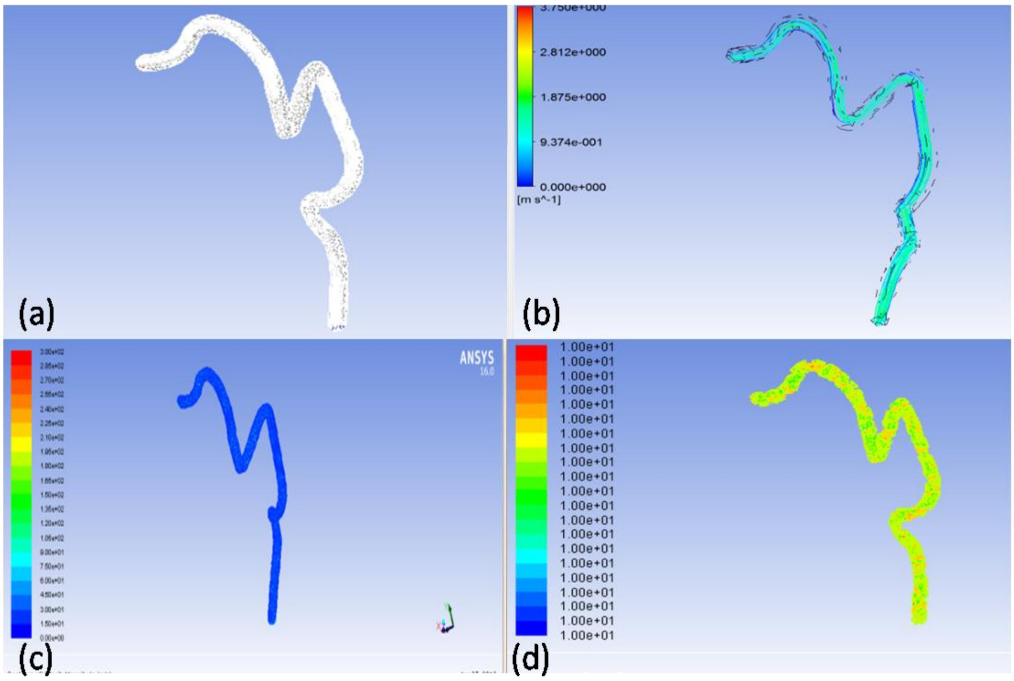

Figure 5.15 ICA without aneurysm (a) mesh (b) flow streamline (c) velocity (d) static pressure

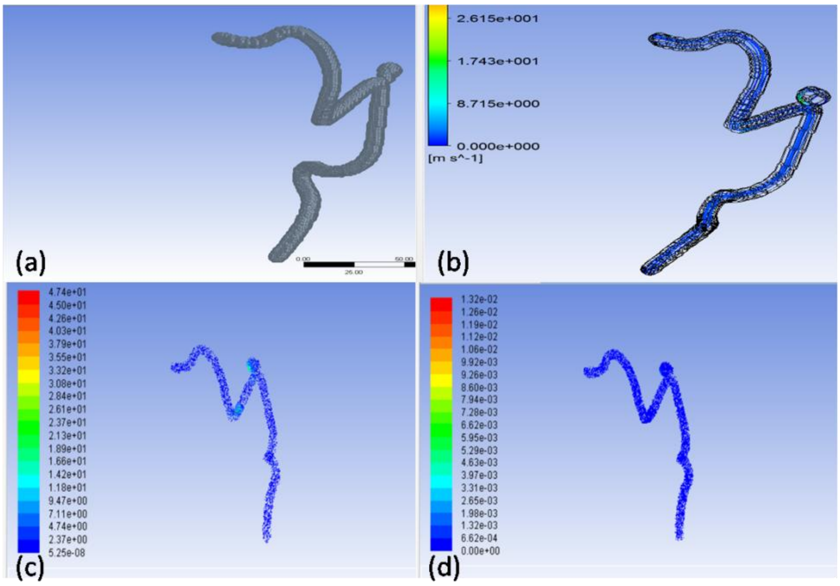

Figure 5.16 ICA (Internal carotid artery) with aneurysm (a) geometry (b) flow streamline (c) velocity (d) WSS

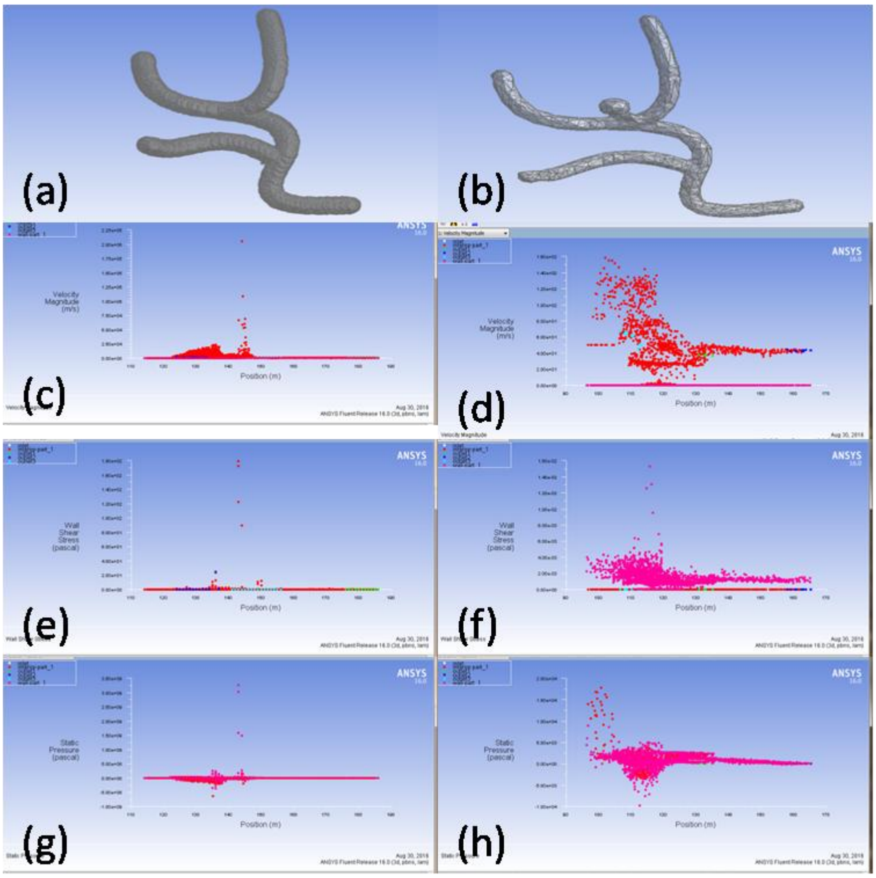

Figure 5.17 Comparison of hemodynamic parameter through flow analysis on complex bifurcation phantom with and without aneurysm (a) the phantom without aneurysm (b)the phantom with aneurysm (c)velocity of the phantom without aneurysm (d) velocity of the phantom with aneurysm (e) WSS of the phantom without aneurysm (f) WSS of the phantom with aneurysm (g) static pressure of the phantom without aneurysm (h) static pressure of the phantom with aneurysm.

The comparisons of hemodynamic parameters like velocity, WSS and static pressure on complex bifurcation phantom with and without aneurysm are performed in the present work. The result is shown in Figure 5.17(a)-(h). From the Figure 5.17 it can be easily stated that there is turbulence in the flow on the phantom which is with the aneurysm. This statement can be stated because it can be observed that there is a variation in the ranges of values for the hemodynamic parameters. For the numerical simulation of hemodynamic parameter in finite element method ANSYS16.0 [95] has been used.

5.6 Discussion

In this present study the utility of the hemodynamic modeling and analysis through novel digital flow based model as well as with CFD have been emphasized. The velocity and WSS models are developed through digital flow based model. In the second part which is regarding CFD modeling, first ACA phantom then secondly major parts of cerebrovasculature including *Circle-of-Willis* were prepared for flow analysis using ANSYS Fluent module. Analysis of fluid dynamic parameters reveals important structural properties. The color coded images represent both qualitative and quantitative maps of the digital phantoms. These results are useful for understanding of fluid flows through cerebral vasculature and help to determine the turbulent flow nature which will provide sufficient evidence to find the anomaly in cerebrovascular structure.

Chapter 6

Anomaly Detection in Human Cerebrovascular Structure

Identification of anomalies in human cerebrovascular structure is very important in predicting and assessing cerebrovascular diseases. Cerebral aneurysm is one of the vascular diseases which cause a number of deaths worldwide and so it is very crucial for clinicians to predict it. It is reasonable to assume that rupture risk assessment can be improved by incorporating hemodynamic analysis as it is usually thought to play an essential role in the process of initiation, progression and rupture of aneurysm. Hemodynamic parameters like WSS, velocity information are essential to assess the health of the critical arterial segments. In the current work a novel 3-D digital flow based model has been used to estimate these vital parameters from the segmented cerebrovasculature of patients' CTA. The present study also includes comparison of the hemodynamic parameters on several cerebrovascular structures with and without aneurysm and to find key features from the arterial segments for possible classification of anomalous regions from healthy segments and prediction of aneurysm like structures and subsequent detection of rupture risk of the same.

6.1 Literature Survey

The following literatures consist of three major categories: (i) Classification model to detect aneurysm; (ii) Rupture risk prediction; (iii) Intra-aneurysmal hemodynamic characteristics for risk assessment using CFD models.

(i) Classification Model to Detect Aneurysm

Y. Wang et al. [199] studied on gene expression in surrounding blood cells to characterize the status of Thoracic aortic aneurysm (TAA) and subtypes of that. 94 peripheral blood samples were collected to get gene expression profiles. They identified 41 gene classifiers which are based on signature of gene expression to recognize TAA patients. The classifier genes can describe a set of potential diagnostic markers to set the stage or status of a blood-based gene expression to facilitate early detection of TAA. They achieved 80% classification accuracy on the testing set.

(ii) Rupture risk prediction

J. Shum et al. [200] studied on the estimation of AAA rupture risk. They experimented on 76 aneurysms for which 10 are ruptured and 66 are unruptured. A non-invasive method of assessment of AAA shape was implemented. From CTA images some arterial part is segmented which consists of aneurysm and 3-D models were generated. A prediction model was developed to determine the rupture risk with some selected features. The model had achieved with the accuracy of 86.6% for prediction.

M. F. Fillinger et al. [187] analyzed the rupture risk of patients with AAA under observation. They compared the effect of WSS and diameter of aneurysm to predict the rupture risk. They used CT scans of patients with AAA. Analysis was performed on 103 patients' CT scan. Receiver operating characteristic (ROC) curves for peak wall stress to predict the rupture risk were better (sensitivity- 94%; specificity-81%; accuracy- 85% [with 44 N/cm^2 threshold]) than for diameter (sensitivity- 81%; specificity-70%; accuracy- 73% [with 5.5 cm threshold]. They concluded that peak AAA wall stress seems to be better to diameter in prediction of the rupture risk of patients with AAA.

(iii) Intra-Aneurysmal Hemodynamic Characteristics for Risk Assessment using CFD Models

J. R. Cebral et al. [201] studied on the relation between hemodynamic factors and the rupture of cerebral aneurysms. Intra-aneurysmal hemodynamics is derived from CFD models. 3D angiography images are used to construct patient-specific 62 models of cerebral aneurysms. A variety of flow signatures or flow patterns were found. 72% of cases with ruptured aneurysms having unstable or compound flow patterns whereas 80% had small impingement regions, and 76% had small jet sizes. With contrast to this, 73%, 82%, and 75% of aneurysms with simple steady flow patterns, large impingement regions, and large jet sizes are found respectively for unruptured aneurysm. Using these three features, they designed the prediction model of rupture risk.

S. M. Moore et al. [104] developed CFD models of the Circle-of-Willis (1-D and 3-D) to provide a simulation tool that can be used to identify cerebral arterial structure which is at risk. M.L Raghaban et al. [105] discussed about the evaluation of the need for surgical intervention in an abdominal aortic aneurysm (AAA) to avoid rupture, information and understanding of wall stresses are very much necessary. S. M. Moore et al. [104] identified the cerebral arterial geometries which are at risk by developing some CFD models as simulation tool. These literatures are stated in detail in chapter 1 and discussed about the aneurysmal hemodynamic analysis and risk assessment.

6.2 Research Objective

From the literature it is clear that detection of anomalous region is one of the vital jobs to predict some cerebrovascular diseases. Analysis and study of the human vasculature and classification of anomalous part and normal part of the human cerebrovasculature signify a lot because diseases like aneurysm which is caused by some anomalies in vascular structure as well as in hemodynamic parameters.

The main purpose of the work, described here, is to classify the normal and anomalous voxels of the cerebrovascular segments through features extracted from the 3-D flow analysis. For that, at the outset, medical data is needed. It is already discussed that real medical data collection is very troublesome and requires patient permission. So, besides the real data some phantom data are also prepared to study the hemodynamic parameters thoroughly. The phantom design methodology is already discussed in chapter 2 of the thesis.

6.3 Present Work

In the current work, 3-D digital flow based model is used to extract different hemodynamic parameters like velocity, WSS etc. from cerebrovascular structures. These hemodynamic parameters and different flow based features are then combined to classify the anomalous regions from the healthy parts of the cerebrovascular structure. The overall work is divided in to the following modules.

1. Design of datasets of cerebrovascular segments using methods which are depicted in Chapter 2 and 3 of the thesis.
2. 3-D digital flow in the cerebrovascular segments using the method is discussed in Chapter 4 of the thesis.
3. Design of the feature set (described in Section 6.3).
4. Classification of anomalous and normal regions of vascular structure using the designed feature set (discussed in section 6.3.3 and 6.3.4).
5. Analysis and comparison of classification results (in section 6.4).

6.3.1 Design of Some Cerebrovascular Structure with and without Aneurysm

There are two types of cerebrovascular structures used in the study, 1) mathematically generated synthetic phantoms, and 2) segmented patients’ CTA data. Phantoms of Cerebrovascular structures like ICA, Basilar Artery with and without aneurysm, as shown in Figure 6.1(a), Figure 6.1(c) and Figure 6.2(a), Figure 6.2(c) respectively, are constructed through the methods, discussed in Chapter 2 and Chapter 3.

6.3.2 Generation of 3D Digital Flow through Cerebrovascular Structures

To do the hemodynamic analysis, 3-D digital flow is to be generated through the cerebrovascular structure. The method of generating the 3-D digital flow is discussed in chapter 4. The ICA and Basilar Artery vascular structures with and without aneurysm and the digital flow through these structures are shown in Figure 6.1 and Figure 6.2

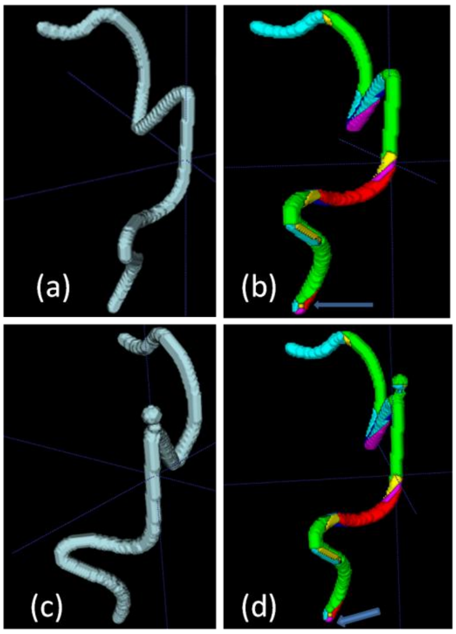

Figure 6.1 (a) ICA without aneurysm (b) flow in ICA without aneurysm (c) ICA with aneurysm (d) flow in ICA with aneurysm

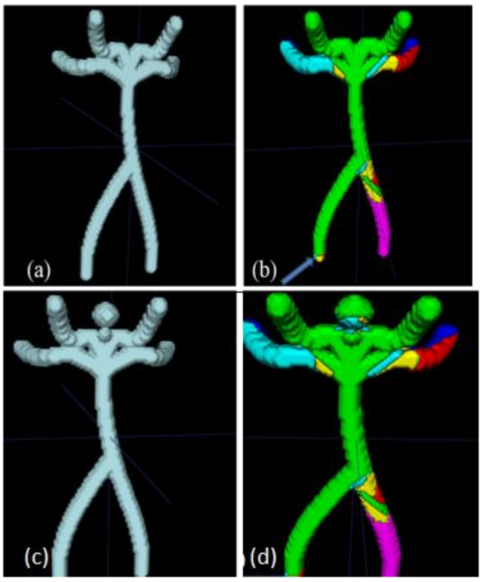

Figure 6.2 Flow nature in phantom of human Basilar Artery (a) Basilar Artery phantom before flow (b) Flow nature in Basilar Artery phantom after flow from left extreme end (c) B Basilar Artery phantom with aneurysm (d) B Basilar Artery phantom with aneurysm after flow from left extreme end

respectively. After flow image of the ICA with and without aneurysm is shown in Figure 6.1(b) and Figure 6.1(d) respectively.

6.3.3 Design of the Feature Set

To design the feature set, two different sets of parameters are extracted from the dataset, 1) hemodynamic attributes like velocity and WSS, and 2) flow based parameters. As discussed before, two types of datasets are considered, i.e., structures with and without aneurysms. For extraction of features from the dataset 3-D digital flow is first applied and both flow based parameters and hemodynamic parameters are estimated for each voxel of the structure. In this work, 12 different features are extracted in the 3x3x3 neighbourhood of each voxel. Designed features are briefly listed below.

Flow based features: Every voxel represents any one of 6 different directional flows, viz., flow in X+ve, X-ve, Y+ve, Y-ve, Z+ve and Z-ve directions. The first feature counts the number of different directional flows in each 3x3x3 region, centering each voxel. The second feature estimates the number of background voxels in each 26-neighbourhood. Six more features are estimated in each such neighbourhood to count the number of flows in any of the six directions mentioned before.

Hemodynamic features: For each voxel, flow velocity and WSS of each voxel are considered as two features. Two more features are extracted as mean, standard deviation of the velocity in the corresponding neighborhood of each voxel.

6.3.4 Classification

In this present study the main objective is to classify the anomalous and normal regions of carotid arterial structures and predict about some arterial diseases. Normal and anomalous regions in 3-D human cerebrovascular phantom are classified [202]. Anomalous regions of human cerebrovascular structure are classified using Random Forest classifier [203]. A modified classification model have been developed with a different feature set of these above mentioned work [202][203]. This modified and improved work is discussed as follows.

As already stated that mainly the aneurysm disease is considered here, some of the vascular structure with aneurysm and some without aneurysm are taken as training data.

The aneurysm part is actually anomalous part and remaining part is normal. By labelling the aneurysm part as anomalous and remaining part as normal, classifier is trained with some known samples and then the ability of the classifier to identify the anomalous and normal regions, is tested on some unknown samples of cerebrovascular structures. For the classification purpose the first step is to design the feature set which is discussed in section 6.3. As a ground truth the voxels are categorised as follows. Total number of instances is 35913.

Table 6.1 Instance count and their weights

Class	Count	Weight
Normal	34884	34884
Anomaly	1029	1029

To analyze the performance of the trained classifier, following evaluation metrics, based on the true positives (TP), true negative(TN), false positive(FP), false negative(FN) measures are used.

$$\text{Accuracy} = \frac{\text{TP+TN}}{\text{TP+FP+FN+TN}}$$

$$\text{True Positive Rate (TPR)} = \frac{\text{TP}}{\text{TP+FN}}$$

$$\text{False Positive Rate (FPR)} = \frac{\text{FP}}{\text{FP+TN}}$$

$$\text{Precision} = \frac{\text{TP}}{\text{TP+FP}}$$

$$\text{Recall} = \frac{\text{TP}}{\text{TP+FN}}$$

In the present study, Multi-layer perceptrons, and Random forests are chosen as classifiers and their performances are analyzed and compared in identifying the anomalous and normal regions in a vascular structure.

6.3.4.1 Multi-Layer Perceptrons

Multi-layer perceptrons (MLP) is perhaps the most useful type of Artificial neural networks, called simply as neural networks [204]. It is a well known field which investigates and solve complicated computational job like the predictive or explorative modeling with simple biological models [205]. A MLP is a class of feed-forward artificial neural network and consists of at least three layers of nodes [206]. For training, MLP uses a supervised learning method called backpropagation.

The power of neural networks actually means the ability of learning the training data and how to relate this to the target variable which is to be predicted [207]. Basically neural networks are capable to learn a mapping. Neural networks get their predictive capability from the hierarchical or multi-layered structure of the networks [208]. The building block for neural network is artificial neuron.

Using this Multi-layer perceptron algorithm, taking the designed feature set as input, both the normal and anomaly classes are predicted. 10 fold cross validation results are given below. Total number of instances is 35913. Number of correctly classified instances is 35263 (98.19%). Number of incorrectly classified instances is 650 (1.80%).

Table 6.2 Performance Gain of multilayer perceptron classifier using 10 fold cross validation

TP Rate	FP Rate	Precision	Recall	Class
0.994	0.456	0.986	0.994	Normal
0.543	0.005	0.756	0.543	Anomaly
		Weighted average		
0.981	0.443	0.979	0.981	

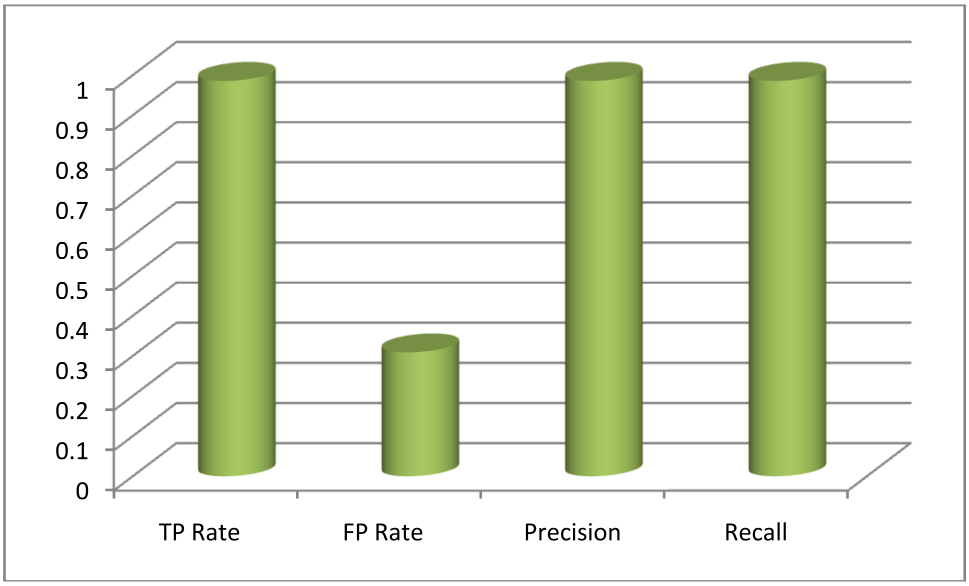

Figure 6.3 Graphical representation of different performance evaluation metrics of classification (weighted average of both the classes) using 10 fold cross validation (MLP)

6.3.4.2 Random Forests Classifier

Random forest is basically a multi-way classifier. Number of trees are associated with this and using some type of randomization, each tree grows [209]. Randomly selecting some subset of training data this classifier generates a number of decision trees. It then gets the decisions from all the decision trees and aggregates to determine the final output or class of the test data [210] [211]. Here for the classification purpose the Random Forest classifier has been used. Using this Random forest classifier algorithm, taking the designed feature set as input, both the normal and anomaly classes are predicted. 10 fold cross validation results are given below. Total number of instances is 35913. Number of correctly classified instances is 35436 (98.67%). Number of incorrectly classified instances is 477 (1.33%).

Table 6.3 Performance Gain of Random forest classifier using 10 fold cross validation

TP Rate	FP Rate	Precision	Recall	Class
0.995	0.318	0.991	0.995	Normal
0.681	0.004	0.825	0.681	Anomaly
		Weighted average		
0.986	0.309	0.986	0.986	

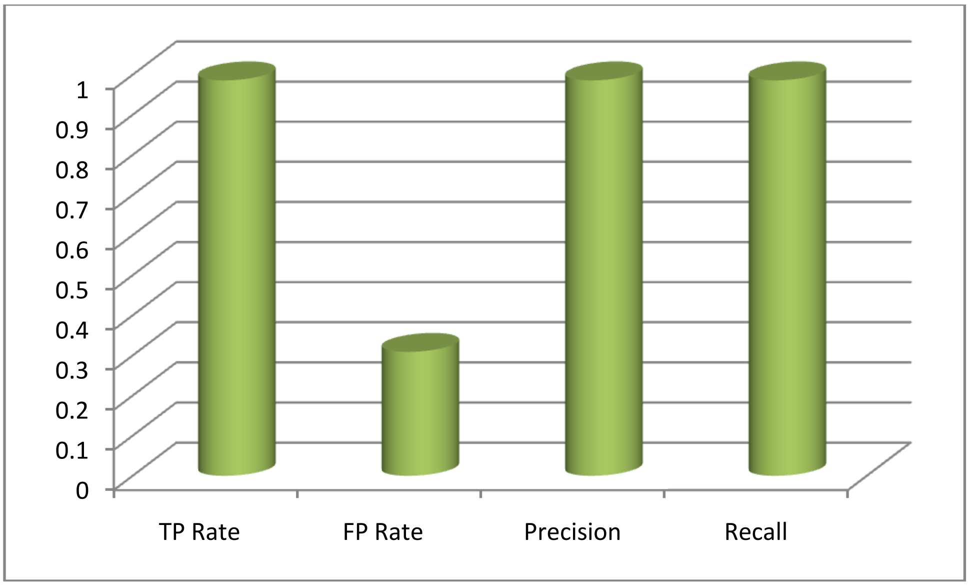

Figure 6.4 Graphical representation of different evaluation metrics of classification (weighted average of both the classes) using 10 fold cross validation (Random forest)

6.4 Comparative Analysis

In this present work, the abnormal and normal regions of the cerebrovascular structure are classified. This classification puts light on the comparative analysis of cerebrovascular structures with and without aneurysm and hemodynamics therein.

A turbulent nature occurs in the flow for the phantom with aneurysm which differs from the flow in the phantom having no aneurysm. These results are very useful for extracting features from the analysis of blood flows through cerebral vasculature with and without aneurysm. These computational studies on digital flows on phantom with and without aneurysm are novel and important for feature extraction as well as classification.

Classification of anomalous region is performed in human cerebrovascular structure using Random Forest classifier [203]. In the study of structural changes in hippocampal dendritic spines, 2-D digital flow has already been applied successfully [162]. Here in this present study 3-D digital flow based model has been used. Here two different classifiers have been used to detect the anomalous and normal region of the cerebrovasculature. The comparisons of different classifiers are stated below:

Table 6.4 Comparisons of different classifiers

Classifier	Correctly Classified Instances	Accuracy
Multilayer Perceptron	35263	98.19 %
Random Forest Classifier	35436	98.67 %

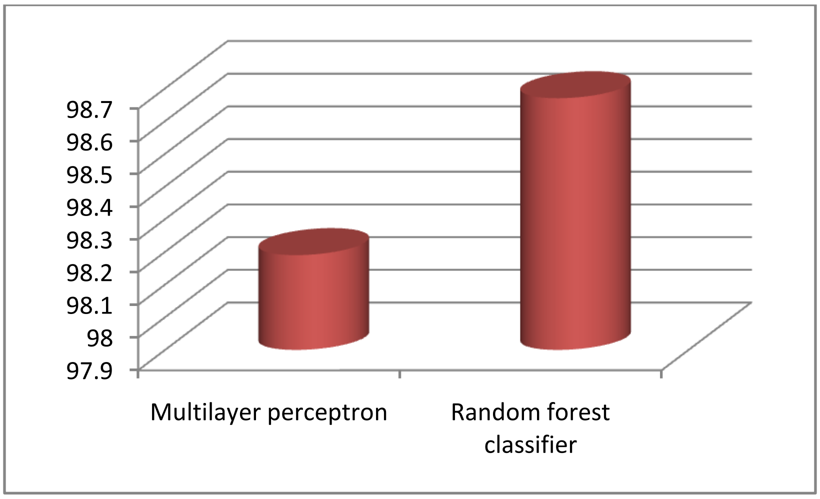

Figure 6.5 Graphical representation of accuracy of different classifier

Table 6.5 Comparisons of different performance metrics of different classifiers

Classifier	TP Rate	FP Rate	Precision	Recall
Multilayer Perceptron	0.981	0.443	0.979	0.981
Random Forest Classifier	0.986	0.309	0.986	0.986

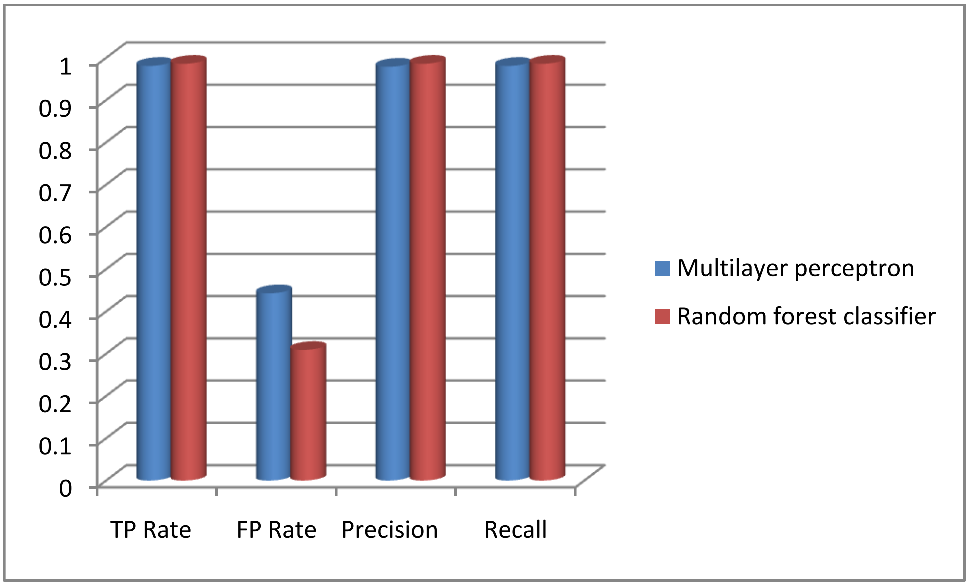

Figure 6.6 Graphical representation of different performance evaluator metrics of different classifiers

6.5 Discussion

By the comparison of different performance evaluator metrics of different classifiers Random forest classifier is performing better for the designed feature set. The maximum classification accuracy which is performed by Random forest classifier is 98.67%. The work presented here may be used in the future work on the digital flow (3-D) based hemodynamic analysis of patients' CTA images with diverse anomalous signature. It also can be applied on complex mathematical phantoms.

Chapter 7

Conclusion

Overall this thesis takes steps towards developing hemodynamic models of human cerebrovascular structure. Detection of anomalous region in vascular structure is one of the vital job for the medical practitioners for further investigation and treatment. So in the present thesis, the ultimate goal is to detect the anomalous region in human cerebrovascular structure, and for that, different features are extracted from the study of the flow analysis on the cerebrovascular phantoms as well as segmented arterial structure with and without aneurysm. The hemodynamic parameter models have been done through the novel digital flow based model and some features are extracted from the conventional CFD based flow analysis.

As the real medical data collections are so troublesome and patient permission is also needed, the real data are not only chosen, but also some phantom data are prepared to study the hemodynamic parameters thoroughly. The detailed need of phantom design is discussed in the introductory chapter of this thesis. Here aneurysm is considered as a vascular disease as it is a very deadly disease to be taken care of. The importance and the reason of this cerebrovascular disease are already discussed briefly in introduction part of this thesis. As the hemodynamics plays an important role in the progression and genesis of aneurysm, hemodynamics of cerebrovasculature is studied on different cerebrovascular structure with and without aneurysm.

Here digital flow has been generated to resemble the blood flow in vascular structure. Digital topology has been used for the studies related to this [212][109]. Using the digital flow based model different hemodynamic parameters like velocity, WSS have been generated and from those hemodynamic parameter and some flow based parameter the feature set has been designed which has been used to classify the anomalous region and normal region of the cerebrovascular structure.

Brain is considered as the most significant and essential part of human body and carotid vascular region is one of the major arterial structures of the same, carotid vasculature and blood flow in the same are considered throughout the thesis.

Multiple tubular structures with varying diameters are combined using piece-wise cubic Bèzier Curves to generate the complete arterial phantom, around the Circle of Willis which is presented at the base of the brain. A basic framework for the design of vascular phantoms, compatible with a custom built user interface is developed in this present work.

Another targeted goal which is achieved, is the segmentation of vasculature from soft bones in the overlapping intensity area. It also targeted towards reducing the number of user interaction in the segmentation process. This work has adopted FDT-based geodesic path propagation approach, and it successfully over performed the pervious approaches made by Saha et al. [151] and other research groups.

The thesis introduces the theory and algorithm of 3-D digital flow and modeled some hemodynamic parameters, a digital flow velocity model is introduced to make the flow closer to real blood flow scenario. The novelty of this work is in the concept of 3-D digital flow and flow velocity model for quick analysis of underlying vascular geometry and establish a relationship between important hemodynamic properties and vascular geometry. Different hemodynamic models are developed using digital flow. CFD based flow analysis is also applied to these cerebrovascular structures with and without aneurysm. Qualitative comparisons of CFD based hemodynamic parameters in human cerebrovascular structure with and without aneurysm are also performed.

In this present work the abnormal and normal regions of the cerebrovascular structure are predicted. This classification emphasized on the comparison of cerebrovascular phantom with and without aneurysm and hemodynamics therein.

After getting the result of flow analysis of the phantom with aneurysm it is found that there is a turbulent signature in the flow which differs from the flow in the phantom without aneurysm. These results are useful for extracting feature from understanding of fluid flows through cerebral vasculature with and without aneurysm. These computational studies of digital flows on phantom with and without aneurysm are novel and important for feature extraction as well as classification. Different classifiers have been used to classify the anomalous region and normal region of the cerebrovascular structure. After applying the different classifiers on selected feature set, the performances are analyzed and compared. Maximum classification accuracy of the present work is 98.67%.

Overall the key contribution of the work presented can be precisely summarized as follows: (i) generation of synthetic structure or phantoms of human cerebrovasculature; (ii) segmentation of carotid arterial structure from real CT angiography image; (iii) Digital flow is developed to simulate hypothetical fluid flow through the phantom and real segmented 3-D structures; (iv) hemodynamic parameter models are developed and analyzed using the concept of digital flow. CFD based flow analysis is also done on some cerebrovascular structure with and without aneurysm; (v) Anomalous regions of the carotid arterial structure are detected.

As future direction of the present work, it can be stated that the present work only deals with CTA images which can be redesigned to deal with other imaging modalities. The work is focused on human cerebrovasculature; it can work with other vascular structures also in future. Flow analysis in digital phantoms is also useful in various other neuro-imaging applications. Flow analysis can be performed on reconstructed digital phantom of hippocampal dendritic spines to analyze it in better way.

References

[1] G. Redekop, K. TerBrugge, W. Montanera, and R. Willinsky, “Arterial aneurysms associated with cerebral arteriovenous malformations: classification, incidence, and risk of hemorrhage,” *J. Neurosurg.*, vol. 89, no. 4, pp. 539–546, 1998.

[2] G. J. Siegel, *Basic neurochemistry: molecular, cellular and medical aspects*, no. V360 SIEb. 1999.

[3] G. P. Xuereb, M. M. L. Prichard, and P. M. Daniel, “The arterial supply and venous drainage of the human hypophysis cerebri,” *Exp. Physiol.*, vol. 39, no. 3, pp. 199–217, 1954.

[4] E. Scharrer, “The blood vessels of the nervous tissue,” *Q. Rev. Biol.*, vol. 19, no. 4, pp. 308–318, 1944.

[5] G. Belcaro and A. N. Nicolaides, *Noninvasive investigations in vascular disease*. World Scientific, 2000.

[6] O. Tanweer, T. A. Wilson, E. Metaxa, H. A. Riina, and H. Meng, “A comparative review of the hemodynamics and pathogenesis of cerebral and abdominal aortic aneurysms: lessons to learn from each other,” *J. Cerebrovasc. Endovasc. Neurosurg.*, vol. 16, no. 4, pp. 335–349, 2014.

[7] D. M. Sawyer, P. S. Amenta, R. Medel, and A. S. Dumont, “Inflammatory mediators in vascular disease: identifying promising targets for intracranial aneurysm research,” *Mediators Inflamm.*, vol. 2015, 2015.

[8] R. Fried and J. Grimaldi, “The Circulatory System and the Heart,” in *The Psychology and Physiology of Breathing*, Springer, 1993, pp. 57–86.

[9] M. Zamir and E. L. Ritman, *The physics of pulsatile flow*. Springer, 2000.

[10] K. Comai, D. L. Feldman, A. L. Goldstein, and J. G. Hamilton, “Atherosclerosis: an overview,” *Drug Dev. Res.*, vol. 6, no. 2, pp. 113–125, 1985.

[11] A. M. Malek, S. L. Alper, and S. Izumo, “Hemodynamic shear stress and its role in atherosclerosis,” *Jama*, vol. 282, no. 21, pp. 2035–2042, 1999.

[12] T. Hashimoto, H. Meng, and W. L. Young, “Intracranial aneurysms: links among inflammation, hemodynamics and vascular remodeling,” *Neurol. Res.*, vol. 28, no. 4, pp. 372–380, 2006.

[13] J. Lynch and G. D. Smith, “A life course approach to chronic disease epidemiology,” *Annu. Rev. Public Heal.*, vol. 26, pp. 1–35, 2005.

[14] B. K. Bharadvaj, R. F. Mabon, and D. P. Giddens, “Steady flow in a model of the human carotid bifurcation. Part I—flow visualization,” *J. Biomech.*, vol. 15, no. 5, pp. 349–362, 1982.

[15] J.-J. Chiu, S. Usami, and S. Chien, “Vascular endothelial responses to altered shear stress: pathologic implications for atherosclerosis,” *Ann. Med.*, vol. 41, no. 1, pp. 19–28, 2009.

[16] M. R. Kaazempur-Mofrad, A. G. Isasi, H. F. Younis, R. C. Chan, D. P. Hinton, G. Sukhova, G. M. LaMuraglia, R. T. Lee, and R. D. Kamm, “Characterization of the atherosclerotic carotid bifurcation using MRI, finite element modeling, and histology,” *Ann. Biomed. Eng.*, vol. 32, no. 7, pp. 932–946, 2004.

[17] D. L. Fry, “Acute vascular endothelial changes associated with increased blood velocity gradients,” *Circ. Res.*, vol. 22, no. 2, pp. 165–197, 1968.

[18] C. M. Schirmer and A. M. Malek, “Wall shear stress gradient analysis within an idealized stenosis using non-Newtonian flow,” *Neurosurgery*, vol. 61, no. 4, pp. 853–864, 2007.

[19] D. G. Potts, *Aneurysms and arteriovenous anomalies of the brain: diagnosis and treatment*. Hoeber Medical Division, Harper & Row, 1965.

[20] O. K. Baskurt and H. J. Meiselman, "Blood rheology and hemodynamics," in *Seminars in thrombosis and hemostasis,* 2003, vol. 29, no. 5, pp. 435–450.

[21] D. A. Steinman, "Image-based computational fluid dynamics modeling in realistic arterial geometries," *Ann. Biomed. Eng.*, vol. 30, no. 4, pp. 483–497, 2002.

[22] S. P. Herbert and D. Y. R. Stainier, "Molecular control of endothelial cell behaviour during blood vessel morphogenesis," *Nat. Rev. Mol. cell Biol.*, vol. 12, no. 9, p. 551, 2011.

[23] R. M. Nerem, "Vascular fluid mechanics, the arterial wall, and atherosclerosis," *J. Biomech. Eng.*, vol. 114, no. 3, pp. 274–282, 1992.

[24] D. B. Cines, E. S. Pollak, C. A. Buck, J. Loscalzo, G. A. Zimmerman, R. P. McEver, J. S. Pober, T. M. Wick, B. A. Konkle, and B. S. Schwartz, "Endothelial cells in physiology and in the pathophysiology of vascular disorders," *Blood,* vol. 91, no. 10, pp. 3527–3561, 1998.

[25] B. K. Lee, H. M. Kwon, B. K. Hong, B. E. Park, S. H. Suh, M. T. Cho, C. S. Lee, M. C. Kim, C. J. Kim, and S. S. Yoo, "Hemodynamic effects on atherosclerosis-prone coronary artery: wall shear stress/rate distribution and impedance phase angle in coronary and aortic circulation," *Yonsei Med. J.*, vol. 42, no. 4, pp. 375–383, 2001.

[26] C. F. Buchanan, S. S. Verbridge, P. P. Vlachos, and M. N. Rylander, "Flow shear stress regulates endothelial barrier function and expression of angiogenic factors in a 3D microfluidic tumor vascular model," *Cell Adh. Migr.*, vol. 8, no. 5, pp. 517–524, 2014.

[27] K. N. Dahl, A. Kalinowski, and K. Pekkan, "Mechanobiology and the microcirculation: cellular, nuclear and fluid mechanics," *Microcirculation,* vol. 17, no. 3, pp. 179–191, 2010.

[28] E. Shaik, "Numerical simulations of blood flow in arteries using fluid-structure interactions." Wichita State University, 2007.

[29] D. Katritsis, L. Kaiktsis, A. Chaniotis, J. Pantos, E. P. Efstathopoulos, and V. Marmarelis, "Wall shear stress: theoretical considerations and methods of measurement," *Prog. Cardiovasc. Dis.*, vol. 49, no. 5, pp. 307–329, 2007.

[30] K. B. Chandran, S. E. Rittgers, and A. P. Yoganathan, *Biofluid mechanics: the human circulation*. CRC press, 2012.

[31] C. A. Taylor, T. J. R. Hughes, and C. K. Zarins, "Finite element modeling of blood flow in arteries," *Comput. Methods Appl. Mech. Eng.*, vol. 158, no. 1–2, pp. 155–196, 1998.

[32] N. A. Lassen and M. S. Christensen, "Physiology of cerebral blood flow," *BJA Br. J. Anaesth.*, vol. 48, no. 8, pp. 719–734, 1976.

[33] C. S. Sinnatamby, *Last's Anatomy e-Book: Regional and Applied*. Elsevier Health Sciences, 2011.

[34] I. M. S. Wilkinson and R. W. R. Russell, "Arteries of the head and neck in giant cell arteritis: a pathological study to show the pattern of arterial involvement," *Arch. Neurol.*, vol. 27, no. 5, pp. 378–391, 1972.

[35] R. Hunt, "THE ROLE OF THE CAROTID ARTERIES, IN THE CAUSATION OF VASCULAR LESIONS OF THE BRAIN, WITH REMARKS ON CERTAIN SPECIAL FEATURES OF THE SYMPTOMATOLOGY. 1," *Am. J. Med. Sci.*, vol. 147, no. 5, p. 704, 1914.

[36] M. Freiman, L. Joskowicz, N. Broide, M. Natanzon, E. Nammer, O. Shilon, L. Weizman, and J. Sosna, “Carotid vasculature modeling from patient CT angiography studies for interventional procedures simulation,” *Int. J. Comput. Assist. Radiol. Surg.*, vol. 7, no. 5, pp. 799–812, 2012.

[37] H. M. Duvernoy, *The human brain: surface, three-dimensional sectional anatomy with MRI, and blood supply*. Springer Science & Business Media, 2012.

[38] D. Perlmutter and A. L. Rhoton Jr, “Microsurgical anatomy of the distal anterior cerebral artery,” *J. Neurosurg.*, vol. 49, no. 2, pp. 204–228, 1978.

[39] Z. C. Akar, M. Dujovny, K. V Slavin, E. Gomez-Tortosa, and J. I. Ausman, “Microsurgical anatomy of the intracranial part of the vertebral artery,” *Neurol. Res.*, vol. 16, no. 3, pp. 171–180, 1994.

[40] A. Kadar and T. Glasz, “Development of atherosclerosis and plaque biology,” *Cardiovasc. Surg.*, vol. 9, no. 2, pp. 109–121, 2001.

[41] U. Morbiducci, A. M. Kok, B. R. Kwak, P. H. Stone, D. A. Steinman, and J. J. Wentzel, “Atherosclerosis at arterial bifurcations: evidence for the role of haemodynamics and geometry,” *Thromb Haemost*, vol. 115, no. 3, pp. 484–492, 2016.

[42] A. J. Brown, Z. Teng, P. C. Evans, J. H. Gillard, H. Samady, and M. R. Bennett, “Role of biomechanical forces in the natural history of coronary atherosclerosis,” *Nat. Rev. Cardiol.*, vol. 13, no. 4, p. 210, 2016.

[43] R. W. Hobson, S. Wilson, and F. J. Veith, *Vascular surgery: principles and practice*. CRC Press, 2003.

[44] W. E. Stehbens, “The pathogenesis of atherosclerosis: a critical evaluation of the evidence,” *Cardiovasc. Pathol.*, vol. 6, no. 3, pp. 123–153, 1997.

[45] J. Suzuki and H. Ohara, “Clinicopathological study of cerebral aneurysms: origin, rupture, repair, and growth,” *J. Neurosurg.*, vol. 48, no. 4, pp. 505–514, 1978.

[46] J. L. Brisman, “Neurosurgery for Cerebral Aneurysm. Medscape.” 2012.

[47] L. N. Sekhar and R. C. Heros, “Origin, growth, and rupture of saccular aneurysms: a review,” *Neurosurgery*, vol. 8, no. 2, pp. 248–260, 1981.

[48] M. R. Crompton, “Mechanism of growth and rupture in cerebral berry aneurysms,” *Br. Med. J.*, vol. 1, no. 5496, p. 1138, 1966.

[49] K. Y. Volokh and D. A. Vorp, “A model of growth and rupture of abdominal aortic aneurysm,” *J. Biomech.*, vol. 41, no. 5, pp. 1015–1021, 2008.

[50] T. Hassan, E. V Timofeev, T. Saito, H. Shimizu, M. Ezura, Y. Matsumoto, K. Takayama, T. Tominaga, and A. Takahashi, “A proposed parent vessel geometry—based categorization of saccular intracranial aneurysms: computational flow dynamics analysis of the risk factors for lesion rupture,” *J. Neurosurg.*, vol. 103, no. 4, pp. 662–680, 2005.

[51] G. G. Ferguson, “Physical factors in the initiation, growth, and rupture of human intracranial saccular aneurysms,” *J. Neurosurg.*, vol. 37, no. 6, pp. 666–677, 1972.

[52] S. Juvela, “Natural history of unruptured intracranial aneurysms: risks for aneurysm formation, growth, and rupture,” in *New Trends in Cerebral Aneurysm Management*, Springer, 2002, pp. 27–30.

[53] R. Muthupillai, D. J. Lomas, P. J. Rossman, J. F. Greenleaf, A. Manduca, and R. L. Ehman, “Magnetic resonance elastography by direct visualization of propagating acoustic strain waves,” *Science (80-.).*, vol. 269, no. 5232, pp. 1854–1857, 1995.

[54] J. Kramer and M. P. Recht, “MR arthrography of the lower extremity,” *Radiol. Clin. North Am.*, vol. 40, no. 5, pp. 1121–1132, 2002.

[55] D. N. Mintz, T. Hooper, D. Connell, R. Buly, D. E. Padgett, and H. G. Potter, "Magnetic resonance imaging of the hip: detection of labral and chondral abnormalities using noncontrast imaging," *Arthroscopy*, vol. 21, no. 4, pp. 385–393, 2005.

[56] K. S. Rakhra, "Magnetic resonance imaging of acetabular labral tears," *JBJS*, vol. 93, no. Supplement_2, pp. 28–34, 2011.

[57] W. R. Hendee and E. R. Ritenour, *Medical imaging physics*. John Wiley & Sons, 2003.

[58] T. O. Smith, G. Hilton, A. P. Toms, S. T. Donell, and C. B. Hing, "The diagnostic accuracy of acetabular labral tears using magnetic resonance imaging and magnetic resonance arthrography: a meta-analysis," *Eur. Radiol.*, vol. 21, no. 4, pp. 863–874, 2011.

[59] Y.-S. Chan, L.-C. Lien, H.-L. Hsu, Y.-L. Wan, M. S. S. Lee, K.-Y. Hsu, and C.-H. Shih, "Evaluating hip labral tears using magnetic resonance arthrography: a prospective study comparing hip arthroscopy and magnetic resonance arthrography diagnosis," *Arthroscopy*, vol. 21, no. 10, pp. 1250-e1, 2005.

[60] C. Czerny, S. Hofmann, M. Urban, C. Tschauner, A. Neuhold, M. Pretterklieber, M. P. Recht, and J. Kramer, "MR arthrography of the adult acetabular capsular-labral complex: correlation with surgery and anatomy.," *AJR. Am. J. Roentgenol.*, vol. 173, no. 2, pp. 345–349, 1999.

[61] C. A. Petersilge, M. A. Haque, W. J. Petersilge, J. S. Lewin, J. M. Lieberman, and R. Buly, "Acetabular labral tears: evaluation with MR arthrography.," *Radiology*, vol. 200, no. 1, pp. 231–235, 1996.

[62] G. A. Toomayan, W. R. Holman, N. M. Major, S. M. Kozlowicz, and T. P. Vail, "Sensitivity of MR arthrography in the evaluation of acetabular labral tears," *Am. J. Roentgenol.*, vol. 186, no. 2, pp. 449–453, 2006.

[63] C. B. Scruby and L. E. Drain, *Laser ultrasonics techniques and applications*. CRC Press, 1990.

[64] A. A. Vives, *Piezoelectric transducers and applications*. Springer Science & Business Media, 2008.

[65] J. C. Bamber, "Ultrasonic properties of tissues," *Ultrasound Med.*, pp. 57–88, 1998.

[66] T. L. Szabo, *Diagnostic ultrasound imaging: inside out*. Academic Press, 2004.

[67] S. Vitek and K. Vortman, "Focused ultrasound system for surrounding a body tissue mass and treatment method." Google Patents, 02-Apr-2013.

[68] M. Marinoni, S. Trapani, T. Atzori, S. D'Onofrio, and A. Cramaro, "Muscle Ultrasound evaluation: Physical principles, standard procedures, advanced technologies and practical advice," 2016.

[69] P. Geladi and H. F. Grahn, *Multivariate image analysis*. Wiley Online Library, 1996.

[70] J. A. Noble and D. Boukerroui, "Ultrasound image segmentation: a survey," *IEEE Trans. Med. Imaging*, vol. 25, no. 8, pp. 987–1010, 2006.

[71] G. E. Nilsson, T. Tenland, and P. A. Oberg, "Evaluation of a laser Doppler flowmeter for measurement of tissue blood flow," *IEEE Trans. Biomed. Eng.*, no. 10, pp. 597–604, 1980.

[72] R. M. Rangayyan, *Biomedical image analysis*. CRC press, 2004.

[73] R. A. Robb, E. A. Hoffman, L. J. Sinak, L. D. Harris, and E. L. Ritman, "High-speed three-dimensional x-ray computed tomography: The dynamic spatial reconstructor," *Proc. IEEE*, vol. 71, no. 3, pp. 308–319, 1983.

[74] D. J. Heuscher, W. W. Lindstrom, and H. K. Tuy, “Multiple detector ring spiral scanner with relatively adjustable helical paths.” Google Patents, 16-Jan-1996.

[75] H. Nishimura and O. Miyazaki, “CT system for spirally scanning subject on a movable bed synchronized to x-ray tube revolution.” Google Patents, 06-Dec-1988.

[76] S. Ulzheimer and T. Flohr, “Multislice CT: current technology and future developments,” in *Multislice CT*, Springer, 2009, pp. 3–23.

[77] R. A. Ketcham and W. D. Carlson, “Acquisition, optimization and interpretation of X-ray computed tomographic imagery: applications to the geosciences,” *Comput. Geosci.*, vol. 27, no. 4, pp. 381–400, 2001.

[78] T. G. Flohr, S. Schaller, K. Stierstorfer, H. Bruder, B. M. Ohnesorge, and U. J. Schoepf, “Multi–detector row CT systems and image-reconstruction techniques,” *Radiology*, vol. 235, no. 3, pp. 756–773, 2005.

[79] J. A. Knottnerus, C. van Weel, and J. W. M. Muris, “Evidence base of clinical diagnosis: evaluation of diagnostic procedures,” *BMJ Br. Med. J.*, vol. 324, no. 7335, p. 477, 2002.

[80] M. M. Jawaid, “Detection, localization and quantification of non-calcified coronary plaques in contrast enhanced CT angiography.” City, University of London, 2017.

[81] M. Fisher, “Occlusion of the internal carotid artery,” *AMA Arch. Neurol. Psychiatry*, vol. 65, no. 3, pp. 346–377, 1951.

[82] J. Mackay, G. A. Mensah, and K. Greenlund, *The atlas of heart disease and stroke*. World Health Organization, 2004.

[83] D. Lloyd-Jones, R. Adams, M. Carnethon, G. De Simone, T. B. Ferguson, K. Flegal, E. Ford, K. Furie, A. Go, and K. Greenlund, “Heart disease and stroke statistics—2009 update: a report from the American Heart Association Statistics Committee and Stroke Statistics Subcommittee,” *Circulation*, vol. 119, no. 3, pp. e21–e181, 2009.

[84] D. J. Gilski and B. Borkenhagen, “Risk evaluation in action for cardiovascular health,” *Crit. Care Nurse*, vol. 25, no. 1, pp. 26–37, 2005.

[85] M. Bathe and R. D. Kamm, “A fluid-structure interaction finite element analysis of pulsatile blood flow through a compliant stenotic artery,” *J. Biomech. Eng.*, vol. 121, no. 4, pp. 361–369, 1999.

[86] P. D. Stein and H. N. Sabbah, “Turbulent blood flow in the ascending aorta of humans with normal and diseased aortic valves.,” *Circ. Res.*, vol. 39, no. 1, pp. 58–65, 1976.

[87] R. N. Jorge, J. M. R. S. Tavares, M. P. Barbosa, and A. P. Slade, *Technologies for medical sciences*. Springer, 2012.

[88] C. A. Taylor and D. A. Steinman, “Image-based modeling of blood flow and vessel wall dynamics: applications, methods and future directions,” *Ann. Biomed. Eng.*, vol. 38, no. 3, pp. 1188–1203, 2010.

[89] M. R. De Leval, G. Dubini, H. Jalali, and R. Pietrabissa, “Use of computational fluid dynamics in the design of surgical procedures: application to the study of competitive flows in cavopulmonary connections,” *J. Thorac. Cardiovasc. Surg.*, vol. 111, no. 3, pp. 502–513, 1996.

[90] C. Hirsch, *Numerical computation of internal and external flows: The fundamentals of computational fluid dynamics*. Elsevier, 2007.

[91] C. Karmonik, J. Bismuth, D. J. Shah, M. G. Davies, D. Purdy, and A. B. Lumsden, "Computational study of haemodynamic effects of entry-and exit-tear coverage in a DeBakey type III aortic dissection: technical report," *Eur. J. Vasc. Endovasc. Surg.*, vol. 42, no. 2, pp. 172–177, 2011.

[92] Y.-C. Fung, "Biomechanics: circulation," *Shock*, vol. 9, no. 2, p. 155, 1998.

[93] K. Pekkan, D. De Zélicourt, L. Ge, F. Sotiropoulos, D. Frakes, M. A. Fogel, and A. P. Yoganathan, "Physics-driven CFD modeling of complex anatomical cardiovascular flows—a TCPC case study," *Ann. Biomed. Eng.*, vol. 33, no. 3, pp. 284–300, 2005.

[94] Q. Long, X. Y. Xu, B. Ariff, S. A. Thom, A. D. Hughes, and A. V Stanton, "Reconstruction of blood flow patterns in a human carotid bifurcation: a combined CFD and MRI study," *J. Magn. Reson. Imaging*, vol. 11, no. 3, pp. 299–311, 2000.

[95] "ANSYS - Simulation Driven Product Development." .

[96] J. Zhang, J. G. Fletcher, T. J. Vrtiska, A. Manduca, J. L. Thompson, M. L. Raghavan, R. J. Wentz, and C. H. McCollough, "Large-vessel distensibility measurement with electrocardiographically gated multidetector CT: phantom study and initial experience," *Radiology*, vol. 245, no. 1, pp. 258–266, 2007.

[97] H. H. G. Hansen, R. G. P. Lopata, and C. L. de Korte, "Noninvasive carotid strain imaging using angular compounding at large beam steered angles: validation in vessel phantoms," *IEEE Trans. Med. Imaging*, vol. 28, no. 6, pp. 872–880, 2009.

[98] M. Piccinelli, A. Veneziani, D. A. Steinman, A. Remuzzi, and L. Antiga, "A framework for geometric analysis of vascular structures: application to cerebral aneurysms," *IEEE Trans. Med. Imaging*, vol. 28, no. 8, pp. 1141–1155, 2009.

[99] L. Antiga, M. Piccinelli, L. Botti, B. Ene-Iordache, A. Remuzzi, and D. A. Steinman, "An image-based modeling framework for patient-specific computational hemodynamics," *Med. Biol. Eng. Comput.*, vol. 46, no. 11, p. 1097, 2008.

[100] P. K. Saha, Z. Gao, S. K. Alford, M. Sonka, and E. A. Hoffman, "Topomorphologic separation of fused isointensity objects via multiscale opening: Separating arteries and veins in 3-D pulmonary CT," *IEEE Trans. Med. Imaging*, vol. 29, no. 3, pp. 840–851, 2010.

[101] S. Basu, M. L. Raghavan, E. A. Hoffman, and P. K. Saha, "Multi-scale opening of conjoined structures with shared intensities: Methods and applications," *Proc. - 2011 Int. Conf. Intell. Comput. Bio-Medical Instrumentation, ICBMI 2011*, pp. 128–131, 2011.

[102] L. Boussel, V. Rayz, C. McCulloch, A. Martin, G. Acevedo-Bolton, M. Lawton, R. Higashida, W. S. Smith, W. L. Young, and D. Saloner, "Aneurysm growth occurs at region of low wall shear stress patient-specific correlation of hemodynamics and growth in a longitudinal study," *Stroke*, vol. 39, no. 11, pp. 2997–3002, 2008.

[103] A. Sarrami-Foroushani, M. N. Esfahany, H. S. Rad, K. Firouznia, M. Shakiba, and H. Ghanaati, "Effects of variations of flow and heart rate on intra-aneurysmal hemodynamics in a ruptured internal carotid artery aneurysm during exercise," *Iran. J. Radiol.*, vol. 13, no. 1, 2016.

[104] S. M. Moore, K. T. Moorhead, J. G. Chase, T. David, and J. Fink, "One-dimensional and three-dimensional models of cerebrovascular flow," *J. Biomech. Eng.*, vol. 127, no. 3, pp. 440–449, 2005.

[105] M. L. Raghavan and D. A. Vorp, “Toward a biomechanical tool to evaluate rupture potential of abdominal aortic aneurysm: identificationof a finite strain constitutivemodel andevaluation of its applicability,” *J. Biomech. no.4,pp. 475–482, 2000*, vol. 33, 2000.

[106] T. Gaziano, K. S. Reddy, F. Paccaud, S. Horton, and V. Chaturvedi, “Cardiovascular disease,” 2006.

[107] C. H. Hennekens, “Increasing burden of cardiovascular disease: current knowledge and future directions for research on risk factors,” *Circulation*, vol. 97, no. 11, pp. 1095–1102, 1998.

[108] A. Vilanova, B. Preim, R. van Pelt, R. Gasteiger, M. Neugebauer, and T. Wischgoll, “Visual exploration of simulated and measured blood flow,” in *Scientific Visualization*, Springer, 2014, pp. 305–324.

[109] P. K. Saha, R. Strand, and G. Borgefors, “Digital topology and geometry in medical imaging: a survey,” *IEEE Trans. Med. Imaging*, vol. 34, no. 9, pp. 1940–1964, 2015.

[110] M. D. Botney, “Role of hemodynamics in pulmonary vascular remodeling: implications for primary pulmonary hypertension,” *Am. J. Respir. Crit. Care Med.*, vol. 159, no. 2, pp. 361–364, 1999.

[111] A. M. Nixon, M. Gunel, and B. E. Sumpio, “The critical role of hemodynamics in the development of cerebral vascular disease: a review,” *J. Neurosurg.*, vol. 112, no. 6, pp. 1240–1253, 2010.

[112] Z. Gao, R. W. Grout, C. Holtze, E. A. Hoffman, and P. Saha, “A new paradigm of interactive artery/vein separation in noncontrast pulmonary CT imaging using multiscale topomorphologic opening,” *IEEE Trans. Biomed. Eng.*, vol. 59, no. 11, pp. 3016–3027, 2012.

[113] C. Wan, G. Jin, J. Wang, X. Li, L. Hao, K. Huang, F. Li, and J. Ren, “Design and development of object-oriented software based on Qt,” *Nucl. Electron. Detect. Technol.*, vol. 24, no. 3, pp. 311–313, 2004.

[114] L. Ibanez, W. Schroeder, L. Ng, and J. Cates, “The ITK software guide,” 2005.

[115] W. J. Schroeder, B. Lorensen, and K. Martin, *The visualization toolkit: an object-oriented approach to 3D graphics*. Kitware, 2004.

[116] W. J. Schroeder, L. S. Avila, and W. Hoffman, “Visualizing with VTK: a tutorial,” *IEEE Comput. Graph. Appl.*, vol. 20, no. 5, pp. 20–27, 2000.

[117] P. Yushkevich, G. Gerig, O. Soldea, and Y. Gao, “Itk-snap.” Online, 2015.

[118] Z. Cai, E.-W. Bai, R. McCabe, M. Zerhouni, G. Wang, M. Raghavan, and J. Kratzberg, “A Dynamic Arterial Tree Phantom for studies of bolus chasing CT Angiography,” *Int. J. Biomed. Eng. Technol.*, vol. 4, no. 1, pp. 88–100, 2010.

[119] B. He, Y. Du, X. Song, W. P. Segars, and E. C. Frey, “A Monte Carlo and physical phantom evaluation of quantitative In-111 SPECT,” *Phys. Med. Biol.*, vol. 50, no. 17, p. 4169, 2005.

[120] D. L. Collins, A. P. Zijdenbos, V. Kollokian, J. G. Sled, N. J. Kabani, C. J. Holmes, and A. C. Evans, “Design and construction of a realistic digital brain phantom,” *IEEE Trans. Med. Imaging*, vol. 17, no. 3, pp. 463–468, 1998.

[121] R. P. Wood, P. Khobragade, L. Ying, K. Snyder, D. Wack, D. R. Bednarek, S. Rudin, and C. N. Ionita, “Initial testing of a 3D printed perfusion phantom using digital subtraction angiography,” in *Proceedings of SPIE--the International Society for Optical Engineering*, 2015, vol. 9417.

[122] E. R. Melhem, J.-M. Serfaty, L. Jones, R. Itoh, B. S. Kuszyk, J.-B. Martin, P. Gailloud, K. P. J. Murphy, and D. A. Rufenacht, “Contrast-enhanced MR angiography: the effects of k-space truncation on luminal representation in a carotid artery phantom model,” *Am. J. Neuroradiol.*, vol. 21, no. 6, pp. 1028–1031, 2000.

[123] G. Cloutier, G. Soulez, S. D. Qanadli, P. Teppaz, L. Allard, Z. Qin, F. Cloutier, and L. Durand, “A multimodality vascular imaging phantom with fiducial markers visible in DSA, CTA, MRA, and ultrasound,” *Med. Phys.*, vol. 31, no. 6, pp. 1424–1433, 2004.

[124] S. Basu, M. L. Raghavan, E. A. Hoffman, and P. K. Saha, “Multi-scale opening of conjoined structures with shared intensities: Methods and applications,” in *Intelligent Computation and Bio-Medical Instrumentation (ICBMI), 2011 International Conference on*, 2011, pp. 128–131.

[125] S. Le Floc’h, G. Cloutier, G. Finet, P. Tracqui, R. I. Pettigrew, and J. Ohayon, “On the potential of a new IVUS elasticity modulus imaging approach for detecting vulnerable atherosclerotic coronary plaques: in vitro vessel phantom study,” *Phys. Med. Biol.*, vol. 55, no. 19, p. 5701, 2010.

[126] G. De Santis, M. De Beule, K. Van Canneyt, P. Segers, P. Verdonck, and B. Verhegghe, “Full-hexahedral structured meshing for image-based computational vascular modeling,” *Med. Eng. Phys.*, vol. 33, no. 10, pp. 1318–1325, 2011.

[127] H. Zhu, Z. Ding, R. N. Piana, T. R. Gehrig, and M. H. Friedman, “Cataloguing the geometry of the human coronary arteries: a potential tool for predicting risk of coronary artery disease,” *Int. J. Cardiol.*, vol. 135, no. 1, pp. 43–52, 2009.

[128] S. M. Zabihi, H. R. Pourreza, and T. Banaee, “Vessel extraction of conjunctival images using LBPs and ANFIS,” *ISRN Mach. Vis.*, vol. 2012, 2011.

[129] H. Bogunović, J. M. Pozo, R. Cárdenes, M. C. Villa-Uriol, R. Blanc, M. Piotin, and A. F. Frangi, “Automated landmarking and geometric characterization of the carotid siphon,” *Med. Image Anal.*, vol. 16, no. 4, pp. 889–903, 2012.

[130] P. A. Yushkevich, J. Piven, H. C. Hazlett, R. G. Smith, S. Ho, J. C. Gee, and G. Gerig, “User-guided 3D active contour segmentation of anatomical structures: significantly improved efficiency and reliability,” *Neuroimage*, vol. 31, no. 3, pp. 1116–1128, 2006.

[131] R. Hasbun, J. Abrahams, J. Jekel, and V. J. Quagliarello, “Computed tomography of the head before lumbar puncture in adults with suspected meningitis,” *N. Engl. J. Med.*, vol. 345, no. 24, pp. 1727–1733, 2001.

[132] T. Beyer, D. W. Townsend, and T. M. Blodgett, “Dual-modality PET/CT tomography for clinical oncology,” *Q. J. Nucl. Med. Mol. Imaging*, vol. 46, no. 1, p. 24, 2002.

[133] L. Antiga and D. A. Steinman, “VMTK: vascular modeling toolkit,” *URL http//www. vmtk. org*, 2006.

[134] S. Basu, E. Hoffman, and P. K. Saha, “Multi-scale Opening–A New Morphological Operator,” in *International Conference on Image Analysis and Processing*, 2015, pp. 417–427.

[135] A. Banerjee, S. Dey, S. Parui, M. Nasipuri, and S. Basu, “Design of 3-D Phantoms for Human Carotid Vasculature,” in *Advances in Computing and Communications (ICACC), 2013 Third International Conference on*, 2013, pp. 347–350.

[136] Y. Xu, P. K. Saha, G. Hu, G. Liang, Y. Yang, and J. Geng, “Quantification of stenosis in coronary artery via CTA using fuzzy distance transform,” in *Medical Imaging 2009: Biomedical Applications in Molecular, Structural, and Functional Imaging*, 2009, vol. 7262, p. 72620K.

[137] S. Svensson, “A decomposition scheme for 3D fuzzy objects based on fuzzy distance information,” *Pattern Recognit. Lett.*, vol. 28, no. 2, pp. 224–232, 2007.

[138] B. Aubert-Broche, M. Griffin, G. B. Pike, A. C. Evans, and D. L. Collins, “Twenty new digital brain phantoms for creation of validation image data bases,” *IEEE Trans. Med. Imaging*, vol. 25, no. 11, pp. 1410–1416, 2006.

[139] I. Guha, N. Das, **P. Rakshit**, M. Nasipuri, and P. K. Saha, “Design of cerebrovascular phantoms using fuzzy distance transform based geodesic paths,” in *4th International Conference on Advanced Computing, Networking, and Informatics [ICACNI - 2016]*, 2016.

[140] I. Guha, N. Das, **P. Rakshit**, M. Nasipuri, P. K. Saha, and S. Basu, “A semiautomatic approach for segmentation of carotid vasculature from patients’ CTA images,” *Innov. Syst. Softw. Eng.*, vol. 13, no. 4, pp. 243–250, 2017.

[141] A. Rosenfeld, “Adjacency in digital pictures,” *Inf. Control*, vol. 26, no. 1, pp. 24–33, 1974.

[142] P. K. Saha and B. B. Chaudhuri, “3D digital topology under binary transformation with applications,” *Comput. Vis. image Underst.*, vol. 63, no. 3, pp. 418–429, 1996.

[143] H. Eggers, “Two fast euclidean distance transformations in z2based on sufficient propagation,” *Comput. Vis. Image Underst.*, vol. 69, no. 1, pp. 106–116, 1998.

[144] G. Borgefors, “On digital distance transforms in three dimensions,” *Comput. Vis. image Underst.*, vol. 64, no. 3, pp. 368–376, 1996.

[145] G. Borgefors, “Distance transformations in arbitrary dimensions,” *Comput. vision, Graph. image Process.*, vol. 27, no. 3, pp. 321–345, 1984.

[146] G. Borgefors, “Distance transformations in digital images,” *Comput. vision, Graph. image Process.*, vol. 34, no. 3, pp. 344–371, 1986.

[147] O. Cuisenaire and B. Macq, “Fast Euclidean distance transformation by propagation using multiple neighborhoods,” *Comput. Vis. Image Underst.*, vol. 76, no. 2, pp. 163–172, 1999.

[148] P.-E. Danielsson, “Euclidean distance mapping,” *Comput. Graph. image Process.*, vol. 14, no. 3, pp. 227–248, 1980.

[149] P. K. Saha, F. W. Wehrli, and B. R. Gomberg, “Fuzzy Distance Transform: Theory, Algorithms, and Applications,” *Comput. Vis. Image Underst.*, vol. 86, no. 3, pp. 171–190, 2002.

[150] A. Rosenfeld, “Geodesics in digital pictures,” *Inf. Control*, vol. 36, no. 1, pp. 74–84, 1978.

[151] P. K. Saha, S. Basu, and E. A. Hoffman, “Multiscale Opening of Conjoined Fuzzy Objects: Theory and Applications,” *IEEE Trans. Fuzzy Syst.*, vol. 24, no. 5, pp. 1121–1133, 2016.

[152] P. K. Saha, J. K. Udupa, and D. Odhner, “Scale-based fuzzy connected image segmentation: theory, algorithms, and validation,” *Comput. Vis. Image Underst.*, vol. 77, no. 2, pp. 145–174, 2000.

[153] A. Rosenfeld and J. L. Pfaltz, “Distance functions on digital pictures,” *Pattern Recognit.*, vol. 1, no. 1, pp. 33–61, Jul. 1968.

[154] A. Rosenfeld and J. L. Pfaltz, “Sequential operations in digital picture processing,” *J. ACM*, vol. 13, no. 4, pp. 471–494, 1966.

[155] U. Montanari, “A method for obtaining skeletons using a quasi-Euclidean distance,” *J. ACM*, vol. 15, no. 4, pp. 600–624, 1968.

[156] J. Hilditch and D. Rutovitz, “Chromosome recognition,” *Ann. N. Y. Acad. Sci.*, vol. 157, no. 1, pp. 339–364, 1969.

[157] C. O. Kiselman, “Regularity properties of distance transformations in image analysis,” *Comput. Vis. Image Underst.*, vol. 64, no. 3, pp. 390–398, 1996.

[158] T. Saito and J.-I. Toriwaki, “New algorithms for euclidean distance transformation of an n-dimensional digitized picture with applications,” *Pattern Recognit.*, vol. 27, no. 11, pp. 1551–1565, 1994.

[159] F. Y. Shih and Y.-T. Wu, “Fast Euclidean distance transformation in two scans using a 3× 3 neighborhood,” *Comput. Vis. Image Underst.*, vol. 93, no. 2, pp. 195–205, 2004.

[160] H. Embrechts and D. Roose, “A parallel Euclidean distance transformation algorithm,” *Comput. Vis. Image Underst.*, vol. 63, no. 1, pp. 15–26, 1996.

[161] P. K. Saha, S. Member, S. Basu, S. Member, and E. A. H. Senior, “Multi-Scale Opening of Conjoined Fuzzy Objects: Theory and Applications,” vol. 6706, no. c, pp. 1–14, 2015.

[162] S. Basu, D. Plewczynski, S. Saha, M. Roszkowska, M. Magnowska, E. Baczynska, and J. Wlodarczyk, “2dSpAn: semiautomated 2-d segmentation, classification and analysis of hippocampal dendritic spine plasticity,” *Bioinformatics*, vol. 32, no. 16, pp. 2490–2498, 2016.

[163] E. S. O. (ESO) E. Committee and E. S. O. W. Committee, “Guidelines for management of ischaemic stroke and transient ischaemic attack 2008,” *Cerebrovasc. Dis.*, vol. 25, no. 5, pp. 457–507, 2008.

[164] J. F. Kurtzke, “An introduction to the epidemiology of cerebrovascular disease,” in *Cerebrovascular disease, tenth Princeton conference. Raven, New York*, 1976, pp. 239–253.

[165] L. C. Brown and J. T. Powell, “Risk factors for aneurysm rupture in patients kept under ultrasound surveillance,” *Ann. Surg.*, vol. 230, no. 3, p. 289, 1999.

[166] J. M. Bamford, P. A. G. Sandercock, M. S. Dennis, J. P. S. Burn, and C. P. Warlow, “A prospective study of acute cerebrovascular disease in the community: the Oxfordshire Community Stroke Project--1981-86. 2. Incidence, case fatality rates and overall outcome at one year of cerebral infarction, primary intracerebral and subarachnoid haemorrhage.,” *J. Neurol. Neurosurg. Psychiatry*, vol. 53, no. 1, pp. 16–22, 1990.

[167] H. Bode and U. Wais, “Age dependence of flow velocities in basal cerebral arteries.,” *Arch. Dis. Child.*, vol. 63, no. 6, pp. 606–611, 1988.

[168] A. F. van Raamt, A. P. A. Appelman, W. P. T. M. Mali, and Y. van der Graaf, “Arterial blood flow to the brain in patients with vascular disease: the SMART Study,” *Radiology*, vol. 240, no. 2, pp. 515–521, 2006.

[169] N. Shahcheraghi, H. A. Dwyer, A. Y. Cheer, A. I. Barakat, and T. Rutaganira, “Unsteady and three-dimensional simulation of blood flow in the human aortic arch,” *J. Biomech. Eng.*, vol. 124, no. 4, pp. 378–387, 2002.

[170] J. Brunette, R. Mongrain, A. Ranga, and J.-C. Tardif, “An Atherosclerotic Coronary Artery Phantom for Particle Image Velocimetry,” *Proc. Can. Eng. Educ. Assoc.*, 2011.

[171] J. H. Halsey, H. A. McDowell, S. Gelmon, and R. B. Morawetz, “Blood velocity in the middle cerebral artery and regional cerebral blood flow during carotid endarterectomy.,” *Stroke*, vol. 20, no. 1, pp. 53–58, 1989.

[172] G. Jungquist, B. Nilsson, H. Ostberg, S. O. Isacsson, L. Janzon, B. Steen, and S. E. Lindell, “Carotid artery blood flow velocity related to transient ischemic attack and stroke in a population study of 69-year-old men.,” *Stroke*, vol. 20, no. 10, pp. 1327–1330, 1989.

[173] W. M. Blackshear, D. J. Phillips, P. M. Chikos, J. D. Harley, B. L. Thiele, and D. E. Strandness, “Carotid artery velocity patterns in normal and stenotic vessels.,” *Stroke*, vol. 11, no. 1, pp. 67–71, 1980.

[174] A. K. Gupta, “Performance and analysis of blood flow through carotid artery,” *Int. J. Eng. Bus. Manag.*, vol. 3, p. 24, 2011.

[175] J. Chen and X.-Y. Lu, “Numerical investigation of the non-Newtonian blood flow in a bifurcation model with a non-planar branch,” *J. Biomech.*, vol. 37, no. 12, pp. 1899–1911, 2004.

[176] J. Lu, C.-W. Liu, and J. S. Thorp, “New methods for computing a saddle-node bifurcation point for voltage stability analysis,” *IEEE Trans. power Syst.*, vol. 10, no. 2, pp. 978–989, 1995.

[177] Z. Lou and W.-J. Yang, “A computer simulation of the non-Newtonian blood flow at the aortic bifurcation,” *J. Biomech.*, vol. 26, no. 1, pp. 37–49, 1993.

[178] S.-W. Lee, L. Antiga, J. D. Spence, and D. A. Steinman, “Geometry of the carotid bifurcation predicts its exposure to disturbed flow,” *Stroke*, vol. 39, no. 8, pp. 2341–2347, 2008.

[179] D. Doorly and S. Sherwin, “Geometry and flow,” *Cardiovasc. Math.*, pp. 177–209, 2009.

[180] F. M. A. Box, R. J. van der Geest, M. C. M. Rutten, and J. H. C. Reiber, “The influence of flow, vessel diameter, and non-newtonian blood viscosity on the wall shear stress in a carotid bifurcation model for unsteady flow,” *Invest. Radiol.*, vol. 40, no. 5, pp. 277–294, 2005.

[181] C. K. Zarins, D. P. Giddens, B. K. Bharadvaj, V. S. Sottiurai, R. F. Mabon, and S. Glagov, “Carotid Bifurcation Atherosclerosis Quantitative Correlation of Plaque Localization with Flow Velocity Profiles and Wall Shear Stress,” pp. 502–515, 1975.

[182] A. Banerjee, S. Dey, S. Parui, M. Nasipuri, and S. Basu, “Synthetic reconstruction of human carotid vasculature using a 2-D/3-D interface,” in *Advances in Computing, Communications and Informatics (ICACCI), 2013 International Conference on*, 2013, pp. 60–65.

[183] D. A. Vorp, M. L. Raghavan, and M. W. Webster, “Mechanical wall stress in abdominal aortic aneurysm: Influence of diameter and asymmetry,” *J. Vasc. Surg.*, vol. 27, no. 4, pp. 632–639, 1998.

[184] M. L. Raghavan, D. A. Vorp, M. P. Federle, M. S. Makaroun, and M. W. Webster, “Wall stress distribution on three-dimensionally reconstructed models of human abdominal aortic aneurysm.,” *J. Vasc. Surg.*, vol. 31, no. 4, pp. 760–9, 2000.

[185] M. F. Fillinger, M. L. Raghavan, S. P. Marra, J. L. Cronenwett, and F. E. Kennedy, “In vivo analysis of mechanical wall stress and abdominal aortic aneurysm rupture risk,” *J. Vasc. Surg.*, vol. 36, no. 3, pp. 589–597, 2002.

[186] C. Julien, Z. Q. Zhang, C. Cerutti, and C. Barrès, “Hemodynamic analysis of arterial pressure oscillations in conscious rats,” *J. Auton. Nerv. Syst.*, vol. 50, no. 3, pp. 239–252, 1995.

[187] M. F. Fillinger, S. P. Marra, M. L. Raghavan, and F. E. Kennedy, “Prediction of rupture risk in abdominal aortic aneurysm during observation: wall stress versus diameter,” *J. Vasc. Surg.*, vol. 37, no. 4, pp. 724–732, 2003.

[188] A. Chien, S. Tateshima, M. Castro, J. Sayre, J. Cebral, and F. Viñuela, “Patient-specific flow analysis of brain aneurysms at a single location: Comparison of hemodynamic characteristics in small aneurysms,” *Med. Biol. Eng. Comput.*, vol. 46, no. 11, pp. 1113–1120, 2008.

[189] B. M. Johnston, P. R. Johnston, S. Corney, and D. Kilpatrick, “Non-Newtonian blood flow in human right coronary arteries: transient simulations,” *J. Biomech.*, vol. 39, no. 6, pp. 1116–1128, 2006.

[190] H. F. Younis, M. R. Kaazempur-Mofrad, R. C. Chan, A. G. Isasi, D. P. Hinton, A. H. Chau, L. A. Kim, and R. D. Kamm, “Hemodynamics and wall mechanics in human carotid bifurcation and its consequences for atherogenesis: investigation of inter-individual variation,” *Biomech. Model. Mechanobiol.*, vol. 3, no. 1, pp. 17–32, 2004.

[191] S. Svensson, “Aspects on the reverse fuzzy distance transform,” *Pattern Recognit. Lett.*, vol. 29, no. 7, pp. 888–896, 2008.

[192] W. J. Vankan, J. M. Huyghe, J. D. Janssen, A. Huson, W. J. G. Hacking, and W. Schreiner, “Finite element analysis of blood flow through biological tissue,” *Int. J. Eng. Sci.*, vol. 35, no. 4, pp. 375–385, 1997.

[193] **P. Rakshit**, N. Das, M. Nasipuri, and S. Basu, “A Qualitative Hemodynamic Analysis on Human Cerebrovascular Phantom,” in *Progress in Advanced Computing and Intelligent Engineering*, Springer, 2018, pp. 219–229.

[194] “MeshLab.” .

[195] “Rhino - Downloads.” .

[196] K. L. Mettinger and K. Ericson, “Fibromuscular dysplasia and the brain. I. Observations on angiographic, clinical and genetic characteristics.,” *Stroke*, vol. 13, no. 1, pp. 46–52, 1982.

[197] M. F. Fillinger, S. P. Marra, M. L. Raghavan, and F. E. Kennedy, “Prediction of rupture risk in abdominal aortic aneurysm during observation: Wall stress versus diameter,” *J. Vasc. Surg.*, vol. 37, no. 4, pp. 724–732, 2003.

[198] **P. Rakshit**, N. Das, M. Nasipuri, and S. Basu, “Hemodynamic Analysis on Human Cerebrovascular Phantoms with and Without Aneurysm,” in *Proceedings of the International Conference on Computing and Communication Systems*, 2018, pp. 383–392.

[199] Y. Wang, C. C. Barbacioru, D. Shiffman, S. Balasubramanian, O. Iakoubova, M. Tranquilli, G. Albornoz, J. Blake, N. N. Mehmet, and D. Ngadimo, “Gene expression signature in peripheral blood detects thoracic aortic aneurysm,” *PLoS One*, vol. 2, no. 10, p. e1050, 2007.

[200] J. Shum, G. Martufi, E. Di Martino, C. B. Washington, J. Grisafi, S. C. Muluk, and E. A. Finol, “Quantitative assessment of abdominal aortic aneurysm geometry,” *Ann. Biomed. Eng.*, vol. 39, no. 1, pp. 277–286, 2011.

[201] J. R. Cebral, M. A. Castro, J. E. Burgess, R. S. Pergolizzi, M. J. Sheridan, and C. M. Putman, “Characterization of cerebral aneurysms for assessing risk of rupture by using patient-specific computational hemodynamics models,” *Am. J. Neuroradiol.*, vol. 26, no. 10, pp. 2550–2559, 2005.

[202] **P. Rakshit**, N.Das, M Nasipuri, S. Basu, “Classification of normal and anomalous regions in 3D human cerebrovascular phantom,” *Int. J. Sci. Eng. Res. Vol. 8, Issue 3, March-2017*, vol. 8, no. 3, pp. 1863–1867, 2017.

[203] **P Rakshit**, M Nasipuri, N. Das. & S. Basu., “Classification of anomalous region in human cerebrovascular structure using Random Forest,” *IJLTET*, vol. 9, no. 3, pp. 015–021, 2018.

[204] J. A. Hertz, *Introduction to the theory of neural computation*. CRC Press, 2018.

[205] D. M. Wolpert, R. C. Miall, and M. Kawato, “Internal models in the cerebellum,” *Trends Cogn. Sci.*, vol. 2, no. 9, pp. 338–347, 1998.

[206] I. A. Basheer and M. Hajmeer, “Artificial neural networks: fundamentals, computing, design, and application,” *J. Microbiol. Methods*, vol. 43, no. 1, pp. 3–31, 2000.

[207] J. Cheng and R. Greiner, “Comparing Bayesian network classifiers,” in *Proceedings of the Fifteenth conference on Uncertainty in artificial intelligence*, 1999, pp. 101–108.

[208] G. Ou and Y. L. Murphey, “Multi-class pattern classification using neural networks,” *Pattern Recognit.*, vol. 40, no. 1, pp. 4–18, 2007.

[209] A. Bosch, A. Zisserman, and X. Munoz, “Image classification using random forests and ferns,” in *Computer Vision, 2007. ICCV 2007. IEEE 11th International Conference on*, 2007, pp. 1–8.

[210] S. B. Kotsiantis, I. Zaharakis, and P. Pintelas, “Supervised machine learning: A review of classification techniques,” *Emerg. Artif. Intell. Appl. Comput. Eng.*, vol. 160, pp. 3–24, 2007.

[211] J. Shotton, M. Johnson, and R. Cipolla, “Semantic texton forests for image categorization and segmentation,” in *Computer vision and pattern recognition, 2008. CVPR 2008. IEEE Conference on*, 2008, pp. 1–8.

[212] T. Y. Kong, A. W. Roscoe, and A. Rosenfeld, “Concepts of digital topology,” *Topol. Appl.*, vol. 46, no. 3, pp. 219–262, 1992.